Enhanced ongoing endogenous activity predicts elimination of adult-born neurons in the mouse olfactory bulb

Thesis submitted as requirement to fulfill the degree ,,Doctor of Philosophy" (Ph.D)

at the
Faculty of Medicine
Eberhard Karls Universität
Tübingen

by

Su, Xin

2020

Dean: Professor Dr. B. Pichler

First reviewer: Professorin Dr. O. Garaschuk
Second reviewer: Professorin Dr. M. Knipper-Breer

Date of oral examination: 01.10.2020

Table of contents

List of abbreviations

2P	two-photon
4DSPA	4D structural plasticity analyses
ABC	adult-born cell
AMPAR	α-amino-3-hydroxy-5-methyl-4-isoxazolepropionic acid receptor
ANOVA	analysis of variance
AOB	accessory olfactory bulb
AP	action potential
AUC	area under the curve
BNST	bed nucleus of the stria terminalis
BPM	breaths per minute
BrdU	bromodeoxyuridine
BW	body weight
CB	calbindin
CR	calretinin
CREB	cAMP response element-binding protein
CSF	cerebrospinal fluid
CX43	connexin 43
DBD	day before death
DCX	doublecortin
DG	dentate gyrus
DPI	days post-viral injection
EPL	external plexiform layer
ETC	excitatory external tufted cell
FOV	field of view
FRET	Förster resonance energy transfer
GABA	γ-aminobutyric acid
GC	granule cell
GCL	granule cell layer
GFAP	glial fibrillary acidic protein
GLAST	astrocyte-specific glutamate transporter
GPCR	G protein-coupled receptor
HP	hippocampus
IQR	interquartile range
i.p.	intraperitoneal
JGN	juxtaglomerular neuron
M/T	mitral and tufted
MCL	mitral cell layer
MOB	main olfactory bulb
MOE	main olfactory epithelium
NC	neurocalcin

NMDAR	N-methyl-D-aspartate receptor
NSC	neuronal stem cell
OSNs	olfactory sensory neurons
PGC	periglomerular cell
PSD 95	Postsynaptic density protein 95
PV	parvalbumin
RGB	red-green-blue
RMS	rostral migratory stream
ROI	region of interest
s.c.	subcutaneous
SAC	short axon cell
SGZ	subgranular zone
SVZ	subventricular zone
TDBL	total dendritic branch length
TTX	tetrodotoxin
VNO	vomeronasal organ
VSN	vomeronasal sensory neuron
ΔR/R	Relative change in Twitch-2B ratio over time

1. Introduction

1.1 Olfaction

Olfaction is the process whereby odorant molecules are receipted and interpreted by the nervous system (Mori, 2001). Olfaction is one of the major chemosensory modalities and essential for any animals to survive (e.g. locating food, water, predator deterrence and avoidance) and reproduce (e.g. sexual and maternal behaviors) in the natural environment (Leinwand and Chalasani, 2011; Lledo et al., 2005). In the rodent brain, there are two different olfactory systems: the main olfactory system and the accessory olfactory system (Kadohisa, 2013).

In the main olfactory system, odorant molecules pass through the nasal cavity by air transport to the main olfactory epithelium (MOE) (Soudry et al., 2011). Odorant molecules interact with the olfactory receptors on the dendrites of olfactory sensory neurons (OSNs), which locate in the MOE (Mombaerts et al., 1996). There are in total ~1000 different types of olfactory receptors, encoded by ~1000 different genes (~3% of all the genes in the genome) in mammals (Buck and Axel, 1991; Mombaerts et al., 1996). Olfactory receptors are seven-helix transmembrane G protein-coupled receptors (GPCRs). Interaction between odorant molecules and olfactory receptors leads to an opening of ion channels via a second messenger pathway and drives action potential firing in the OSNs (Jones and Reed, 1989; Nakamura and Gold, 1987). Each OSN expresses one type of olfactory receptor, and OSNs expressing the same type of olfactory receptors converge their axons into the same glomerulus, a spherical structure in the main olfactory bulb (MOB) (Wachowiak and Shipley, 2006). In mice, one glomerulus receives axonal projections from ~1000 OSNs (Imai, 2014). In the glomeruli, the axon terminals of OSNs form synaptic connections with the primary dendrites of projection neurons - mitral and tufted cells (M/T cells) (Gire et al., 2013). After being processed in the MOB, olfactory information is transmitted by M/T cells to numerous downstream structures, including the piriform cortex, amygdala, entorhinal cortex, anterior olfactory nucleus, olfactory tubercle and so on (Igarashi et al., 2012; Nagayama et al., 2010).

In the accessory olfactory system, odorant molecules bind to the olfactory receptors on the dendrites of vomeronasal sensory neurons (VSNs), which reside in the vomeronasal organ (VNO) and send axonal projections to the accessory olfactory bulb (AOB). VSNs expressing the same type of olfactory receptors project their axons into multiple glomeruli and form synaptic connections with projection mitral cells, which send olfactory information to the medial amygdala and the bed nucleus of the stria terminalis (Holy, 2018). The accessory olfactory system mainly contributes to the sensing of non-volatile pheromones, while the main olfactory system contributes to the detection of volatile odorant molecules (Dulac and Torello, 2003; Kadohisa, 2013). The accessory olfactory system is a structure that cannot be found in the adult human brain, in contrast to many other mammals (Zilles, 2004).

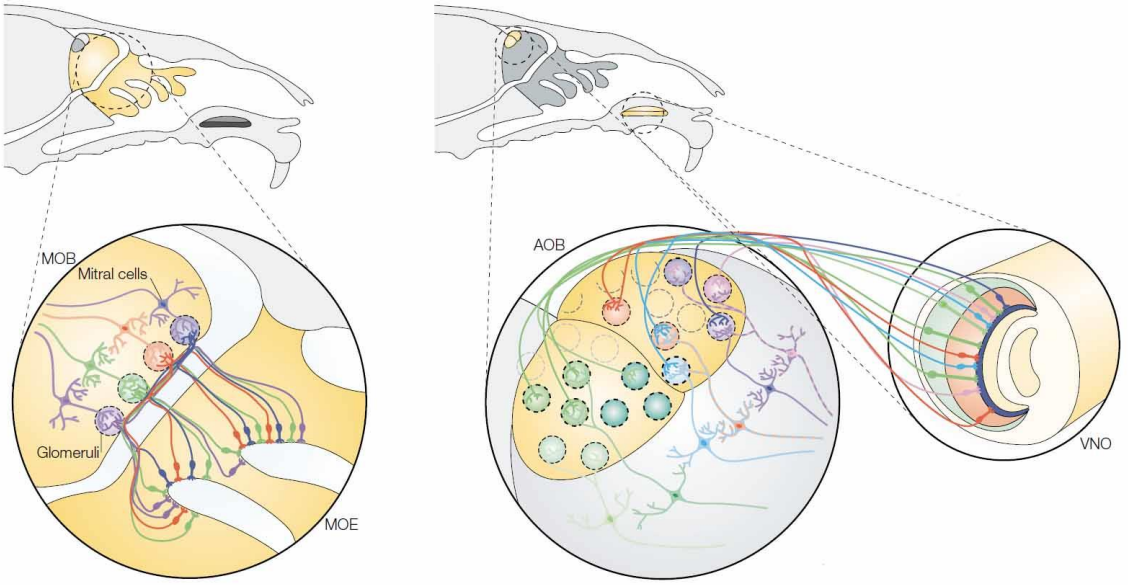

Figure 1. Schematic representation of the main and accessory olfactory system in the rodent brain. Odorant molecules inhaled into the nasal cavity bind to the olfactory receptors on the dendrites of olfactory sensory neurons (OSNs) in the main olfactory epithelium (MOE) and the vomeronasal organ (VNO). In the MOE (left), OSNs expressing the same type of olfactory receptors (indicated by different colors) converge their axons into the same glomerulus (bottom), where they form synaptic connections with mitral and tufted cells (M/T cells), the two major types of output neurons in the main olfactory bulb (MOB). In the VNO (right), vomeronasal sensory neurons (VSNs) expressing the same type of olfactory receptors project their axons into multiple glomeruli in the accessory olfactory bulb (AOB). The mitral output neurons project their axons to the medial amygdala and the bed nucleus of the stria terminalis, modified from (Dulac and Torello, 2003).

1.2 Neuronal circuitry in the main olfactory bulb

As described in 1.1, the MOB is the first central relay of the olfactory system. The ability to process olfactory information depends on the structural architecture of neuronal circuitry in the MOB. Histologically, the MOB has been divided into multiple layers, and neurons in the MOB have been categorized according to the locations of their cell bodies (Nagayama et al., 2014). In the early 1970s, data obtained with Golgi staining experiments showed that neurons in distinct layers of the MOB are morphologically different from each other (Pinching and Powell, 1971; Price and Powell, 1970). Juxtaglomerular neurons (JGNs), granule cells, mitral cells and tufted cells were categorized in the MOB (Figure 2). JGNs refer to three types of morphologically distinct cells in the glomerular layer: inhibitory periglomerular cells (PGCs) and short axon cells (SACs), and excitatory external tufted cells (ETCs) (Homma et al., 2013; Parrish-Aungst et al., 2007). In the MOB, the ratio of inhibitory neurons to excitatory neurons is approximately 100:1, much higher than that in other brain areas, suggesting that inhibition plays a critical role in the processing of olfactory information (Lledo et al., 2008).

1.2.1 Periglomerular cells

PGCs have the smallest cell body (5-10 μm in diameter) among JNGs, release neurotransmitter γ-aminobutyric acid (GABA), and in most cases, project dendrites into a single glomerulus (Parrish-Aungst et al., 2007). Some PGCs have short, local projection axons, while the others are reported to be axon-less (Kosaka and Kosaka, 2011). The dendrites of PGCs and the secondary dendrites of M/T cells form reciprocal dendrodendritic synapses, with closely opposing pre- and post-synaptic regions (Imai, 2014). In this synapse, glutamate released from M/T cell spines activates the α-amino-3-hydroxy-5-methyl-4-isoxazolepropionic acid receptors (AMPARs) and N-methyl-D-aspartate receptors (NMDARs) on PGC spines to increase local Ca^{2+} concentration in PGC spines. The elevated Ca^{2+} concentration triggers the release of GABA from PGC spines, which acts on $GABA_A$ receptors of M/T cells to postsynaptically inhibit M/T cells (Halabisky et al., 2000; Lepousez et al.,

2013). GABA release is locally controlled by dendritic calcium spikes, independent of M/T cells' axonal action potentials (Isaacson and Strowbridge, 1998). PGCs express a variety of neurochemical markers, including calbindin (CB), calretinin (CR), neurocalcin (NC) and parvalbumin (PV), although the functional differences between subpopulations expressing different markers remain largely unknown (Parrish-Aungst et al., 2007). PGCs can be activated by OSNs, mitral cells, tufted cells, and can exert intraglomerular feedback inhibition onto these cell types as well as on neighboring JGNs (Murphy et al., 2005).

1.2.2 Short axon cells

SACs comprise a heterogeneous population of neurons in the MOB. Based on the locations of their cell bodies, SACs are classified as superficial SACs and deep SACs (dSACs). Cell bodies of superficial SACs are located in the glomerular layer, while cell bodies of dSACs are located in the internal region of the external plexiform layer (EPL), mitral cell layer (MCL) and granule cell layer (GCL) (Nagayama et al., 2014). In this thesis, SACs specifically refer to superficial SACs. SACs release both dopamine and GABA as neurotransmitters, and the release of these two neurotransmitters is independent and serves temporally different roles. GABA release triggers a fast-rising postsynaptic current, which lasts for only 50-100 milliseconds, while evoked dopamine release lasts for tens of seconds (Borisovska et al., 2013). In total, PGCs and SACs account for ~50% of JGNs (Parrish-Aungst et al., 2007). SACs target M/T cells and the other JGNs, and they also mediate presynaptic inhibition of OSNs through the $GABA_B$ receptors and D2 dopaminergic receptors on the axonal terminals of OSNs (Bywalez et al., 2017; Imai, 2014; McGann et al., 2005). The processes of SACs contact multiple glomeruli (up to ~20-30 glomeruli) to form distinct intraglomerular and interglomerular connections, which can dynamically regulate information transferring from OSNs to M/T cells (Aungst et al., 2003; Kiyokage et al., 2010).

1.2.3 External tufted cells

The other half of JGNs are external tufted cells (ETCs) (Pinching and Powell, 1971). Glutamatergic ETCs are located within the glomerular layer or at the border between the glomerular layer and the EPL (Hayar et al., 2004a). ETCs have the largest cell body (10-15 μm in diameter) among JGNs (Pinching and Powell, 1971). In most cases, ETCs have a single apical dendrite projecting into one glomerulus, and dendrites ramifying throughout a large volume (~80%) of the glomerulus (Hayar et al., 2004a; Nagayama et al., 2014). In sharp contrast to PGCs and SACs, which often receive polysynaptic inputs from OSNs, ETCs receive monosynaptic inputs from OSNs and act as a major excitatory link between OSNs and PGCs/SACs to synchronize activity in the glomerulus (Hayar et al., 2004b). ETCs have a lower activation threshold than M/T cells. Combined with the fact that stimulation-induced activity of ETCs and M/T cells are highly correlated, this suggests ETCs mediate feedforward excitation of M/T cells (Jan et al., 2009). The most prominent physiological characteristic of ETCs is their ability to generate spontaneous spike bursts, which are related to respiration (Hayar et al., 2004a). Interestingly, ETCs with dendrites in the same but not different glomeruli exhibit synchronous bursting activity, which involves both synaptic and gap junction interactions (Hayar et al., 2005).

1.2.4 Granule cells

GABAergic granule cells (GCs) are located in the GCL and account for more than 90% of interneurons in the MOB (Shepherd et al., 2007). GCs are axon-less and extend their apical dendrites into the EPL, where they make reciprocal dendrodendritic synapses with the secondary dendrites of M/T cells (Balu et al., 2007; Nagayama et al., 2014). GCs-mediated feedback inhibition of M/T cells in the EPL is critical for olfactory information processing in the MOB (Cleland and Linster, 2005). In the GCL, GCs receive the proximal excitatory axonal inputs from axon collaterals of mitral cells and centrifugal axons of cortical pyramidal cells (Balu et al., 2007). Distal dendrodendritic inputs in the EPL have slow kinetics, while proximal axonal inputs in the GCL show fast kinetics, suggesting that they are functionally distinct synapses (Balu et al., 2007). In addition to

distal and proximal excitatory inputs, GCs also receive GABAergic inhibitory inputs from dSACs (Lepousez et al., 2013). Based on their dendritic morphology and the locations of their cell bodies in the GCL, GCs can be subdivided into several subgroups, but the functional specificity for each subgroup remains largely unclear (Merkle et al., 2014; Takahashi et al., 2016, 2018).

1.2.5 Mitral cells and tufted cells

Mitral cells and tufted cells (M/T cells) are the two major types of projection neurons in the MOB. M/T cell extends a single primary dendrite into one glomerulus to receive inputs from OSNs. ~20 M/T cells associated with the same glomerulus are located below this glomerulus (Murthy, 2011). Cell bodies of mitral cells are surrounded by the neighboring mitral cells in the MCL, and the secondary dendrites of mitral cells radiate horizontally in the deeper EPL, while tufted cells have their cell bodies in the EPL and extend their secondary dendrites in the superficial EPL (Imamura and Greer, 2009; Nagayama et al., 2014). Two distinct connections, between the primary dendrites of M/T cells and JGNs in the glomerular layer and between the secondary dendrites of M/T cells and GCs in the EPL, tightly control the action potential firing of M/T cells (Lledo et al., 2005). The targets of axonal projections are different between mitral cells and tufted cells. Mitral cells project axons to both the anterior and posterior parts of the olfactory cortex, whereas tufted cells only project axons to the anterior part of the olfactory cortex, including the anterior olfactory nucleus, anterior piriform cortex, and olfactory tubercle. Even in the anterior olfactory cortex, M/T cells project their axons to distinct, largely non-overlapping subregions (Igarashi et al., 2012; Nagayama et al., 2014).

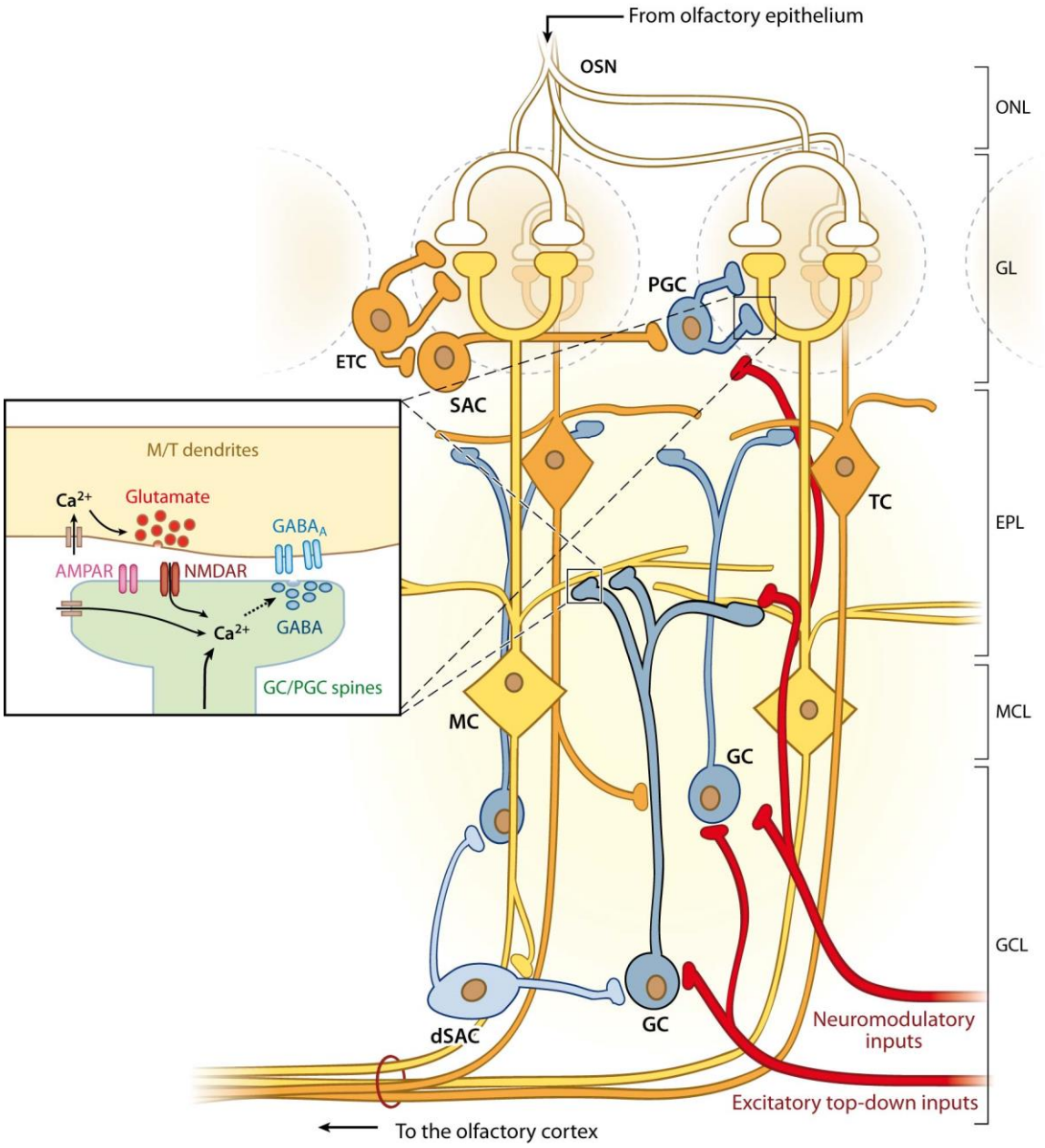

Figure 2. Schematic drawing of neuronal circuitry in the rodent main olfactory bulb. In the MOB, olfactory sensory neurons (OSNs) converge their axons into the glomeruli in the glomerular layer. Inside the glomeruli, the axon terminals of OSNs make synapses with the primary dendrites of output neurons - mitral and tufted cells (M/T cells). In the glomerular layer, juxtaglomerular neurons (JGNs), including periglomerular cells (PGCs), short-axon cells (SACs) and external tufted cells (ETCs), provide sophisticated regulation of glomerular synaptic transmission. In the external plexiform layer (EPL), the secondary dendrites of M/T cells make reciprocal dendrodendritic synapses with apical dendrites of granule cells (GCs), which are inhibited by deep short-axon cells (dSACs) in the deeper bulbar region. The axons of M/T cells project to different higher brain regions in a non-overlapping manner. PGCs and GCs also are innervated by neuromodulatory top-down inputs from the olfactory cortex and other central brain regions. ONL, olfactory nerve layer; GL, glomerular layer; MCL, mitral cell layer; MC, mitral cells; TC, tufted cells; GCL, granule cell layer; modified from (Lepousez et al., 2013).

1.3 Adult neurogenesis in the main olfactory bulb

The classic enigma proposed by Ramon *y* Cajal was that neurogenesis, a process where functional newborn neurons are produced by stem cells, only happens at embryonic and early postnatal stages, and no neurons can be generated and added into the adult brain (Ming and Song, 2005). In the 1960s, the pioneer studies took advantage of [H^3]-thymidine labeling and autoradiography to prove that newborn neurons can be added into different areas of adult rat brain (Altman, 1963, 1969; Altman and Das, 1965). However, these findings were largely ignored because of the lack of functional relevance. In the 1980s, this field was revisited with the introduction of a synthetic thymidine analogue - bromodeoxyuridine (BrdU), which can be applied to detect proliferating cells in living tissues (Gratzner, 1982). BrdU incorporating cells were detected in the brain samples of all mammals examined, including the adult human brain samples (Eriksson et al., 1998; Ming and Song, 2005). Combining retroviral-based lineage tracing with electrophysiological patch-clamp recordings, researchers obtained the most convincing data so far showing that newly-generated cells in the adult mammalian brain are indeed functional neurons (Boldrini et al., 2018; Carleton et al., 2003; Moreno-Jiménez et al., 2019; van Praag et al., 2002).

Nowadays, it is generally accepted that significant level of adult neurogenesis happens in at least two brain regions in mammals under physiological conditions: the subventricular zone (SVZ) of lateral ventricle and the subgranular zone (SGZ) of the dentate gyrus in the hippocampus (Ming and Song, 2011; Zhao et al., 2008). In the SVZ, newborn cells generated by adult neuronal stem cells (NSCs) migrate through the rostral migratory stream (RMS) into the OB to differentiate into local interneurons: PGCs, SACs and GCs, while newborn cells generated by adult NSCs in the SGZ undergo a short distance migration into the granule cell layer to differentiate into the principal neurons - granule cells in the hippocampal dentate gyrus (Figure 3) (Gould and Gross, 2002; Ming and Song, 2005).

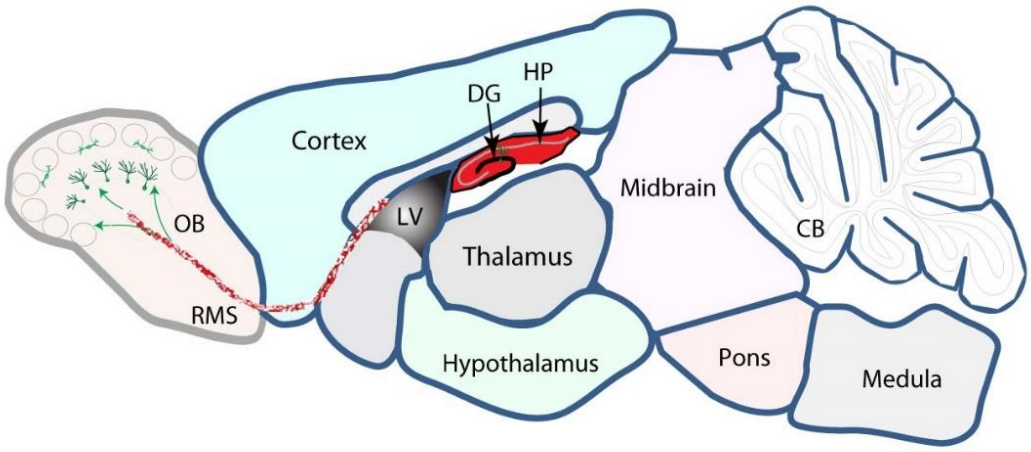

Figure 3. Adult neurogenesis in the subventricular zone and the hippocampal dentate gyrus. A sagittal overview of the adult rodent brain highlighting the two neurogenic niches. Neural stem cells (NSCs) in the subventricular zone (SVZ) give rise to newborn cells, which migrate through the rostral migratory streams (RMS) – a remarkably long journey, to the olfactory bulb (OB) to differentiate into local interneurons: granule cells, periglomerular cells and short axon cells. Neural stem cells in the subgranular zone (SGZ) of the dentate gyrus (DG) in the hippocampus (HP) give rise to newborn cells, which migrate radially through a short distance to granule cell layer to become granule cells - the principal cells in the hippocampus. CB, cerebellum, modified from (Ming and Song, 2011).

1.3.1 Adult neural stem cells in the SVZ

Adult NSCs (also known as type B cells or radial-glia like cells) in the SVZ are derived from a subpopulation of embryonic stem cells, which slowly divide at perinatal stages and remain in an undifferentiated state to become adult NSCs (Furutachi et al., 2015). Type B cells express a variety of intermediate filament proteins, including nestin, sox2 and vimentin (Figure 4) (Ming and Song, 2011). Type B cells maintain a quiescent state, and their cell bodies are located immediately under the ependymal cell layer, with a long basal process terminating on the blood vessels and a single short apical process poking through the ependymal cell layer to contact the ventricle, which is filled with cerebrospinal fluid (CSF) (Figure 4) (Mirzadeh et al., 2008). The number of NSCs in the SVZ shows an age-dependent decrease. However, once activated, NSCs exhibit similar proliferation and differentiation capacity in the young and old brain. It is a compensatory mechanism for type B cells to actively maintain quiescence to avoid full depletion of the NSC pool (Kalamakis et al., 2019). NSCs in the SVZ are dynamically regulated by astrocytes, microglia, ependymal

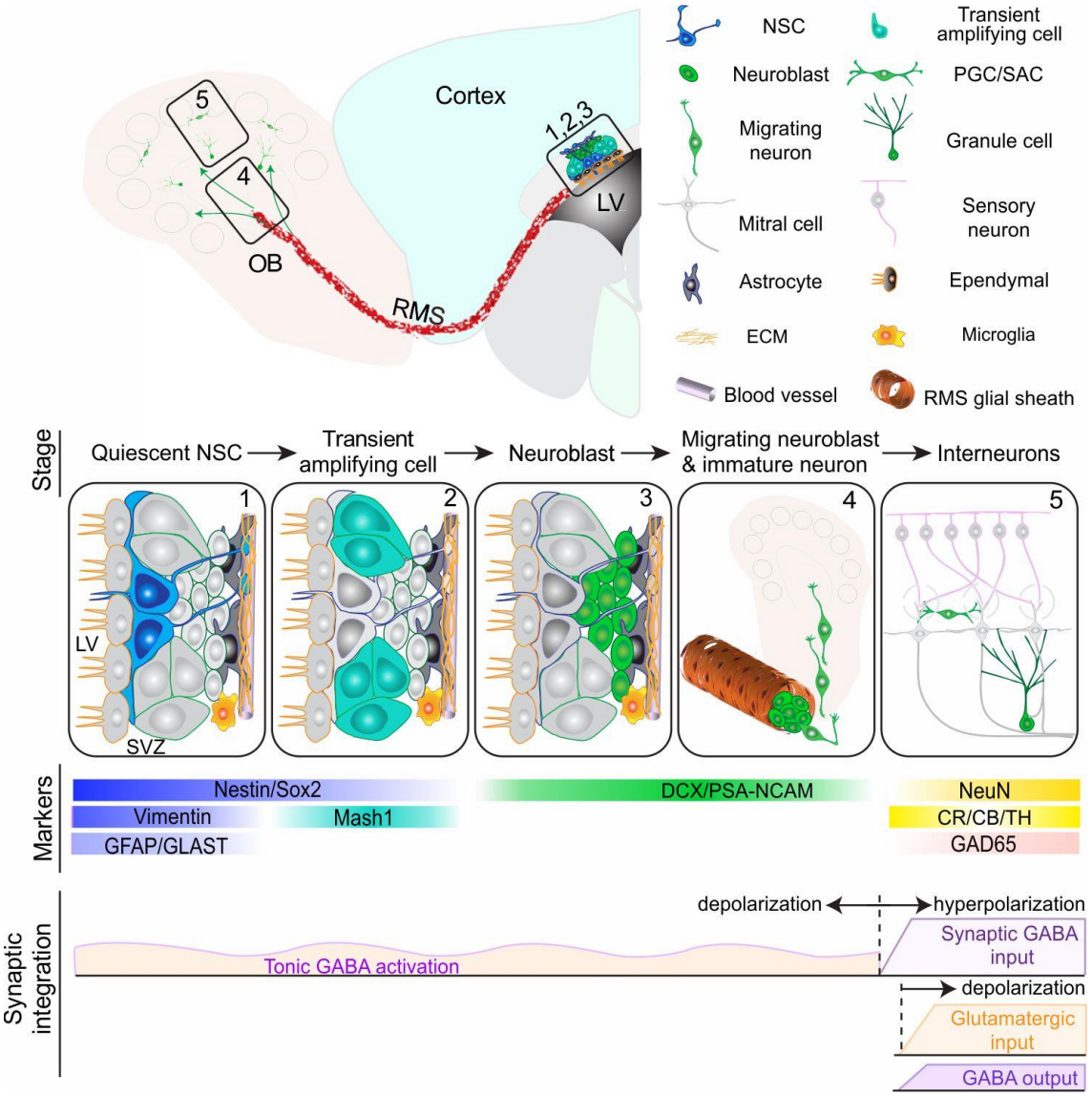

Figure 4. Different stages of adult neurogenesis in the subventricular zone. (1) Activation of quiescent radial-glia like neural stem cells (NSCs, also known as type B cells) in the subventricular zone (SVZ) niche. Type B cell has a long basal process terminating on the blood vessels and a single short apical process poking through the ependymal cell layer to contact the ventricle. (2) The proliferation of rapidly cycling type C cells (also known as transient-amplifying cells). This process can expand the progeny population generated by a single NSC division. (3) Generation of neuroblasts, which have a prominent, long leading process and a short trailing process. (4) Tangential migration in the rostral migratory stream (RMS), radial and the subsequent lateral migration in the core of the olfactory bulb (OB). (5) Differentiation and maturation of newborn cells to become granule cells (GCs) and juxtaglomerular neurons (JGNs), including periglomerular cells (PGCs) and short axon cells (SACs), in the OB. ECM, extracellular matrix, modified from (Bond et al., 2015; Ming and Song, 2011).

cells, blood vessels, the extracellular matrix (ECM) in the local neurogenic niche, and also long-range projections (Bond et al., 2015). Depending on their positions in the SVZ, adult type B cells generate different neuronal subtypes in

the OB, similar to embryonic stem cells, which means the positional information of embryonic stem cells is maintained in adult NSCs (Fuentealba et al., 2015). In addition to their NSC properties, type B cells also exhibit classic ultrastructural properties and neurochemical markers of astroglia. For example, glial fibrillary acidic protein (GFAP) and astrocyte-specific glutamate transporter (GLAST) (Doetsch et al., 1999; Kriegstein and Alvarez-Buylla, 2009). It has been reported that in the adult SVZ, type B cells communicate with niche astrocytes through intercellular Ca^{2+} propagating waves, which are regulated by connexin 43 (CX43)-mediated gap junctions (Lacar et al., 2011).

1.3.3 Migration of neuroblasts

Transient-amplifying type C cells divide to generate neuroblasts (type A cells), which are characterized by the expression of doublecortin (DCX) and polysialylated-neural cell adhesion molecule (PSA-NCAM) (Doetsch et al., 1999; Garcia et al., 2004; Shen et al., 2008; Wang et al., 2011). In the SVZ, type A neuroblasts migrate through a tubular network formed by type B and type C cells into the RMS, which extends into the core of the OB (Doetsch et al., 1997). In the adult rodent brain, more than 30,000 type A neuroblasts migrate from the SVZ to the OB every day in the adult rodent brain (Lois and Alvarez-Buylla, 1994). In the RMS, type A neuroblasts form densely packed, elongated clusters called chains, which are enwrapped by astrocytic tunnels (also named as glial tubes) (Lois et al., 1996). Chain-forming neuroblasts directly contact vascular endothelial cells, with the intervening astrocytic endfeet enwrapping the blood vessels (Whitman et al., 2009). Neuroblasts migrate along with each other by forming discontinuous adherent junctions. This suggests that neuroblasts themselves are the migratory scaffold (Kaneko et al., 2017). Migrating type A neuroblasts have a highly polarized morphology, with a prominent, long leading process and a short trailing process (Kaneko et al., 2017). The movement of neuroblasts includes four steps: (1) growth of the leading process, (2) formation of a transient ‘swelling’ in the leading process and movement of the centrosome, (3) translocation of the soma together with the nucleus, (4) a pause which defines saltatory movement (Figure 5) (Ota et al., 2014; Schaar and McConnell,

2005). The long-distance, directional migration of neuroblasts is regulated by various endogenous and exogenous factors. However, it seems like the directional migration in the RMS is not influenced by chemoattractants from the OB because surgical removal of the OB does not affect the directional migration (Jankovski et al., 1998; Kirschenbaum et al., 1999). Inside the RMS, some neuroblasts are also proliferative, but this stream of proliferating neuroblasts does not extend into the OB (Bordiuk et al., 2014). After focal demyelination in the corpus callosum, neuroblasts in the adult SVZ change their migratory pathway to become oligodendrocytes in the corpus callosum, indicating the *in vivo* lineage plasticity of neuroblasts (Jablonska et al., 2010).

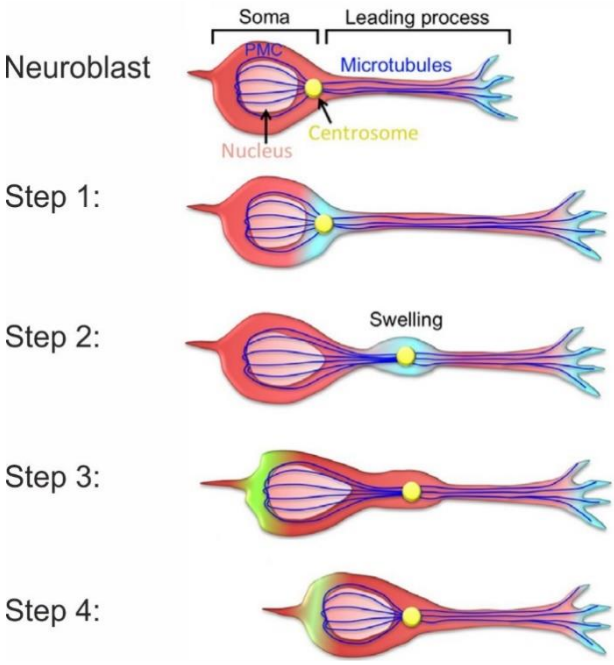

Figure 5. The saltatory migration of neuroblasts. Neuroblasts have a typical bipolar morphology, with a prominent, long leading process and a short trailing process. A movement of neuroblasts includes the following four steps: (1) extension of the leading process, (2) formation of a transient 'swelling' in the leading process and movement of the centrosome, (3) soma translocation, (4) a pause following soma translocation. Migration happens when repeating this cycle many times, modified from (Kaneko et al., 2017).

It takes approximately 4-6 days for newborn cells to migrate from the SVZ to the core of the mouse OB (Belluzzi et al., 2003; Petreanu and Alvarez-Buylla, 2002). Upon arrival in the core of OB, neuroblasts detach from the RMS to start a saltatory, radial migration, which is unchained but also relies on blood vessels (Bovetti et al., 2007). For adult-born JGNs, when arriving in the glomerular layer, they switch from radial migration to lateral migration, which is cell age-dependent, exhibits a 'stop-and-go' temporal characteristic, and can be either unidirectional or multidirectional. Surprisingly, single adult-born JGN can travel

up to 900 μm (cumulative distance) before it finally settles down (Liang et al., 2016). Although the exact mechanisms driving the lateral migration have not been elucidated, one hypothesis is that adult-born JGNs migrate laterally to find their parent glomerulus (Kovalchuk et al., 2015). By closing naris with a unilateral plug to deprive olfactory inputs, it has been demonstrated that tangential migration in the RMS, radial migration in the core of the OB and lateral migration in the glomerular layer are not sensitive to olfactory inputs (Frazier-Cierpial and Brunjes, 1989; Liang et al., 2016).

1.3.4 Differentiation and maturation of adult-born neurons

In the OB, about 90-95% of adult-born cells (ABCs) migrate into the granule cell layer to differentiate into GCs, while the other 5-10% migrate into the superficial glomerular layer to become JGNs, including PGCs and SACs (Bovetti et al., 2007; Lledo et al., 2006). Most ABCs differentiate into GABAergic neurons (GCs, PGCs and SACs), but a tiny fraction of ABCs become glutamatergic SACs (Brill et al., 2009). Almost all GC subtypes derived from embryonic/neonatal neurogenesis can also be generated by adult neurogenesis, although embryonic/neonatal neurogenesis and adult neurogenesis have different tendencies in generating different GC subtypes, for example, adult neurogenesis tends to generate GCs in the deep GCL (Fuentealba et al., 2015; Merkle et al., 2014; Takahashi et al., 2018). Adult-born JGNs express a variety of immunohistochemical markers, including CB, CR, PV and tyrosine hydroxylase (TH), indicating that all PGC subtypes, as well as SACs, can be generated by adult neurogenesis (Whitman and Greer, 2007a).

Morphologically, ~2 weeks after birth, adult-born GCs develop elaborate dendrites extending into the EPL (Petreanu and Alvarez-Buylla, 2002). Longitudinal *in vivo* single-cell imaging experiments showed that ~30 days after birth, adult-born GCs gain the stable dendritic morphology (Sailor et al., 2016). For adult-born JGNs, it is reported that from 10 to 45 days after their birth, the complexity of their dendritic morphology is increasing to reach the morphological steady-state, which cannot be maintained after 6 months of cell age (Livneh and Mizrahi, 2011; Mizrahi, 2007). The dendritic spines of both

adult-born GCs and JGNs are structurally highly plastic throughout life, likely allowing the olfactory circuitries to reliably adapt to new odor environments (Mizrahi, 2007; Sailor et al., 2016). Interestingly, it has been reported that odor deprivation by unilateral naris closure has a negligible impact on the dendritic morphogenesis of both adult-born JGNs and GCs in the OB (Mizrahi, 2007; Petreanu and Alvarez-Buylla, 2002). A more precise experiment combining intrinsic optical imaging with *in vivo* two-photon imaging techniques demonstrated that passive odor exposure promotes the dendritic morphogenesis and synaptogenesis of immature adult-born PGNs only in odor-activated glomeruli, but cannot alter the dendritic morphogenesis and synaptogenesis of immature adult-born PGNs in other inactive glomeruli (Livneh et al., 2009).

Functionally, the synaptic and functional integration of ABCs in the OB was first characterized by a combination of BrdU incorporation, pseudorabies virus-based transsynaptic labeling and c-Fos mapping of odor-evoked neuronal activity (Carlén et al., 2002), and then was studied with electrophysiological recording technique (Belluzzi et al., 2003; Carleton et al., 2003). Neuroblasts in the RMS express extrasynaptic $GABA_A$ receptors, followed by AMPARs. Once detached from the RMS to start a radial migration in the core of the OB, newborn cells start to express functional NMDARs to sense local neuronal activity (Carleton et al., 2003). This is remarkably different from the neuronal functional maturation process in the developing brain, where neurons firstly express NMDA receptors, which are required for activity-dependent trafficking of AMPARs (Carleton et al., 2003; Durand et al., 1996; Sultan et al., 2015). As in the developing brain, activation of $GABA_A$ receptors leads to depolarization of migrating neuroblasts in the adult brain, probably due to the high concentration of Cl^- inside the neuroblasts (Carleton et al., 2003). In the OB, ABCs receive both GABAergic and glutamatergic synaptic inputs before they can generate action potentials. This suggests ABCs follow the rule of “listening before speaking,” which means they sample the neural network activity before sending out any output signals (Belluzzi et al., 2003; Carleton et al., 2003; Kelsch et al., 2008). Interestingly, adult-born GCs are first innervated by centrifugal axons or

M/T cell axon collaterals in the GCL and then form reciprocal dendrodendritic synapses with apical dendrites of M/T cell in the EPL (Whitman and Greer, 2007b). The glutamatergic synapses increase their AMPARs/NMDARs ratio when transiting from immature, plastic to more mature, stable states (Grubb et al., 2008). One notable difference between adult-born PGCs and GCs is that in adult-born PGCs, maturation of the voltage-dependent sodium current precedes the formation of synaptic contacts, while in adult-born GCs, the fully developed sodium current can only be observed after the establishment of synaptic connections (Belluzzi et al., 2003; Lledo et al., 2006). It usually takes ~8-9 weeks for ABCs to reach maturity, when their action potential (AP) firing rates are similar to the neighboring resident cells' AP firing rates (Kovalchuk et al., 2015; Livneh et al., 2014).

1.3.5 Activity-dependent survival of adult-born neurons

Although thousands of ABCs migrate into the OB every day, only about half of them survive over prolonged periods of time, and the other half is eliminated by the programmed cell death (also referred to apoptosis). According to the data obtained with BrdU incorporation and labeling experiments, this largely happens between 15 and 45 days after birth (Mouret et al., 2008; Petreanu and Alvarez-Buylla, 2002; Whitman and Greer, 2007a; Winner et al., 2002). Apoptosis is an active intrinsic cell death process, which mainly affects isolated cells. Cysteine-dependent aspartate proteases (caspases)-dependent apoptosis has been suggested as a major contributor to the death of ABCs because treatment with caspases inhibitors increases the survival rate of ABCs (Biebl et al., 2005; Kuhn, 2015). Apoptosis can be triggered by various stimuli and conditions, which activate caspases followed by neuronal morphological changes, including nuclear and cytoplasmic condensation, DNA cleavage in the nucleosome, nuclear membrane breakdown, plasma membrane blebbing, nuclear fragmentation and formation of apoptotic bodies (Benn and Woolf, 2004; Elmore, 2007). Plenty of factors, including intracellular signaling molecules and pathways (pro- and anti-apoptotic Bcl-2 family, cAMP response element-binding protein signaling pathway), extracellular signaling molecules (e.g. neurotrophic

and growth factors, hormones) and neurotransmitters (GABA, glutamate, serotonin, acetylcholine) were shown to influence the survival of ABCs (Kuhn, 2015). The cellular components of the brain's immune system, including microglia and astrocytes, have also been shown to directly control the survival of immature ABCs (Denizet et al., 2017; Sierra et al., 2010; Sultan et al., 2015).

A major theme in both the bulbar and hippocampal adult neurogenesis is how sensory experience influences the proliferation of NSCs, migration, maturation, integration, and survival of newborn cells (Lepousez et al., 2013). It is now generally recognized that sensory inputs can greatly affect the survival/death of newborn cells in the adult brain (Bond et al., 2015; Lledo et al., 2006; Ming and Song, 2011). In the OB, this was firstly reported in an experiment in which odor deprivation with naris closure was found to decrease the survival rate of adult-born GCs through elevated apoptosis (Corotto et al., 1994). Subsequently, it was shown that enriched odor exposure promotes the survival of bulbar adult-born interneurons without affecting NSC proliferation (Rochefort and Lledo, 2005; Rochefort et al., 2002). Passive activation of sensory inputs does not influence the survival/death of adult-born GCs, while active olfactory discrimination learning significantly increases the survival of adult-born GCs in the OB (Alonso et al., 2006; Sultan et al., 2011). Alike GCs, the survival of adult-born JGNs is also activity-dependent: olfactory enrichment and discrimination learning were reported to promote the survival of immature adult-born JGNs, while sensory deprivation inhibits it (Sakamoto et al., 2014; Sawada et al., 2011). The survival of ABCs in the mouse OB is robustly influenced by olfactory sensory experience during a restricted time period, suggesting the existence of a critical period (2-4 weeks after birth) when ABCs are the most sensitive to the influence of sensory inputs (Alonso et al., 2006; Mouret et al., 2008; Yamaguchi and Mori, 2005). Since ABCs start to receive synaptic inputs and integrate into the local circuitries during this time period, it has long been postulated that ABCs die because they "fail to integrate" into the pre-existing neuronal circuitry (Lin et al., 2010; Turnley et al., 2014). However, this hypothesis has never been tested directly.

Except for the sensory-driven activity, there is the other form of activity in the brain – the endogenous neuronal activity which is driven by the spontaneous activity of the surrounding neuronal network as well as the cell-autonomous activity and independent of sensory inputs (McVea et al., 2016). At the perinatal stages, when sensory inputs are not present, endogenous neuronal activity controls the proper formation of the blueprint of developing neural network, e.g., the proliferation of stem cells, neuronal migration, neural differentiation, dendritic morphogenesis and synaptogenesis, neurotransmitter specification and functional integration of immature neurons (Khazipov and Luhmann, 2006; Luhmann et al., 2016). In the adult brain, both NSCs in the SVZ and neuroblasts in the RMS exhibit endogenous calcium spikes (García-González et al., 2017; Lacar et al., 2011). In the RMS, endogenous calcium spikes control the speed and direction of neuroblast migration via activation of Ca^{2+}-dependent potassium channels (García-González et al., 2017). After switching from tangential migration to radial migration, migrating neuroblasts exhibit endogenous intracellular calcium transients, which are mediated by L-type calcium channels. However, manipulation of spontaneous intracellular calcium activity in the migrating neuroblasts doesn't affect the rate of radial migration (Darcy and Isaacson, 2009). Our study revealed the ubiquitous presence of endogenous calcium activity in the immature adult-born JGNs *in vivo*, and the strength of spontaneous activity shows a bell-shaped dependence on cell's age, peaking around 3 weeks of cell age (Maslyukov et al., 2018). The endogenous activity has been shown to influence the fate of adult-born GCs, with genetically enhanced (by expression of the bacterial voltage-gated Na^+ channel NaChBac) endogenous activity increasing and with genetically suppressed (by expression of Kir2.1 potassium channel) endogenous activity decreasing their survival (Lin et al., 2010). Knocking out NMDARs revealed the critical roles of synaptic inputs in regulating the survival of ABCs (Kelsch et al., 2012; Mu et al., 2015; Tashiro et al., 2006). Interestingly, the survival of NMDARs-deficient ABCs was fully rescued by increasing cell-intrinsic activity via NaChBac expression. This suggests that activity-dependent survival of ABCs depends to a large extent on

the overall level of cell-intrinsic activity and sensory driven activity, but to a lesser extent on its pattern (Lin et al., 2010).

In summary, the survival of ABCs in the OB can be influenced by both sensory-driven as well as endogenous activity.

1.3.6 Functional significance of adult-born neurons in the OB

When the phenomenon of adult neurogenesis was initially found, it was postulated that the major role of newborn neurons is to replace old, dying neurons within the mature circuits (Carleton et al., 2003; Nottebohm, 2002). In the mouse OB, resident JGNs exhibit a turnover rate of ~3% per month, and although newborn neurons added and old ones lost, the total number of JGNs remained unchanged, suggesting there is a balance between the number of adult-born JGNs and the number of lost resident JGNs (Imayoshi et al., 2008; Mizrahi et al., 2006), although there is a very recent study showed the increase of cell number in the OB and an expansion of the bulbar volume due to ABCs (Platel et al., 2019). More direct evidence came from *Sawada et al.*, after eliminating resident, mature JGNs with two-photon laser ablation, adult-born JGNs were shown to be recruited into the same positions which were filled by the eliminated JGNs before, indicating that ABCs indeed replace the dead neurons (Sawada et al., 2011). Long-term genetic labeling experiments showed that the majority of granule cells are replaced by ABCs, and the ablation of adult neurogenesis leads to a substantial reduction in the number of GCs in the OB (Breton-Provencher et al., 2009; Imayoshi et al., 2008). As mentioned above, ABCs form dendrodendritic connections with M/T cells to control the activity of M/T cells, ablated neurogenesis impairs lateral inhibition of M/T cells and reduces the frequency of gamma oscillations (Breton-Provencher et al., 2009). Thus, in the OB, ABCs are essential for the proper function of the bulbar circuitry.

In addition, cumulative evidence suggests that ABCs exhibit unique physiological properties at specific developmental stages, which allow ABCs to act as major mediators for an additional level of functional plasticity in the adult brain (Ming and Song, 2005). Shortly after their arrival in the OB, immature

adult-born GCs easily undergo long-term potentiation and this property is lost when newborn GCs become mature (Nissant et al., 2009). Immature adult-born JGNs exhibit lower spontaneous firing rates when compared with mature adult-born JGNs or resident cells (Kovalchuk et al., 2015; Livneh et al., 2014). Developing adult-born JGNs and adult-born GCs (2-4 weeks of cell age) are more sensitive to odorant stimuli, have broader odor response but lower odor-selectivity than their mature counterparts (8-9 weeks of cell age) (Livneh et al., 2014; Wallace et al., 2017). Interestingly, soon after receiving synaptic inputs, immature adult-born GCs are more responsive to novel odors, while resident GCs are less responsive to novel odors, indicating immature ABCs play important roles in the detection of new signals, which allows olfactory system to adapt to the constantly changing environment (Magavi et al., 2005). Moreover, sensory stimulation modifies the spine density and the excitability of ABCs but doesn‘t affect the morphology and function of preexisting neurons in the OB (Saghatelyan et al., 2005). These data suggest that ABCs not only replace dead neurons but also provide a form of morphofunctional plasticity in the OB.

Is adult neurogenesis in the OB necessary for normal olfactory learning and other olfaction-related behaviors? The answer is yes. By inhibiting the migration of newborn cells in the RMS, it has been shown that dramatic reduction in the number of ABCs in the OB impaired mice’s ability to discriminate two odorants but did not change olfactory detection level or memory (Bath et al., 2008; Gheusi et al., 2000). By exposing animals to an odor-enriched environment, which can promote the survival of ABCs as described in 1.3.5, it has been reported that the promoted survival of ABCs in the OB can improve animals’ odor discrimination ability. This suggests odor discrimination ability depends on the reinforcement of functional inhibitory circuitries by ABCs (Mandairon et al., 2006; Moreno et al., 2009). However, the genetic ablation of ABCs in the OB did not change animals’ odor discrimination ability, innate olfactory response, or long-term retention of odor-associated memory (Imayoshi et al., 2008). The pharmacological ablation of ABCs in the OB also did not change animals’ odor discrimination ability and long-term olfactory memory (Breton-Provencher et al., 2009). The discrepancies between these findings may be caused by the

odorants used in these studies, because inducible suppression of adult neurogenesis affects animal's ability to discriminate highly similar odorants but not distinct odorants (Enwere et al., 2004; Li et al., 2018). Optogenetic targeting experiment showed that activation of ABCs, but not early postnatal born neurons in the OB, facilitates discrimination learning of highly similar odorants, indicating an immediate causal relationship between adult neurogenesis in the OB and olfactory discrimination learning behaviors (Alonso et al., 2012). Surprisingly, adult neurogenesis in the OB has been linked to sexual and maternal behaviors. Pregnancy specifically increases the number of both adult-born GCs and JGNs in the OB by increasing the cell proliferation in the SVZ, which is mediated by a peptide hormone prolactin (Shingo et al., 2003). After the delivery, dendritic spines of adult-born GCs, but not resident GCs in the lactating mothers, exhibit more stable features (Kopel et al., 2012). Genetic ablation of bulbar ABCs in male mice leads to deficits in aggression and mating behaviors, while ablation in female mice leads to deficits in fertility and nurturing behaviors, which are known to rely on olfaction (Sakamoto et al., 2011). More studies are needed to unveil the cellular, molecular and circuitry mechanisms underlying the relationship between adult bulbar neurogenesis and pheromone-associated behaviors. Adult bulbar neurogenesis has also been related to some other olfaction-related behaviors, for example, X-ray irradiation which ablates adult bulbar neurogenesis leads to a disrupted olfactory fear conditioning (Valley et al., 2009).

To conclude, although there are some discrepancies between different behavioral analysis, which may be due to the effectiveness and specificities of different manipulations or the other differences in the experimental settings, continuous neurogenesis in the OB is critical for many olfaction-related behaviors.

1.4 The aims of this project

As described in 1.3.5, only about 50% of ABCs survive over the longer periods of time and the others die soon after arriving in the OB. It remains unknown

what governs ABC's decision to survive or to die and whether morphological and/or functional properties of ABCs can predict their subsequent fate. It has long been postulated that the death of ABCs is caused by their "failure to integrate" into the pre-existing functional circuitry but this hypothesis has never been directly tested. To examine the factors determining the survival/death of adult-born JGNs, we specifically addressed the following specific points:

1. Understanding the importance of dendritic morphogenesis for the survival of adult-born JGNs.
2. Examining the importance of odor-evoked responsiveness for the survival of adult-born JGNs;
3. Elucidating the importance of the basal Ca^{2+} level and the endogenous neuronal activity for the survival of adult-born JGNs;

2. Materials and Methods

2.1 Animals

All experiments in this project were performed in accordance with animal welfare guidelines in the University of Tübingen and were approved by the Baden-Württemberg state government in Germany. C57/BL6 mice from Charles River Laboratories were used in this study. Animals were kept in pathogen-free conditions at 22 ºC and 60% air humidity, under 12 hours light/12 hours dark cycle with *ad libitum* access to food and water. Female mice were maintained in groups of 3-5 mice, male mice were maintained individually. All experimental procedures were in accordance with the Directive 2010/63/EU of the European Parliament and the Council of the European Union.

2.2 Cranial window implantation

3 or 4-month-old C57/BL6 mice were taken from the animal facility of the University of Tübingen. Craniotomy was made above the mouse OB, as described previously (Kovalchuk et al., 2015; Liang et al., 2016; Maslyukov et al., 2018). In brief, mice were anesthetized by an intraperitoneal (i.p.) injection of a mixture (80/4 µg/g body weight (BW)) of ketamine (Fagron, Barsbuettel, Germany) and xylazine (Sigma-Aldrich, St. Louis, MO, USA). 5-10 minutes after injection, the mouse status was examined with a toe pinch response. An additional dose of ketamine/xylazine (80/2 µg/g BW) was injected if mice were not deeply anesthetized. The hair above the OB was gently shaved by a veterinarian trim without cutting whiskers. Mice were then transferred to a stereotaxic setup and head-fixed with two ear bars (Stoelting, Wood Dale, IL, USA). The body temperature was measured using a rectal temperature probe and maintained at 35-37 °C using a custom-made heating plate located under the mice. Both eyes were protected with eye ointments (Bepanthen^{TM}, Bayer, Germany) to avoid corneal dehydration. Local anesthetic lidocaine (2%, AstraZeneca, Wedel, Germany) was applied by a subcutaneous (s.c.) injection above the OB. 5 minutes after lidocaine injection, scalp above the OB was

gently removed with scissors and tweezers and the exposed skull was cleaned with standard ringer solution (in mM: 147 Na^+, 4 K^+, 2.2 Ca^{2+}, 156 Cl^-; B. Braun Melsungen AG, Germany). A circular groove (Ø 3 mm) was made above two hemispheres of the OB with a high-speed dental driller (ultimate 500, NSK). Small pieces of bones were removed with fine tweezers and gentle airflow. Ringer solution was repeatedly added and absorbed with swabs (Kettenbach GmbH, Germany) to avoid overheating, which may cause damage to the brain tissue under skull. After careful removal of the bone with fine tweezers, a glass coverslip (Ø 3 mm, Warner Instruments, Hamden, CT, USA) was gently positioned above the two bulbs. Cyanoacrylate glue was applied to the gap between coverslip and skull to stabilize coverslip. 5 minutes after cyanoacrylate glue application, the stability of coverslip was further strengthened by blue light-cured dental cement (Ivoclar Vivadent AG, Liechtenstein). Afterward, mice were placed on a heating plate until full recovery. After surgery, mice were housed individually with wet food and water supplied in a petri dish in the cage for a few days.

After the surgery, carprofen (5 µg/g BW, Pfizer, Berlin, Germany) was injected daily (s.c.) for 3 consecutive days to prevent pain and antibiotic enrofloxacin (Baytril, 1:100 v/v, Bayer, Leverkusen, Germany) was applied in drinking water for 10 consecutive days to prevent bacterial infection.

2.3 Stereotaxic viral injection and holder implantation

At least 4 weeks after window installation, window clarity and bone regrowth under the coverslip were checked under the microscope. Mice that passed the quality control were used for viral injection, as described previously (Kovalchuk et al., 2015; Liang et al., 2016). After preparing mice for surgery as described in 2.2, the scalp above the skull was gently removed with scissors and tweezers. The dental cement above injection sites was carefully removed with a high-speed dental driller. The same dental driller was used to make 2 small holes in the skull above the injection sites at the following coordinates: AP 3.0mm, ML ± 0.82 mm, DV -3.0 ± 0.05 mm from pial surface. A glass capillary (~30-40 µm in

tip diameter) filled with viral solution (~1.0-1.5 µl) was navigated to one of the injection sites. Lentivirus encoding a Förster resonance energy transfer (FRET) based ratiometric calcium indicator Twitch-2B (Maslyukov et al., 2018; Thestrup et al., 2014) or a mixture of red-green-blue (RGB) retroviruses encoding mCherry (red fluorescent protein, R), Venus (green fluorescent protein, G) and Cerulean (blue fluorescent protein, B) (1:1:1 ratio in terms of infectious titer) (Liang et al., 2016) was utilized. Twitch-2B lentivirus and RGB retroviruses were produced in accordance with the protocols described (Gomez-Nicola et al., 2014; Kovalchuk et al., 2015; Liang et al., 2016; Maslyukov et al., 2018). The glass pipette was lowered to a depth of 3.05 mm from dura. Because RMS is a tiny structure, the viral solution was injected into 3 spots (3.05 mm, 3.00 mm, 2.95 mm in depth) to increase the probability of infecting ABCs. The glass pipette remained in the injection spot for 5 minutes to allow the viral solution to diffuse in the brain tissue. After injection, the glass pipette was gently taken out from the brain tissue and the injection hole was covered with dental cement. This injection procedure was repeated for the RMS injection in the second hemisphere. Then, the exposed skull was rinsed with a standard ringer solution. A custom-made titanium holder was positioned above the skull and fixed with dental cement. The remaining exposed skull was also covered with dental cement. Carprofen (5 µg/g body weight, Pfizer, Berlin, Germany) was injected (s.c.) to kill the pain. Mice were positioned on a heating plate to recover. Wet food together with water were supplied in a petri dish in the cage.

2.4 Longitudinal *in vivo* two-photon imaging of dendritic morphology

Starting from DPI 4, mice were trained for 7 consecutive days to accustom to the two-photon imaging setup for awake imaging. For the first training day, mice were gently handled inside their home cages and then transferred to the microscope stage for at least 30 min of free exploration. From DPI 5 to DPI 11, after gentle handing and free exploration, mice were head-fixed to the microscope stage for an increasing time, from 5 min at DPI 5 to at least 30 min at DPI 11. Longitudinal *in vivo* two-photon imaging began at DPI 12.

Image acquisition was performed with a customized two-photon microscope based on an Olympus FV1000 system (Olympus, Tokyo, Japan), which is connected to a mode-locked laser (Spectra Physics, Mountain View, CA) as described (Kovalchuk et al., 2015; Liang et al., 2016; Maslyukov et al., 2018). 3D Z-stacks (512x512 pixels, Kalman-filter of 2, 3 µm step size) were taken daily from DPI 12 to DPI 35 and on DPI 44, DPI 45 to document the positions of RGB-positive adult-born JGNs in awake mice. The following procedure was chosen to excite RGB and to collect the emission light: 800 nm wavelength was used to excite Cerulean and mCherry and a 570-nm dichroic mirror to split the emission light (the short-pass channel for Cerulean and the long-pass channel for mCherry). Subsequently, we have used 970 nm wavelength to excite Venus and a 570-nm dichroic mirror to split the emission light (the short-pass channel for Venus). Because each labeled adult-born JGN has its color identity, this procedure allowed a precise tracking of individual migrating cells (Liang et al., 2016). Sparse labeling, blood vessel pattern, tiny irregularities pf the dura matter under the glass coverslip and the distance between RGB^+ cells were used as landmarks helping to identify the same cells in longitudinal imaging sessions (Gonçalves et al., 2016).

To record the dendritic morphology of RGB-labeled adult-born JGNs, mice were head-fixed in the imaging setup under isoflurane-induced anesthesia (2% for induction, 0.8-1.0% for maintenance) to prevent any animal's movements. Both eyes were protected with eye ointments (Bepanthen™, Bayer, Germany) to avoid corneal dehydration. Mouse body temperature was measured with a rectal probe and maintained at 36-37 °C by placing a heating plate under the mouse. The breath rate was monitored and kept at 100-140 BPM. Either 900 nm or 970 nm excitation wavelength was chosen based on the fluorescent proteins each cell expressed. 3D Z-stacks (512x512 pixels, Kalman-filter of 3, step size 2 µm) with appropriate zoom factors were recorded to cover the intact dendritic morphology.

2.5 Longitudinal *in vivo* two-photon calcium imaging

Action potentials produce generalized calcium accumulations throughout the neuron. The imaging of calcium influx into neurons with calcium indicators provides an indirect but accurate measure of action potential spiking of the individual neuron (Yuste et al., 2011). Twitch-2B, composed of a donor fluorescent protein (mCerulean3, a brighter variant of CFP), a calcium-binding domain (Troponin C) and an acceptor fluorescent protein (cpVenus^{CD}, a brighter variant of YFP), is a genetically encoded ratiometric calcium indicator and exhibits the near-linear relationship between fluorescence change and action potential numbers in the physiological spiking range and can minimize artifacts caused by animal's movements (Thestrup et al., 2014; Wilms and Häusser, 2014). These properties make Twitch-2B particularly valuable for long-term *in vivo* calcium imaging experiments, no matter whether animals are awake or anesthetized.

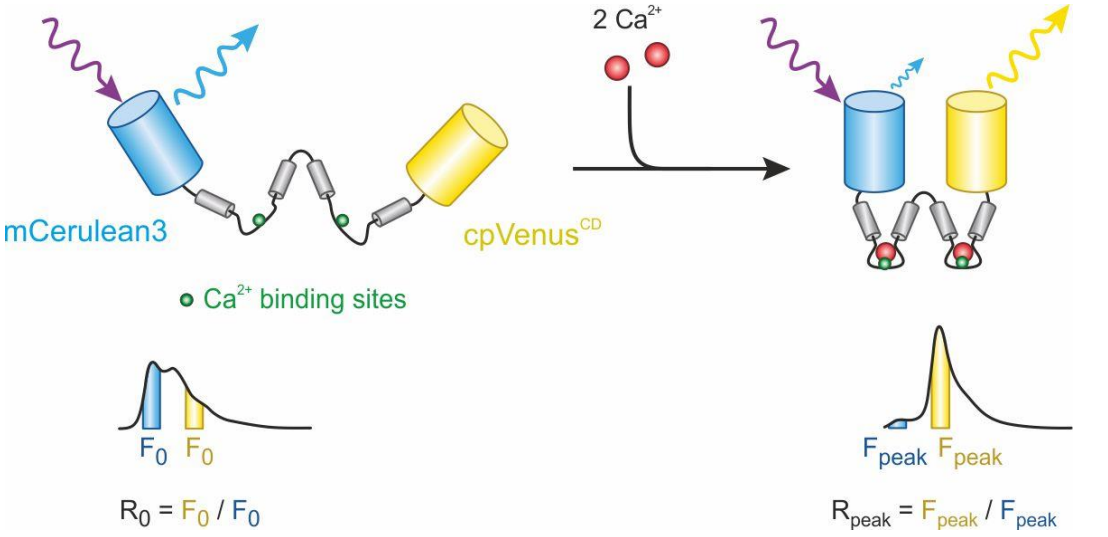

Figure 6. Schematic drawing showing the working principle of calcium indicator Twitch-2B. Twitch-2B is a Förster resonance energy transfer (FRET) based ratiometric calcium indicator, which is composed of a donor fluorophore mCerulean3 (indicated by blue color, a brighter variant of CFP), an acceptor fluorophore cpVenus^{CD} (indicated by a yellow color, a brighter variant of YFP), and a troponin C-derived calcium-binding domain. Upon excitation without binding Ca^{2+} ions, mCerulean3 and cpVenus^{CD} emit photons independently. When binding 2 Ca^{2+} ions, Twitch-2B changes its conformation and the distance between these two fluorophores becomes shorter. Upon excitation by a specific wavelength, the shorter distance enables FRET to occur between mCerulean3 and cpVenus^{CD} fluorophores, causes a decrease in the fluorescence of mCerulean3 and a concomitant increase in the fluorescence of cpVenus^{CD}. Thus, the increase of the mCerulean3/cpVenus^{CD} ratio corresponds to an increase of the free intracellular Ca^{2+} concentration, modified from (Wilms and Häusser, 2014).

11 days post-viral injection (DPI 11), a training period started, allowing mice to accustom to the experimenter and the two-photon microscope setup for awake imaging, as described in 2.4. The emitted light was collected through a Zeiss 20x water immersion objective (NA 1.00) (Zeiss, Jena, Germany). When mice were awake and head-fixed, 3-dimensional (3D) Z-stacks (512x512 pixels, Kalman-filter of 2, 3 µm step size) from the dura mater to a depth of 240 µm were acquired every second day from DPI 18 to DPI 44/45 to document the positions of Twitch-2B-positive (Twitch-2B^{+}) cells. 930 nm excitation wavelength was chosen to excite Twitch-2B.

Endogenous activity of adult-born JGNs (2-min-long recordings, 6.67 Hz sampling rate) was recorded in awake mice with 890 nm excitation wavelength. Fluorescence signals from mCerulean and cpVenus^{CD} were split by a 515-nm dichroic mirror. A 475/64 nm band-pass filter and a 500 nm long-pass filter (Semrock, Rochester, United States) were used to block reflected light and transmit the mCerulean and cpVenus^{CD} emission light, respectively. During one imaging session, mice were head-fixed in the setup for no more than 2 hours.

2.6 Odor application

Examinations of odor-evoked responses were performed as described earlier (Kovalchuk et al., 2015; Maslyukov et al., 2018). In brief, mouse was deeply anesthetized with a mixture of midazolam (5 mg/kg BW), medetomidine (0.5 mg/kg BW), and fentanyl (0.05 mg/kg BW) by i.p. injection. After head-fixation in the imaging setup with a heating plate under the mouse, both eyes were protected with eye ointments (Bepanthen^{TM}, Bayer, Germany) to avoid corneal dehydration. Mouse body temperature was monitored with a rectal probe and maintained at 36-37 °C. Breath rate was kept at 100-160 breaths per minute (BPM). Twitch-2B^{+} cells were imaged with 890 nm excitation light. A custom-made flow dilution olfactometer was used to deliver a mixture consisting of the equal parts of either 3 (isoamyl acetate, 2-hexanone and 3 ethyl tiglate) or 7 (ethyl-acetate, butanal, pentanal, ethyltiglate, propanal, methyl-propionate and ethyl-butyrate) odorants, which can achieve broad activation of dorsal OB

glomeruli (Kovalchuk et al., 2015; Livneh et al., 2014). Odorants (1.7% of saturated vapor) were presented as a 4-second-long pulse in front of the mouse's snout while capturing time-lapsed images (6.67 Hz) of target cells. There was at least a 5-minute-long interval between different odor applications. The odors used in this study were provided by Sigma-Aldrich at the highest commercially available purity. For each mouse, odorants were applied twice, with the 1st application at DPI 20 to DPI 25 and the 2nd application at DPI 28 to DPI 32.

2.7 Analysis

Offline data analysis was performed with Olympus Fluoviewer (Olympus, Tokyo, Japan), ImageJ (https://imagej.nih.gov/ij/), Igor Pro (WaveMetrics, Portland, United States), 4DSPA software (Lee et al., 2013) and custom-made routines in Matlab (The MathWorks, Inc., Natick, Massachusetts, United States).

2.7.1 Analysis of dendritic morphology

TIFF image stacks of dendritic morphology were imported into Image J. Neuronal soma and dendrites were manually traced to have accurate reconstructions and analyzed with Simple Neurite Tracer plugin. Cells with incomplete dendritic arborizations were not taken for analysis. Dendritic 3D reconstructions were analyzed with Neuromantic (Myatt et al., 2012) as well as Analyze skeleton plugin in Image J. Number of primary dendrites, number of dendritic branches, total dendritic branch length (TDBL) of all dendritic branches, number of branch points and number of dendritic endings (last segments between the dendritic tip and a branch point) were quantified.

Newly-added and pruned dendritic endings were analyzed with the 4D structural plasticity analysis (4DSPA) software (Lee et al., 2013). Specifically, morphologies (swc files) reconstructed with the Simple Neurite Tracer plugin in Image J were converted to Neurolucida ASC files with NLMorphologyConverter (http://neuronland.org/NLMorphologyConverter/NLMorphologyConverter.html). ASC files were then converted to TXT files with Eigen converter, which was

kindly provided by the developers of the 4DSPA software. TXT files can be opened with the 4DSPA software and a comparison of branch morphology between 2 neighboring time points (one group) was made according to the established procedure (Gonçalves et al., 2016; Lee et al., 2013). Results were further processed in Matlab.

2.7.2 Analysis of endogenous activity

For the analysis of endogenous activity, TIFF time-lapse images were imported into Image J. A region of interest (ROI) was drawn for each cell based on the shape of its soma. A background ROI was drawn in the area near the target cell. Thereafter, TIFF images were split into mCerulean3 and cpVenus^{CD} channels and fluorescence intensity values for these two channels were calculated. The fluorescence intensity values were imported into Matlab and filtered with a 1st order low-pass digital Butterworth filter with a cutoff frequency of 0.6 Hz. Twitch-2B ratio was calculated using the following formula:

$$\text{Ratio} = \frac{F(\text{cpVenus}^{CD})_{Soma} - F(\text{cpVenus}^{CD})_{Background}}{F(\text{mCerulean3})_{Soma} - F(\text{mCerulean3})_{Background}}$$

The following parameters were analyzed: basal Twitch-2B ratio, maximum Twitch-2B ratio, maximum ΔR/R amplitude, area under the curve (AUC) per second, fraction of time spent above 2.4, fraction of time spent below 2.0. The values for basal and maximum ratios were calculated as follows: the filtered traces were processed by a sliding average algorithm with a window size of 5 seconds to determine the basal ratio (minimum average value) and 1.5 seconds to determine the maximum ratio (maximum average value) in the Matlab. ΔR/R was calculated as (R-R0)/R0, where R0 is the basal ratio.

The difference in fluctuation patterns has been used to compare eliminated and surviving adult-born JGNs. Fluctuations in the endogenous activity traces have been detected using the mid-reference level crossing approach (2003). In the following, the fluctuation degree has been quantified using the number of crossing points passing through the mid-reference level (2003). The Gaussian mixture model (McLachlan and Peel, 2000) has been used to explore and

detect the naturally existing clusters in the counted crossing points. In the given clustering technique, the correct number of clusters has been estimated using Bayesian Information Criteria (Wit et al., 2012). Assigned labels have been used to calculate the portion of each cluster in eliminated and surviving adult-born JGNs and these fractions are compared statistically using the Chi-square test with Yates' correction. Note that in some mice, there are more than one cells eliminated at different time points, endogenous activity traces of the same surviving adult-born JGNs in these mice at these different time points were respectively clustered.

2.7.3 Analysis of odor-evoked responses

As described in 2.7.1, TIFF images were open with Image J and separated into mCerulean3 and cpVenus^{CD} channels. After background subtraction as described in 2.7.1, ΔR/R amplitude was calculated based on the Twitch-2B ratio in Igor Pro. Odor responsiveness of adult-born JGNs was automatically detected according to the protocol described (Homma et al., 2013; Kovalchuk et al., 2015). In brief, all ΔR/R traces were processed with a binomial filter, and the filtered traces were subtracted from ΔR/R traces to give the baseline noise trace. A template-matching algorithm was used to automatically define calcium transients. Cells were defined as odor-responding if their ΔR/R amplitudes were three times larger than the standard deviation of the corresponding background noise.

2.7.4 Data and statistical analyses

Box plots illustrate the median ± interquartile range (IQR) of the respective dataset. Statistics were performed with GraphPad Prism 7 (GraphPad Software, Inc.). Shapiro-Wilk test was adopted to check the normality of individual datasets. For one dataset, One sample *t* test or Wilcoxon signed rank test was applied based on the normality of the dataset. For two unpaired not normally distributed datasets, nonparametric Mann-Whitney test was used. For two unpaired normally distributed datasets, after checking heterogeneity of variances with F test, unpaired student's *t* test with or without Welch’s correction

was applied. For two paired not normally distributed datasets, Wilcoxon matched-pairs signed rank test was used. For two paired normally distributed datasets, paired student's *t* test was applied. For three or more paired not normally distributed datasets, Friedman test followed by Dunn's multiple comparisons test was used. For three or more paired normally distributed datasets, after checking heterogeneity of variances with Bartlett's test, One-way repeated measures ANOVA with or without Greenhause-Geisser Sphericity Correction followed by Holm-Sidak post hoc test was used. Unless indicated, all statistical tests were two-tailed. Differences were considered significant if $P < 0.05$.

3. Results

3.1 Longitudinal *in vivo* fate mapping of adult-born JGNs with RGB labeling

As it has been reported by immunohistochemical data, ~50% of adult-born JGNs are eliminated from 15 to 45 days after their birth (Mouret et al., 2009; Whitman and Greer, 2007a, 2009). However, according to the data from our lab, adult-born JGNs undergo vivid lateral migration after arrival in the glomerular layer at early time points (e.g. 15 days after their birth), see Figure 7C in (Liang et al., 2016). To achieve a precise identification of migrating adult-born JGNs in longitudinal experiments at early time points, we chose the well-established red-green-blue (RGB) cell-marking approach in the lab, labeling neuroblasts via an RMS injection of a mixture of retroviruses encoding mCherry (red), Venus (green) and Cerulean (blue) (Figure 7A) (Gomez-Nicola et al., 2014; Liang et al., 2016). This multi-color RGB labeling technique provides each labeled cell a unique color identity, thus enabling accurate tracking of migrating cells over a long period of time (Gomez-Nicola et al., 2014; Liang et al., 2016). Color-coded adult-born JGNs were visualized through a cranial window with two-photon (2P) microscopy (Figure 1C).

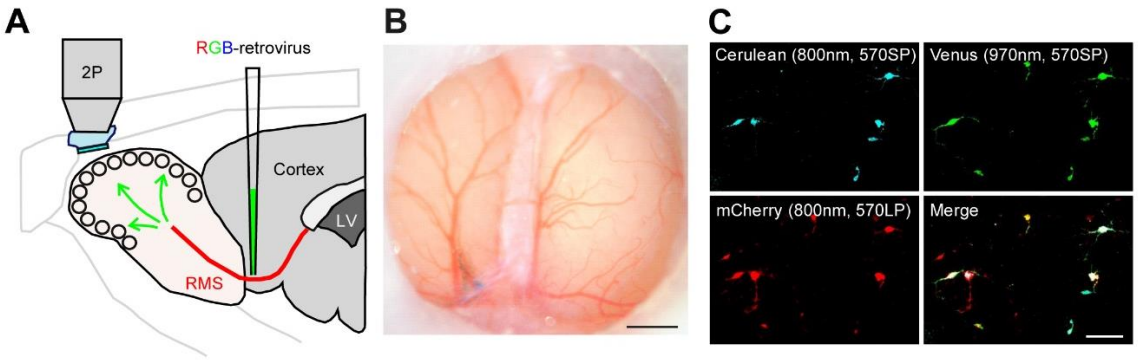

Figure 7. RGB multi-color labeling and *in vivo* imaging of adult-born JGNs. (**A**) Scheme of the experimental setup. Adult-born JGNs were labeled via RMS injection of a 1:1:1 mixture of retroviruses encoding Cerulean (blue), Venus (green) and mCherry (red) fluorescent proteins (RGB labeling) and repeatedly imaged via a chronic cranial window by means of two-photon (2P) microscopy. (**B**) A representative example of a glass cranial window on the OB. (**C**) Maximum intensity projection (MIP) images (0-100 µm, step 2 µm) of RGB-labeled adult-born JGNs taken at DPI 12 in blue, green and red channels. 800 nm excitation wavelength was used to efficiently excite Cerulean and mCherry, while 970 nm excitation wavelength was used to excite Venus. A 570 nm dichroic mirror was used to split emission light. The merged image is shown in the lower right corner. SP, short pass chanel; LP, long pass chanel. Scale bar: 50 µm.

To cover the entire period of adult-born JGN elimination (15 to 45 days after birth), we started our longitudinal experiments at 12 days post injection (DPI 12). Positions together with dendritic morphology of RGB-labeled adult-born JGNs were longitudinally and recurrently imaged from DPI 12 to DPI 45, as outlined in Figure 8A. Because of the extensive lateral migration of adult-born JGNs at early time points, we imaged RGB-labeled adult-born JGNs every day from DPI 12 to DPI 35 and imaged these cells again at DPI 44, 45. To develop the criteria for cell elimination, we made use of the prior knowledge showing that adult-born JGNs rarely migrate after being stable for more than 4 days (Figure 4 in (Liang et al., 2016)) and left a 30-50 µm wide margin to the border of each field of view (FOV), not to mistake cell migration for cell elimination. Thus, adult-born JGNs were scored as eliminated if either (i) cell debris was found in the position where an adult-born JGN was previously located (upper panel in Figure 8B) or (ii) a cell appeared in the FOV at DPI 12, stayed in the same position at DPI 18-22 (at least 4 days) and then disappeared from the dorsal surface of the bulb under the entire cranial window (lower panel in Figure 8B). We often noticed that debris of cells expressing mCherry together with other fluorescent proteins (i.e. the upper cell in Figure 8B, upper panel) was colored red, likely due to the resistance of mCherry to proteolysis and degradation (Costantini et al., 2015). Based on the criteria listed above, RGB-labeled adult-born JGNs were classified into 3 groups: surviving cells (i.e. cells staying in their positions within the FOV till DPI 45, the end of the longitudinal imaging), eliminated cells and cells whose fate was uncertain (i.e. either eliminated without fulfilling the above criteria or rapidly migrating out of the cranial window between two imaging sessions). To avoid the false-positive results, we excluded the uncertain cells from further analyses. Note, this might cause an underestimation of the fraction of eliminated cells.

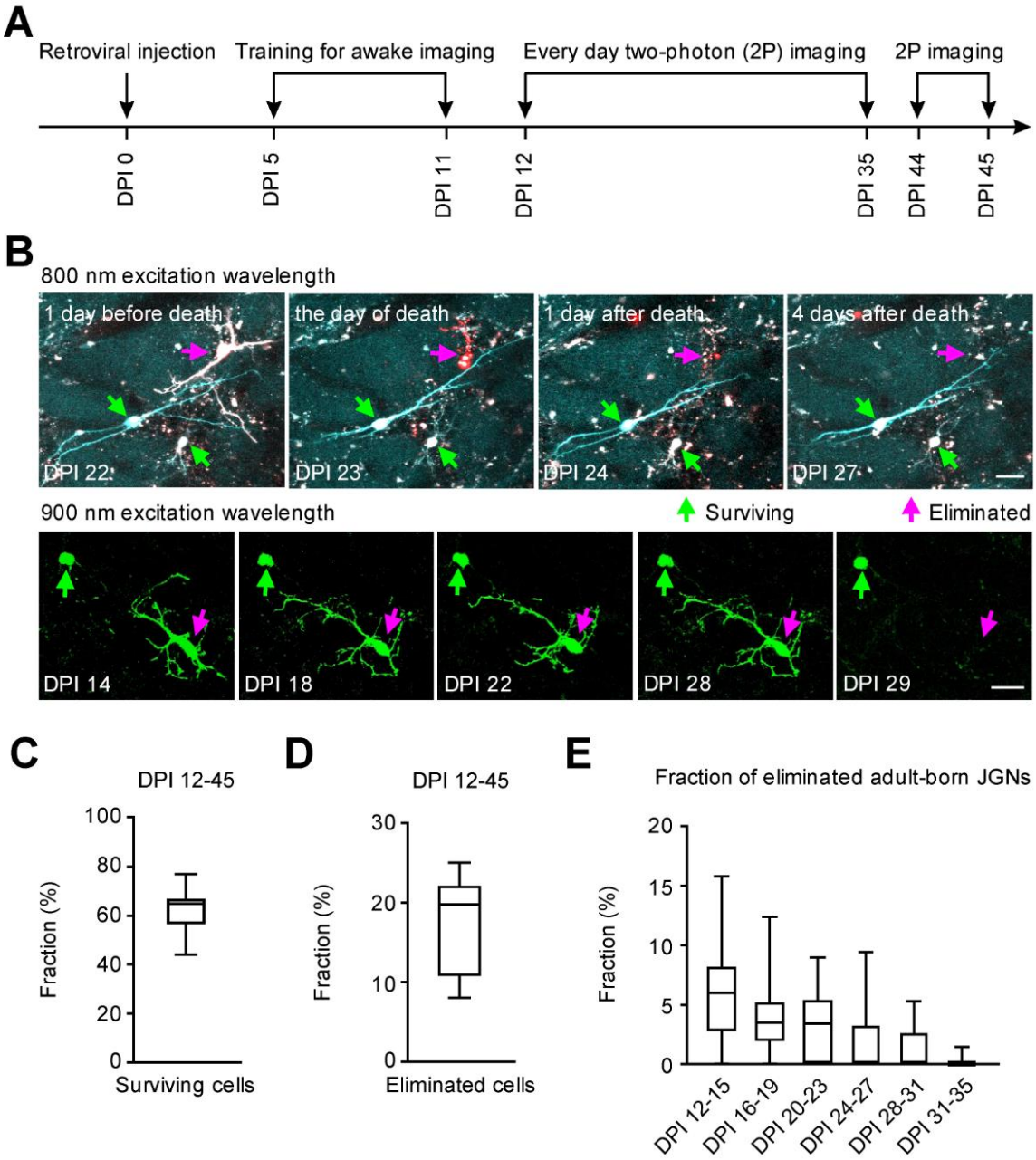

Figure 8. Longitudinal fate mapping of adult-born JGNs with *in vivo* 2P microscopy. (**A**) Schematic illustration of the experimental timeline (see Material and Methods for more details). (**B**) Upper: MIP images (34-54 µm, step 2 µm, 800 nm excitation wavelength) showing 1 eliminated cell (magenta arrow) and 2 surviving cells (green arrows) in the same FOV at 4 time points: DPI 22 (1 day before death), DPI 23 (the day of death), DPI 24 (1 day after death) and DPI 27 (4 days after death). Note red cell debris visible at DPI 23 and DPI 24. Lower: MIP images (12-52 µm, step 2 µm, 900 nm excitation wavelength) illustrating 1 eliminated and 1 surviving adult-born JGNs in the same FOV at 5 different time points. DPI 29 was defined as the day of death. Scale bars: 25 µm. (**C, D**) Box plots showing the median (per mouse) fractions of surviving (**C**) and eliminated (**D**) adult-born JGNs at DPI 12-45 (n = 12 mice). (**E**) Box plot showing the median (per mouse) fractions of adult-born JGNs, eliminated at different time points (n = 12 mice).

With the above criteria, 63.97 ± 11.29% (per mouse, median ± IQR) of 528 analyzed adult-born JGNs were classified as surviving cells (Figure 8C), 18.45 ± 12.89% were classified as eliminated cells (Figure 8D) and the rest were classified as uncertain cells (n = 12 mice). Interestingly, the fraction of eliminated adult-born JGNs decreased over the analyzed time period (DPI 12-45) with no adult-born JGNs being eliminated after DPI 36 (Figure 8E, 91 eliminated cells, n = 12 mice). In total, 91.51% of eliminated adult-born JGNs (83/91 cells) were eliminated before DPI 28. This data is consistent with the previous *in vivo* study showing that the elimination of adult-born JGNs after DPI 28 is minimal (~4%) (Sawada et al., 2011). Our data demonstrated that the elimination of adult-born JGNs was cell age-dependent, with more eliminated cells at younger ages and less eliminated cells when adult-born JGNs became more mature.

Taken together, our data demonstrated that at least ~20% of adult-born JGNs can be eliminated in the OB after DPI 12 and the elimination of adult-born JGNs was cell age-dependent. We found ~5% of adult-born JGNs were eliminated at DPI 12-15 and no cell eliminated after DPI 36, suggesting the period of adult-born JGN elimination in the OB seems to start earlier than assumed previously and last till DPI 36 only.

3.2 Development of the dendritic tree in adult-born JGNs

To understand how the decision to die or to survive is made, next, we asked which features of immature adult-born JGNs can predict their fate. To begin with, we focused on dendritic morphology. Although it has been reported that at the population level the dendritic trees of mature adult-born JGNs at DPI 43 and DPI 45 are more complex than those of immature adult-born JGNs at DPI 10 and DPI 13 (Livneh et al., 2009, 2014; Mizrahi, 2007, 2007), longitudinal analysis of dendritic development of individual adult-born JGNs is still lacking. In this study, the following morphological parameters (schematically illustrated in Figure 9A) were quantified: total dendritic branch length (TDBL), number of dendrites, number of primary dendrites, number of branch points and number of

dendritic endings. Based on the number of primary dendrites, adult-born JGNs are classified either as unipolar or as multipolar cells (Figure 9B). We found a significant increase in the median (per mouse) fraction of unipolar adult-born JGNs at DPI 45 when compared with the fraction of unipolar cells at DPI 13 (Figure 9C, P = 0.0049, Wilcoxon signed rank test, n = 11 mice). There are 2 possibilities: either (i) multipolar cells pruned their primary dendrites to become unipolar cells or (ii) unipolarity of dendritic tree is beneficial for cell survival and more multipolar cells were eliminated at DPI 13-45. Out of all eliminated and surviving adult-born JGNs with documented dendritic morphology, 22.5% (9/40 cells, n = 11 mice) of eliminated adult-born JGNs and a smaller fraction of cells (12.16%, 18/148 cells, n = 12 mice) had a unipolar dendritic tree at DPI 13. The observed difference between surviving and eliminated cells in terms of the fraction of unipolar cells at DPI 13, however, did not reach the level of statistical significance (Figure 9D, P = 0.16, Chi-square test with Yates' correction), suggesting that unipolarity of dendritic tree is not an advantage for the survival of adult-born JGNs. These data also suggested that the higher fraction of unipolar cells observed at DPI 45 (Figure 9C) was not caused by the enhanced elimination of multipolar cells during DPI 13 and DPI 45.

For a detailed dendritic tree analysis, we considered the surviving cells that did not move their positions during DPI 13 and DPI 45 as stable surviving cells (69.62 ± 12.12% from all surviving cells, n = 12 mice). We first analyzed the dendritic morphology of these stable surviving cells and then took their morphology as a reference to analyze which morphological features of eliminated adult-born JGNs might predict their fate. To do so, we reconstructed and analyzed the dendritic trees of stable surviving adult-born JGNs at the following 12 time points: DPI 13, DPI 14, DPI 17, DPI 18, DPI 21, DPI 22, DPI 27, DPI 28, DPI 34, DPI 35, DPI 44, DPI 45 (Figure 10A). For each cell, the data were normalized to the respective value measured at DPI 13 and means of 2 neighboring time points were taken for statistics shown in Figure 10B-F.

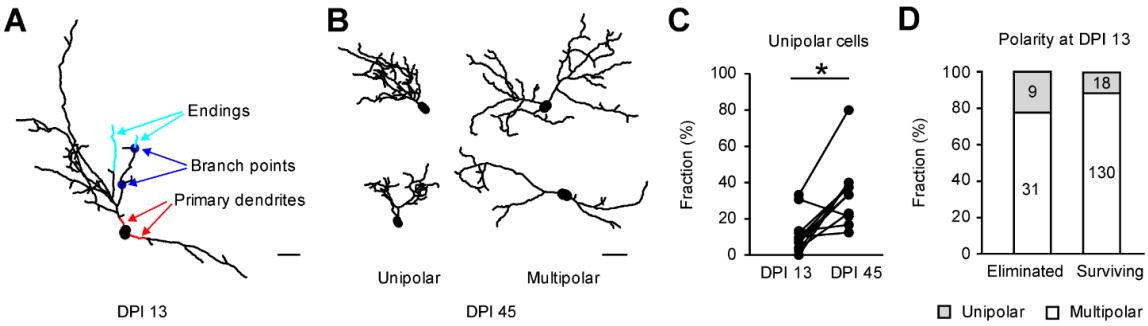

Figure 9. The polarity of adult-born JGN's dendritic morphology. (**A**) 2D projection image of a reconstructed adult-born JGN (DPI 13) illustrating the morphological parameters analyzed in this study. Primary dendrites are colored red, branch points are colored blue, dendritic endings are colored cyan (see Methods for further details). Scale bar: 25 µm. (**B**) Representative reconstructions of 2 unipolar and 2 multipolar cells at DPI 45. Scale bar: 25 µm. (**C**) Connected dot graph showing the fractions of unipolar cells at DPI 13 and DPI 45 (P = 0.0049, Wilcoxon signed rank test, n = 11 mice). (**D**) Bar graphs showing fractions of unipolar and multipolar cells among the eliminated and surviving cells (40 eliminated cells from 11 mice, 148 surviving cells from 12 mice). Cell morphology was evaluated at DPI 13.

Strikingly, all analyzed parameters of stable surviving adult-born JGNs including the median (per mouse) TDBL, number of dendrites, number of primary dendrites, number of branch points and number of endings declined from DPI 13 to DPI 45 (Figure 10B-F, n = 34 cells from 8 mice), indicating that the dendritic complexity of adult-born JGNs decreased during the process of maturation. The reduction in the number of primary dendrites is consistent with the increased fraction of unipolar cells seen at DPI 45 (Figure 9C). Consistently, Sholl analysis also revealed a significant reduction in the dendritic complexity at DPI 45, when compared to DPI 13 (Figure 10G,H).

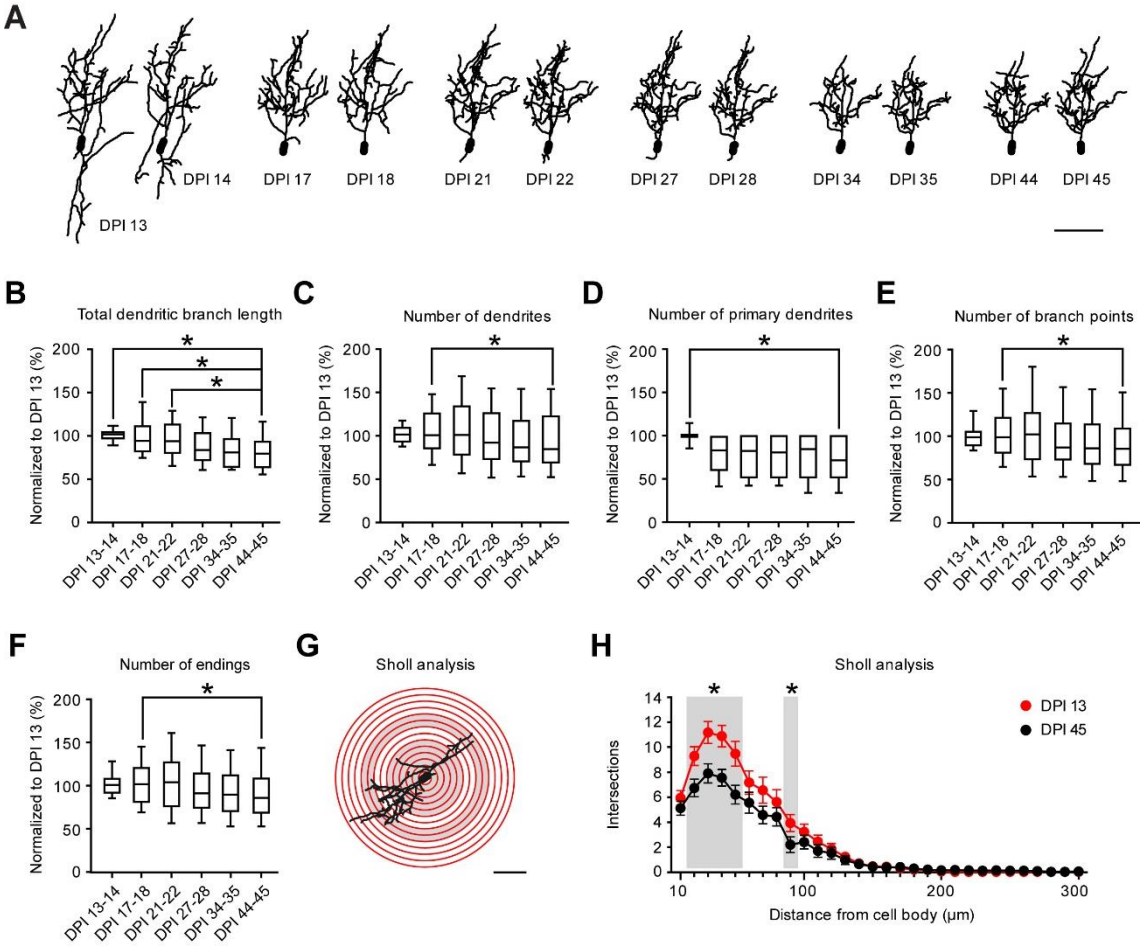

Figure 10. Development of the dendritic tree in stable surviving adult-born JGNs. (**A**) Representative reconstructions of the same cell at 12 different time points. Scale bar: 50 µm. (**B**-**F**) Box plots illustrating median (per cell) total dendritic branch length (**B**), numbers of dendrites (**C**), primary dendrites (**D**), branch points (**E**) and endings (**F**). For each cell, the data were normalized to the respective value measured at DPI 13 ($P < 0.05$, Friedman test followed by Dunn's multiple comparisons test, n = 34 cells, 8 mice). (**G**) Schematic diagram illustrating the Sholl analysis procedure. Scale bar: 30 µm. (**H**) Graph comparing the mean numbers of intersections with Sholl spheres for cells imaged at DPI 13 (red) and DPI 45 (black) ($P < 0.05$, Wilcoxon signed rank test, n = 34 cells, 8 mice). Error bars represent SEM. Grey zones in (**G**) and (**H**) indicate the regions where the numbers of intersections showed significant differences at DPI 13 compared to DPI 45.

Table 1. Summary of morphological data and *P* values in Figure 10.

Figure	Data (median ± IQR)	*P* values
Figure 10B	DPI 13-14: 101.8 ± 18.22% DPI 17-18: 101.0 ± 42.4% DPI 21-22: 101.5 ± 57.74% DPI 27-28: 92.58 ± 55.39% DPI 34-35: 87.22 ± 48.69% DPI 44-45: 85.32 ± 55.36%	DPI 13-14 VS. DPI 44-45: $P = 0.21$ DPI 17-18 VS. DPI 44-45: $P = 0.0067$ DPI 21-22 VS. DPI 44-45: $P = 0.063$ DPI 27-28 VS. DPI 44-45: $P > 0.99$ DPI 34-35 VS. DPI 44-45: $P > 0.99$
Figure 10C	DPI 13-14: 100 ± 0% DPI 17-18: 83.33 ± 40.62% DPI 21-22: 81.67 ± 50% DPI 27-28: 80± 50%	DPI 13-14 VS. DPI 44-45: $P < 0.001$ DPI 17-18 VS. DPI 44-45: $P = 0.26$ DPI 21-22 VS. DPI 44-45: $P = 0.4$

	DPI 34-35: 83.75 ± 50% DPI 44-45: 70.84 ± 50%	DPI 27-28 VS. DPI 44-45: $P = 0.73$ DPI 34-35 VS. DPI 44-45: $P > 0.99$
Figure 10D	DPI 13-14: 101.9 ± 8.16% DPI 17-18: 94.54 ± 29.34% DPI 21-22: 94.15 ± 33.78% DPI 27-28: 84.06 ± 31.99% DPI 34-35: 81.29 ± 33.29% DPI 44-45: 79.82 ± 30.44%	DPI 13-14 VS. DPI 44-45: $P < 0.001$ DPI 17-18 VS. DPI 44-45: $P < 0.001$ DPI 21-22 VS. DPI 44-45: $P < 0.001$ DPI 27-28 VS. DPI 44-45: $P = 0.46$ DPI 34-35 VS. DPI 44-45: $P > 0.99$
Figure 10E	DPI 13-14: 99.43 ± 16.78% DPI 17-18: 99.36 ± 41.38% DPI 21-22: 103 ± 54.43% DPI 27-28: 87.75 ± 42.56% DPI 34-35: 86.82± 46.54% DPI 44-45: 86.31± 42.85%	DPI 13-14 VS. DPI 44-45: $P = 0.12$ DPI 17-18 VS. DPI 44-45: $P = 0.018$ DPI 21-22 VS. DPI 44-45: $P = 0.11$ DPI 27-28 VS. DPI 44-45: $P > 0.99$ DPI 34-35 VS. DPI 44-45: $P > 0.99$
Figure 10F	DPI 13-14: 100 ± 17.33% DPI 17-18: 100.9 ± 40.43% DPI 21-22: 103.1 ± 51.73% DPI 27-28: 90.18 ± 40.82% DPI 34-35: 88.75± 42.5% DPI 44-45: 85.09 ± 40.63%	DPI 13-14 VS. DPI 44-45: $P = 0.12$ DPI 17-18 VS. DPI 44-45: $P = 0.032$ DPI 21-22 VS. DPI 44-45: $P = 0.26$ DPI 27-28 VS. DPI 44-45: $P > 0.99$ DPI 34-35 VS. DPI 44-45: $P > 0.99$
Figure 10H	Mean ± SEM 10 µm: 6.07 ± 0.64 (DPI 13), 5 ± 0.53 (DPI 45) 20 µm: 9.29 ± 0.76 (DPI 13), 6.74 ± 0.7 (DPI 45) 30 µm: 11.18 ± 0.88 (DPI 13), 7.91 ± 0.76 (DPI 45) 40 µm: 10.88 ± 0.87 (DPI 13), 7.56 ± 0.65 (DPI 45) 50 µm: 9.47 ± 1 (DPI 13), 6.21 ± 0.75 (DPI 45) 60 µm: 7.48 ± 1 (DPI 13), 6 ± 0.88 (DPI 45) 70 µm: 6.56 ± 1.03 (DPI 13), 4.59 ± 0.71 (DPI 45) 80 µm: 6.03 ± 1.06 (DPI 13), 4.84 ± 0.77 (DPI 45) 90 µm: 3.94 ± 0.68 (DPI 13), 2.21 ± 0.63 (DPI 45) 100 µm: 3.24 ± 0.62 (DPI 13), 2.4 ± 0.54 (DPI 45)	DPI 13 VS. DPI 45 10 µm: $P = 0.18$ 20 µm: $P = 0.031$ 30 µm: $P = 0.0096$ 40 µm: $P = 0.0065$ 50 µm: $P = 0.01$ 60 µm: $P = 0.12$ 70 µm: $P = 0.065$ 80 µm: $P = 0.21$ 90 µm: $P = 0.014$ 100 µm: $P = 0.30$

Further, to investigate the turnover of dendritic branches, we conducted quantitative 4D structural plasticity analyses (4DSPA), using previously published protocols (Gonçalves et al., 2016; Lee et al., 2013). We analyzed the added and pruned dendritic endings of the same neuron at 6 different 1-day time windows (Figure 11A). Our data showed that stable surviving adult-born JGNs underwent extensive dendritic remodeling at early time points and the degree of structural plasticity decreased over time (Figure 11B-E). Consistent

with the literature data (Livneh and Mizrahi, 2011; Mizrahi, 2007), mature adult-born JGNs (DPI 44-45) remained structurally dynamic (Figure 11).

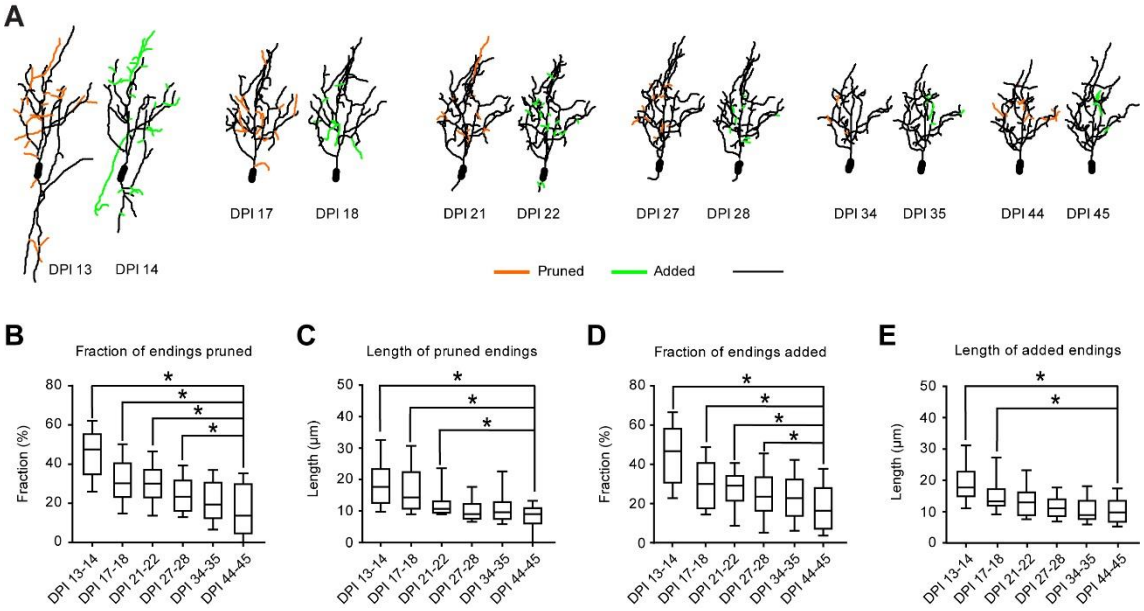

Figure 11. Dendritic remodeling of stable surviving adult-born JGNs. (**A**) Representative reconstructions of the same cell at 12 different time points (groups of 2 consecutive time points). Colors highlight pruned (orange) and added (green) dendrites for each group. Scale bar: 50 µm. (**B**-**E**) Box plots showing the median (per cell) fraction of endings pruned ($P < 0.05$, One-way repeated measures ANOVA followed by Holm-Sidak's multiple comparisons test) (**B**), length of pruned endings ($P < 0.05$, Friedman test followed by Dunn's multiple comparisons test) (**C**), fraction of endings added ($P < 0.05$, One-way repeated measures ANOVA followed by Holm-Sidak's multiple comparisons test) (**D**) and median length of added endings ($P < 0.05$, Friedman test followed by Dunn's multiple comparisons test) (**E**) in stable surviving adult-born JGNs (n = 34 cells, 8 mice).

Table 2. Summary of dendritic remodeling data and *P* values in Figure 11.

Figure	Data (median ± IQR)	*P* values
Figure 11B	DPI 13-14: 48.06 ± 20.86% DPI 17-18: 30.6 ± 17.47% DPI 21-22: 30.42 ± 14.29% DPI 27-28: 23.67 ± 15.79% DPI 34-35: 19.62 ± 18.33% DPI 44-45: 13.85 ± 25.46%	DPI 13-14 VS. DPI 44-45: $P < 0.0001$ DPI 17-18 VS. DPI 44-45: $P < 0.0001$ DPI 21-22 VS. DPI 44-45: $P < 0.0001$ DPI 27-28 VS. DPI 44-45: $P = 0.0056$ DPI 34-35 VS. DPI 44-45: $P = 0.086$
Figure 11C	DPI 13-14: 17.75 ± 10.77 µm DPI 17-18: 14.39 ± 11.64 µm DPI 21-22: 10.78 ± 3.72 µm DPI 27-28: 9.13 ± 4.73 µm DPI 34-35: 9.69 ± 5.36 µm DPI 44-45: 9.12 ± 4.96 µm	DPI 13-14 VS. DPI 44-45: $P < 0.0001$ DPI 17-18 VS. DPI 44-45: $P < 0.0001$ DPI 21-22 VS. DPI 44-45: $P = 0.0033$ DPI 27-28 VS. DPI 44-45: $P = 0.18$ DPI 34-35 VS. DPI 44-45: $P = 0.3$
Figure 11D	DPI 13-14: 46.83 ± 27.45% DPI 17-18: 30.15 ± 23.05% DPI 21-22: 29.18 ± 12.62% DPI 27-28: 23.67 ± 17.05% DPI 34-35: 22.92 ± 18.46% DPI 44-45: 16.48 ± 20.75%	DPI 13-14 VS. DPI 44-45: $P < 0.0001$ DPI 17-18 VS. DPI 44-45: $P < 0.0001$ DPI 21-22 VS. DPI 44-45: $P = 0.0026$ DPI 27-28 VS. DPI 44-45: $P = 0.022$ DPI 34-35 VS. DPI 44-45: $P = 0.054$

Figure 11E	DPI 13-14: 17.72 ± 7.86 µm DPI 17-18: 13.33 ± 5.28 µm DPI 21-22: 13.01 ± 7.35 µm DPI 27-28: 11.08 ± 5.42 µm DPI 34-35: 8.96 ± 5.84 µm DPI 44-45: 9.87 ± 6.74 µm	DPI 13-14 VS.DPI 44-45: $P < 0.0001$ DPI 17-18 VS. DPI 44-45: $P < 0.0001$ DPI 21-22 VS. DPI 44-45: $P = 0.22$ DPI 27-28 VS. DPI 44-45: $P > 0.99$ DPI 34-35 VS. DPI 44-45: $P > 0.99$

As mentioned in the introduction section, adult-born JGNs comprise two subtypes of cells: adult-born periglomerular cells (PGCs) and adult-born short axon cells (SACs). Because these two subtypes have distinct dendritic morphology (Kiyokage et al., 2010; Nagayama et al., 2010; Pinching and Powell, 1971), we identified adult-born PGCs and adult-born SACs based on their dendritic morphology at DPI 45 and characterized the dendritic development in each subtype from DPI 13 to DPI 45. In general, the patterns of morphological development were similar in stable surviving adult-born PGCs (Figure 12, n = 13 PGCs from 7 mice) and stable surviving adult-born SACs (Figure 13, n = 14 SACs from 5 mice). Both cell types exhibited a significant reduction in the TDBL as well as the number of primary dendrites from DPI 13 to DPI 45, meaning both subtypes showed a decreasing trend in the complexity of dendritic morphology at DPI 13-45. We also observed a developmental decrease in the degree of dendritic remodeling in both subtypes, like adult-born JGNs in Figure 11. For the first time, our data indicated that adult-born PGCs and SACs share similar patterns of dendritic development, regardless of the fact that they have distinct dendritic morphology.

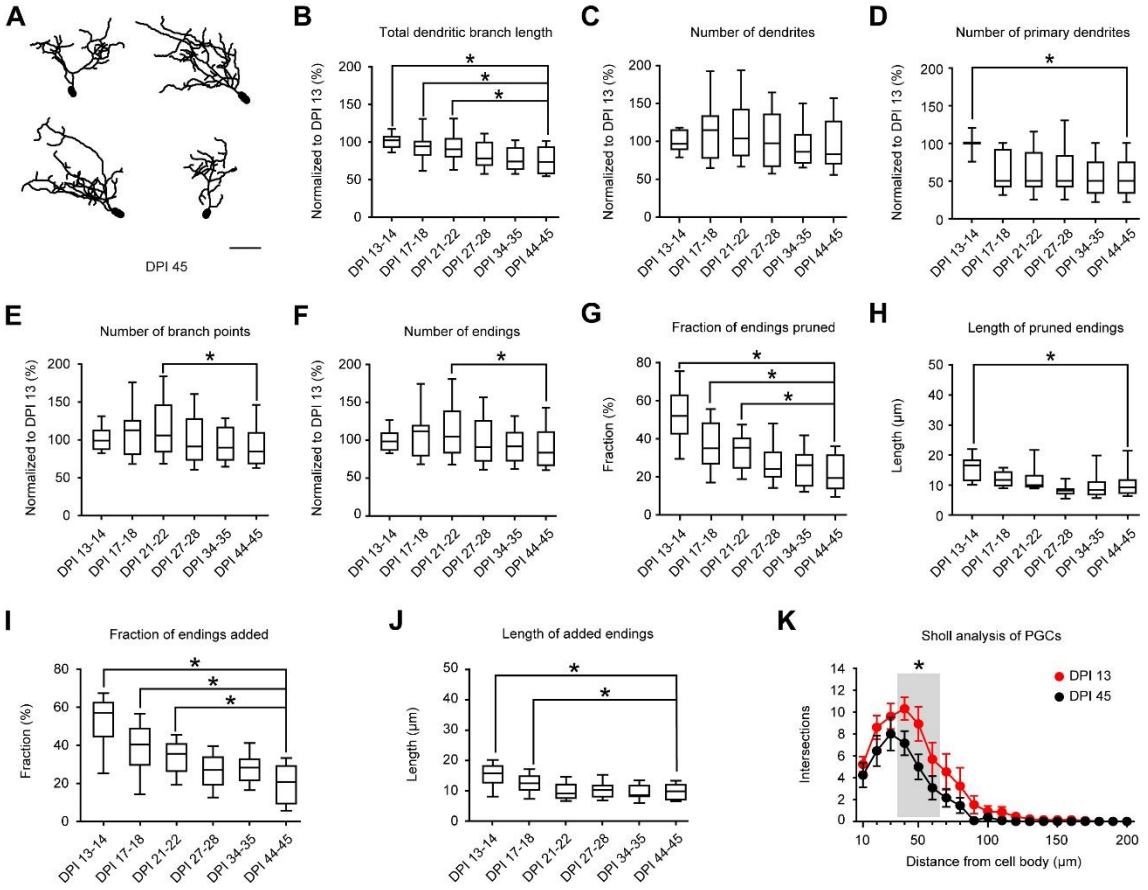

Figure 12. Development and plasticity of the dendritic tree in stable surviving adult-born PGCs. (**A**) Representative reconstructions of 4 adult-born PGCs at DPI 45. Scale bar: 25 µm. (**B**-**F**) Box plots summarizing the median (per cell) total dendritic branch length ($P < 0.05$, One-way repeated measures ANOVA followed by Holm-Sidak's multiple comparisons test) (**B**), numbers of dendrites ($P > 0.05$, One-way repeated measures ANOVA followed by Holm-Sidak's multiple comparisons test) (**C**), primary dendrites ($P < 0.05$, Friedman test followed by Dunn's multiple comparisons test) (**D**), branch points ($P < 0.05$, One-way repeated measures ANOVA followed by Holm-Sidak's multiple comparisons test) (**E**), and endings ($P < 0.05$, One-way repeated measures ANOVA followed by Holm-Sidak's multiple comparisons test) (**F**) in stable surviving adult-born PGCs. For each cell, the data were normalized to the respective values measured at DPI 13 (n = 13 PGCs, 7 mice). (**G**-**J**) 4D structural plasticity analysis showing the median (per cell) fraction of endings pruned ($P < 0.05$, One-way repeated measures ANOVA followed by Holm-Sidak's multiple comparisons test) (**G**), length of pruned endings ($P < 0.05$, Friedman test followed by Dunn's multiple comparisons test) (**H**), fraction of endings added ($P < 0.05$, One-way repeated measures ANOVA followed by Holm-Sidak's multiple comparisons test) (**I**), length of added endings ($P < 0.05$, One-way repeated measures ANOVA followed by Holm-Sidak's multiple comparisons test) (**J**) in stable surviving adult-born PGCs (n = 13 PGCs, 7 mice). (**K**) Sholl analyses of adult-born PGCs at DPI 13 (red) and DPI 45 (black) ($P < 0.05$, Wilcoxon signed rank test, n = 13 PGCs, 7 mice). Error bars represent SEM.

Table 3. Summary of dendritic development and remodeling data in stable surviving adult-born PGCs and *P* values in Figure 12.

Figure	Data (median ± IQR)	*P* values

Figure 12B	DPI 13-14: 96.32 ± 26.31% DPI 17-18: 114.1 ± 56.41% DPI 21-22: 103.3 ± 61.56% DPI 27-28: 96.91 ± 69.28% DPI 34-35: 85.57 ± 38.33% DPI 44-45: 82.35 ± 56.63%	DPI 13-14 VS. DPI 44-45: $P = 0.88$ DPI 17-18 VS. DPI 44-45: $P = 0.21$ DPI 21-22 VS. DPI 44-45: $P = 0.16$ DPI 27-28 VS. DPI 44-45: $P = 0.69$ DPI 34-35 VS. DPI 44-45: $P = 0.88$
Figure 12C	DPI 13-14: 100 ± 0% DPI 17-18: 50 ± 50% DPI 21-22: 50 ± 45.83% DPI 27-28: 50 ± 41.67% DPI 34-35: 50 ± 41.67% DPI 44-45: 50 ± 41.67%	DPI 13-14 VS. DPI 44-45: $P = 0.0018$ DPI 17-18 VS. DPI 44-45: $P > 0.99$ DPI 21-22 VS. DPI 44-45: $P > 0.99$ DPI 27-28 VS. DPI 44-45: $P > 0.99$ DPI 34-35 VS. DPI 44-45: $P > 0.99$
Figure 12D	DPI 13-14: 100.7 ± 14.34% DPI 17-18: 93.04 ± 18.8% DPI 21-22: 89.25 ± 24.56% DPI 27-28: 76.98 ± 31.09% DPI 34-35: 72.81 ± 29.28% DPI 44-45: 72.49 ± 35.53%	DPI 13-14 VS. DPI 44-45: $P < 0.0001$ DPI 17-18 VS. DPI 44-45: $P = 0.0009$ DPI 21-22 VS. DPI 44-45: $P = 0.0009$ DPI 27-28 VS. DPI 44-45: $P = 0.25$ DPI 34-35 VS. DPI 44-45: $P = 0.69$
Figure 12E	DPI 13-14: 97.73 ± 25.68% DPI 17-18: 111.4 ± 45.11% DPI 21-22: 104.6 ± 62.22% DPI 27-28: 90 ± 54.82% DPI 34-35: 88.64 ± 43.54% DPI 44-45: 83.33 ± 41.38%	DPI 13-14 VS. DPI 44-45: $P = 0.66$ DPI 17-18 VS. DPI 44-45: $P = 0.1$ DPI 21-22 VS. DPI 44-45: $P = 0.041$ DPI 27-28 VS. DPI 44-45: $P = 0.66$ DPI 34-35 VS. DPI 44-45: $P = 0.91$
Figure 12F	DPI 13-14: 98.78 ± 23.6% DPI 17-18: 112.5 ± 40.85% DPI 21-22: 105.1 ± 55.99% DPI 27-28: 91.3 ± 54.18% DPI 34-35: 92.39 ± 38.33% DPI 44-45: 84 ± 45.04%	DPI 13-14 VS. DPI 44-45: $P = 0.55$ DPI 17-18 VS. DPI 44-45: $P = 0.092$ DPI 21-22 VS. DPI 44-45: $P = 0.032$ DPI 27-28 VS. DPI 44-45: $P = 0.55$ DPI 34-35 VS. DPI 44-45: $P = 0.87$
Figure 12G	DPI 13-14: 52 ± 20.18% DPI 17-18: 35 ± 21.23% DPI 21-22: 35.29 ± 15.4% DPI 27-28: 24.14 ± 12.77% DPI 34-35: 26.09 ± 16.22% DPI 44-45: 19.44 ± 17.54%	DPI 13-14 VS. DPI 44-45: $P < 0.0001$ DPI 17-18 VS. DPI 44-45: $P = 0.0039$ DPI 21-22 VS. DPI 44-45: $P = 0.017$ DPI 27-28 VS. DPI 44-45: $P = 0.32$ DPI 34-35 VS. DPI 44-45: $P = 0.53$
Figure 12H	DPI 13-14: 16.6 ± 6.55 µm DPI 17-18: 11.72 ± 4.44 µm DPI 21-22: 9.97 ± 3.74 µm DPI 27-28: 8.19 ± 1.53 µm DPI 34-35: 8.37 ± 4.22 µm DPI 44-45: 9.28 ± 4.34 µm	DPI 13-14 VS. DPI 44-45: $P = 0.0002$ DPI 17-18 VS. DPI 44-45: $P = 0.23$ DPI 21-22 VS. DPI 44-45: $P = 0.83$ DPI 27-28 VS. DPI 44-45: $P = 0.97$ DPI 34-35 VS. DPI 44-45: $P > 0.99$
Figure 12I	DPI 13-14: 57.14 ± 17.78 % DPI 17-18: 40.43 ± 19.21 % DPI 21-22: 35.48 ± 14.29 % DPI 27-28: 27.03 ± 14.43 % DPI 34-35: 28.3 ± 11.12 % DPI 44-45: 20.69 ± 19.78 %	DPI 13-14 VS. DPI 44-45: $P < 0.001$ DPI 17-18 VS. DPI 44-45: $P < 0.001$ DPI 21-22 VS. DPI 44-45: $P = 0.0016$ DPI 27-28 VS. DPI 44-45: $P = 0.097$ DPI 34-35 VS. DPI 44-45: $P = 0.069$
Figure 12J	DPI 13-14: 15.78 ± 5.55 µm DPI 17-18: 12.51 ± 4.55 µm DPI 21-22: 9.04 ± 4.45 µm DPI 27-28: 10.23 ± 3.73 µm DPI 34-35: 8.47 ± 3.56 µm DPI 44-45: 9.82 ± 4.82 µm	DPI 13-14 VS. DPI 44-45: $P < 0.001$ DPI 17-18 VS. DPI 44-45: $P = 0.033$ DPI 21-22 VS. DPI 44-45: $P = 0.96$ DPI 27-28 VS. DPI 44-45: $P = 0.91$ DPI 34-35 VS. DPI 44-45: $P = 0.96$

Figure 12K	Mean ± SEM 10 µm: 5.23 ± 0.71 (DPI 13), 4.12 ± 1.13 (DPI 45) 20 µm: 8.62 ± 1.08 (DPI 13), 6.46 ± 1.39 (DPI 45) 30 µm: 9.62 ± 1.17 (DPI 13), 8 ± 1.5 (DPI 45) 40 µm: 10.31 ± 1.04 (DPI 13), 7.15 ± 1.11 (DPI 45) 50 µm: 8.92 ± 1.58 (DPI 13), 5 ± 1.15 (DPI 45) 60 µm: 5.69 ± 1.52 (DPI 13), 3.08 ± 1.08 (DPI 45) 70 µm: 5.54 ± 1.65 (DPI 13), 2.15 ± 0.83 (DPI 45) 80 µm: 3.23 ± 1.69 (DPI 13), 1.46 ± 0.69 (DPI 45) 90 µm: 1.54 ± 0.81 (DPI 13), 0.077 ± 0.08 (DPI 45) 100 µm: 0.92 ± 0.5 (DPI 13), 0.38 ± 0.24 (DPI 45)	DPI 13 VS. DPI 45 10 µm: *P* = 0.48 20 µm: *P* = 0.24 30 µm: *P* = 0.12 40 µm: *P* = 0.041 50 µm: *P* = 0.015 60 µm: *P* = 0.043 70 µm: *P* = 0.1 80 µm: *P* = 0.25 90 µm: *P* = 0.25 100 µm: *P* = 0.25

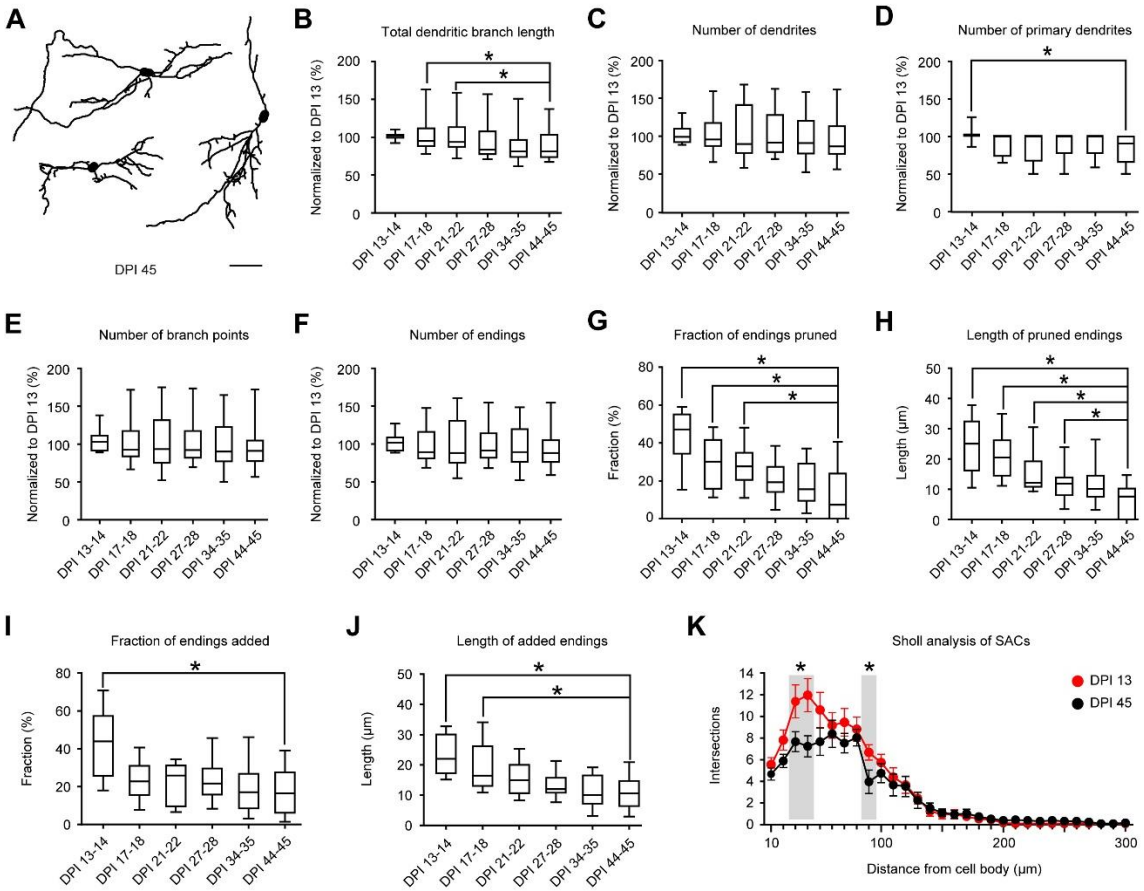

Figure 13. Development and plasticity of the dendritic tree in stable surviving adult-born SACs. (**A**) Representative reconstructions of three adult-born SACs at DPI 45. Scale bar: 50 µm. (**B**-**F**) Box plots illustrating the median (per cell) total dendritic branch length ($P < 0.05$, One-way repeated measures followed by Holm-Sidak's multiple comparisons test) (**B**), the

median (per cell) numbers of dendrites ($P > 0.05$, Friedman test followed by Dunn's multiple comparisons test) (**C**), primary dendrites ($P < 0.05$, Friedman test followed by Dunn's multiple comparisons test) (**D**), branch points ($P > 0.05$, Friedman test followed by Dunn's multiple comparisons test) (**E**) and dendritic endings ($P > 0.05$, One-way repeated measures ANOVA followed by Holm-Sidak's multiple comparisons test) (**F**) in stable surviving adult-born short axon cells. For each cell, the data were normalized to the respective values measured at DPI 13 (n = 14 SACs, 5 mice). (**G**-**J**) 4D structural plasticity analysis showing the median (per cell) fraction of endings pruned ($P < 0.05$, Friedman test followed by Dunn's multiple comparisons test) (**G**), length of pruned endings ($P < 0.05$, Friedman test followed by Dunn's multiple comparisons test) (**H**), fraction of endings added ($P < 0.05$, Friedman test followed by Dunn's multiple comparisons test) (**I**), length of added endings ($P < 0.05$, One-way repeated measures ANOVA followed by Holm-Sidak's multiple comparisons test) (**J**) (n = 14 SACs, 5 mice). (**K**) Sholl analyses of SACs at DPI 13 (red) and DPI 45 (black) ($P < 0.05$, Wilcoxon signed rank test, n = 14 SACs, 5 mice). Error bars represent SEM.

Table 4. Summary of dendritic development and remodeling data in stable surviving adult-born SACs and *P* values in Figure 13.

Figure	Data (median ± IQR)	*P* values
Figure 13B	DPI 13-14: 99.95 ± 18.62% DPI 17-18: 96.7 ± 31.26 % DPI 21-22: 90.61 ± 64.68% DPI 27-28: 92.58 ± 49.93% DPI 34-35: 91.95 ± 44.4% DPI 44-45: 87.55 ± 37.68%	DPI 13-14 VS. DPI 44-45: $P > 0.99$ DPI 17-18 VS. DPI 44-45: $P > 0.99$ DPI 21-22 VS. DPI 44-45: $P > 0.99$ DPI 27-28 VS. DPI 44-45: $P > 0.99$ DPI 34-35 VS. DPI 44-45: $P > 0.99$
Figure 13C	DPI 13-14: 100 ± 2.5% DPI 17-18: 100 ± 27.08% DPI 21-22: 100 ± 33.33% DPI 27-28: 100 ± 23.33% DPI 34-35: 100 ± 23.33% DPI 44-45: 100 ± 35%	DPI 13-14 VS. DPI 44-45: $P = 0.012$ DPI 17-18 VS. DPI 44-45: $P > 0.99$ DPI 21-22 VS. DPI 44-45: $P > 0.99$ DPI 27-28 VS. DPI 44-45: $P > 0.99$ DPI 34-35 VS. DPI 44-45: $P > 0.99$
Figure 13D	DPI 13-14: 102.7 ± 5.03% DPI 17-18: 96.07 ± 24.61% DPI 21-22: 94.62 ± 27.31% DPI 27-28: 84.71± 31.26% DPI 34-35: 82.04 ± 23.7% DPI 44-45: 81.87 ± 30.77%	DPI 13-14 VS. DPI 44-45: $P = 0.24$ DPI 17-18 VS. DPI 44-45: $P = 0.037$ DPI 21-22 VS. DPI 44-45: $P = 0.042$ DPI 27-28 VS. DPI 44-45: $P = 0.24$ DPI 34-35 VS. DPI 44-45: $P = 0.58$
Figure 13E	DPI 13-14: 101.9 ± 20.78% DPI 17-18: 91.15 ± 34.74% DPI 21-22: 92.31± 57.03% DPI 27-28: 91 ± 36.51% DPI 34-35: 88.87± 46.19% DPI 44-45: 90 ± 27.98%	DPI 13-14 VS. DPI 44-45: $P = 0.86$ DPI 17-18 VS. DPI 44-45: $P > 0.99$ DPI 21-22 VS. DPI 44-45: $P > 0.99$ DPI 27-28 VS. DPI 44-45: $P > 0.99$ DPI 34-35 VS. DPI 44-45: $P > 0.99$
Figure 13F	DPI 13-14: 101.2 ± 18.53% DPI 17-18: 88.91 ± 35.96% DPI 21-22: 87.69 ± 56.45% DPI 27-28: 91 ± 33.5% DPI 34-35: 89.13 ± 44.3% DPI 44-45: 87.68 ± 29.86%	DPI 13-14 VS. DPI 44-45: $P = 0.52$ DPI 17-18 VS. DPI 44-45: $P = 0.69$ DPI 21-22 VS. DPI 44-45: $P = 0.66$ DPI 27-28 VS. DPI 44-45: $P = 0.65$ DPI 34-35 VS. DPI 44-45: $P = 0.78$
Figure 13G	DPI 13-14: 47.12 ± 20.82% DPI 17-18: 30.11 ± 25.72% DPI 21-22: 27.62 ± 14.29% DPI 27-28: 19.29 ± 13.31% DPI 34-35: 15.61 ± 19.57% DPI 44-45: 7.32 ± 23.9%	DPI 13-14 VS. DPI 44-45: $P < 0.0001$ DPI 17-18 VS. DPI 44-45: $P = 0.032$ DPI 21-22 VS. DPI 44-45: $P = 0.0051$ DPI 27-28 VS. DPI 44-45: $P = 0.79$ DPI 34-35 VS. DPI 44-45: $P > 0.99$

Figure 13H	DPI 13-14: 25.03 ± 16.21 µm DPI 17-18: 20.54 ± 11.67 µm DPI 21-22: 12.12 ± 8.42 µm DPI 27-28: 11.88 ± 5.87 µm DPI 34-35: 10.11 ± 6.99 µm DPI 44-45: 7.59 ± 10.25 µm	DPI 13-14 VS. DPI 44-45: $P < 0.0001$ DPI 17-18 VS. DPI 44-45: $P = 0.0001$ DPI 21-22 VS. DPI 44-45: $P = 0.0014$ DPI 27-28 VS. DPI 44-45: $P = 0.017$ DPI 34-35 VS. DPI 44-45: $P = 0.22$
Figure 13I	DPI 13-14: 43.93 ± 31.62% DPI 17-18: 22.84 ± 15.37% DPI 21-22: 25.92 ± 21.51% DPI 27-28: 21.68 ± 13.77% DPI 34-35: 17.09 ± 18.28% DPI 44-45: 16.48 ± 21.47%	DPI 13-14 VS. DPI 44-45: $P = 0.0003$ DPI 17-18 VS. DPI 44-45: $P > 0.99$ DPI 21-22 VS. DPI 44-45: $P = 0.86$ DPI 27-28 VS. DPI 44-45: $P = 0.65$ DPI 34-35 VS. DPI 44-45: $P > 0.99$
Figure 13J	DPI 13-14: 22.04 ± 12.81 µm DPI 17-18: 16.41 ± 13.13 µm DPI 21-22: 14.97 ± 9.38 µm DPI 27-28: 12.04 ± 4.98 µm DPI 34-35: 10.12 ± 9.33 µm DPI 44-45: 10.62 ± 8.31 µm	DPI 13-14 VS. DPI 44-45: $P < 0.0001$ DPI 17-18 VS. DPI 44-45: $P = 0.0003$ DPI 21-22 VS. DPI 44-45: $P = 0.071$ DPI 27-28 VS. DPI 44-45: $P = 0.53$ DPI 34-35 VS. DPI 44-45: $P = 0.94$
Figure 13K	Mean ± SEM 10 µm: 5.43 ± 0.75 (DPI 13), 4.64 ± 0.57 (DPI 45) 20 µm: 7.79 ± 0.93 (DPI 13), 5.86 ± 0.61 (DPI 45) 30 µm: 11.36 ± 1.53 (DPI 13), 7.64 ± 0.92 (DPI 45) 40 µm: 11.93 ± 1.54 (DPI 13), 7.21 ± 0.99 (DPI 45) 50 µm: 10.57 ± 1.61 (DPI 13), 7.64 ± 1.26 (DPI 45) 60 µm: 9.14 ± 1.19 (DPI 13), 8.36 ± 1.27 (DPI 45) 70 µm: 9.43 ± 1.28 (DPI 13), 7.5 ± 0.91 (DPI 45) 80 µm: 8.79 ± 1.12 (DPI 13), 8 ± 0.78 (DPI 45) 90 µm: 6.64 ± 0.72 (DPI 13), 3.93 ± 1.1 (DPI 45) 100 µm: 5.71 ± 0.75 (DPI 13), 4.71 ± 0.88 (DPI 45)	DPI 13 VS. DPI 45 10 µm: $P = 0.34$ 20 µm: $P = 0.06$ 30 µm: $P = 0.029$ 40 µm: $P = 0.0039$ 50 µm: $P = 0.08$ 60 µm: $P = 0.56$ 70 µm: $P = 0.1$ 80 µm: $P = 0.59$ 90 µm: $P = 0.0084$ 100 µm: $P = 0.26$

In a subset of experiments, we additionally followed the dendritic morphology of adult-born JGNs from DPI 9 to DPI 13. The dendritic morphology of stable surviving adult-born JGNs (i.e. cells, which did not change their position between DPI 13 and DPI 45) at DPI 9-13 was reconstructed and analyzed no matter whether the cells migrated or not during these 5 imaging sessions. All the data were normalized to the respective values measured at DPI 13. Our data revealed that the dendritic tree of stable surviving adult-born JGNs grew rapidly, increasing, for example, the TDBL by 35.21% and the number of

dendrites by 68.42% between DPI 9 and DPI 13 (Figure 14, n = 15 cells from 4 mice).

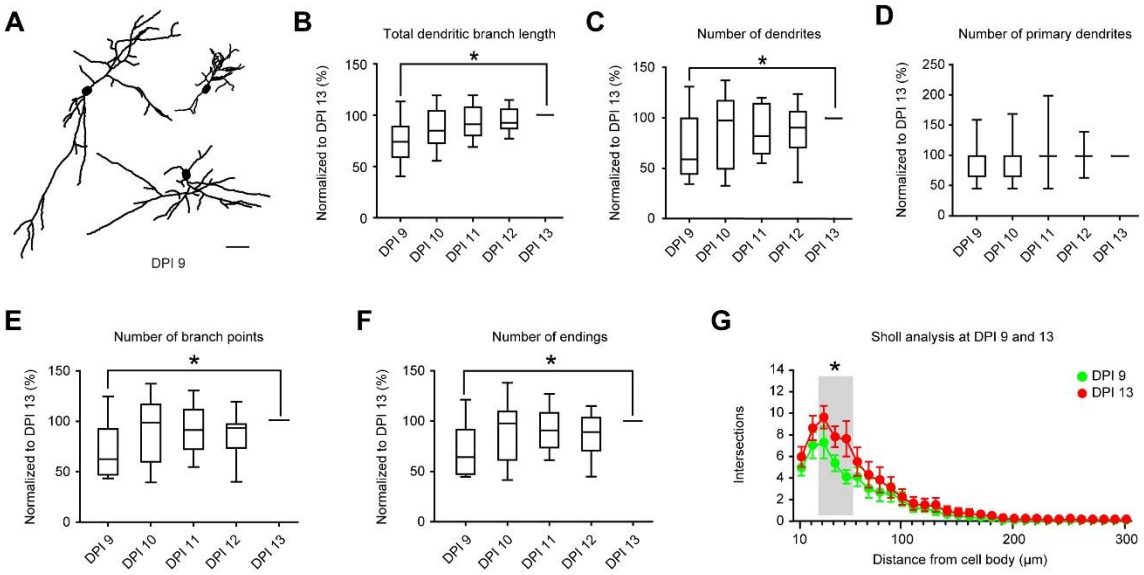

Figure 14. An initial period of fast dendritic growth in surviving adult-born JGNs at DPI 9-13. (**A**) Representative reconstructions of 3 adult-born JGNs at DPI 9. Scale bar: 25 µm. (**B**-**F**) Box plots summarizing the median (per cell) total dendritic branch length (**B**), numbers of dendrites (**C**), primary dendrites (**D**), branch points (**E**) and endings (**F**) in surviving adult-born JGNs at DPI 9-13. For each cell, the data were normalized to the respective values measured at DPI 13 ($P < 0.05$, Friedman test followed by Dunn's multiple comparisons test, n = 15 JGNs, 4 mice). (**G**) Sholl analyses showing the number of dendritic intersections with Sholl spheres at DPI 9 (green) and DPI 13 (red) ($P < 0.05$, Wilcoxon signed rank test, n = 15 JGNs, 4 mice). Error bars represent SEM.

Table 5. Summary of dendritic development in stable surviving adult-born JGNs at DPI 9-13 and *P* values in Figure 14.

Figure	Data (median ± IQR)	*P* values
Figure 14B	DPI 9: 59.38 ± 55.17% DPI 10: 97.67 ± 67.4% DPI 11: 82.35 ± 49.48% DPI 12: 90.63 ± 35.29% DPI 13: 100 ± 0%	DPI 9 VS. DPI 13: $P = 0.032$ DPI 10 VS. DPI 13: $P > 0.99$ DPI 11 VS. DPI 13: $P > 0.99$ DPI 12 VS. DPI 13: $P > 0.99$
Figure 14C	DPI 9: 100 ± 33.33% DPI 10: 100 ± 33.33% DPI 11: 100 ± 0% DPI 12: 100 ± 0% DPI 13: 100 ± 0%	DPI 9 VS. DPI 13: $P > 0.99$ DPI 10 VS. DPI 13: $P > 0.99$ DPI 11 VS. DPI 13: $P > 0.99$ DPI 12 VS. DPI 13: $P > 0.99$
Figure 14D	DPI 9: 73.96 ± 29.85% DPI 10: 84.66 ± 31.32% DPI 11: 90.96 ± 27.45% DPI 12: 92.27 ± 18.7% DPI 13: 100 ± 0%	DPI 9 VS. DPI 13: $P = 0.0014$ DPI 10 VS. DPI 13: $P = 0.2$ DPI 11 VS. DPI 13: $P = 0.66$ DPI 12 VS. DPI 13: $P > 0.99$

Figure 14E	DPI 9: 61.54 ± 45.15% DPI 10: 97.83 ± 56.87% DPI 11: 90.48 ± 39.07% DPI 12: 92.31 ± 23.57% DPI 13: 100 ± 0%	DPI 9 VS. DPI 13: *P* = 0.006 DPI 10 VS. DPI 13: *P* = 0.99 DPI 11 VS. DPI 13: *P* > 0.99 DPI 12 VS. DPI 13: *P* > 0.99
Figure 14F	DPI 9: 64.29 ± 44.3% DPI 10: 97.87 ± 48.1% DPI 11: 90.91 ± 34.62% DPI 12: 89.19 ± 32.77% DPI 13: 100 ± 0%	DPI 9 VS. DPI 13: *P* = 0.0089 DPI 10 VS. DPI 13: *P* = 0.99 DPI 11 VS. DPI 13: *P* > 0.99 DPI 12 VS. DPI 13: *P* > 0.99
Figure 14G	Mean ± SEM 10 µm: 4.87 ± 0.76 (DPI 9), 5.87 ± 0.93 (DPI 13) 20 µm: 6.93 ± 1.2 (DPI 9), 8.53 ± 1.14 (DPI 13) 30 µm: 7.2 ± 1.49 (DPI 9), 9.53 ± 1.05 (DPI 13) 40 µm: 5.27 ± 0.76 (DPI 9), 7.73 ± 0.98 (DPI 13) 50 µm: 4 ± 0.64 (DPI 9), 7.53 ± 1.65 (DPI 13) 60 µm: 4 ± 0.88 (DPI 9), 5.40 ± 1.33 (DPI 13) 70 µm: 2.93 ± 0.88 (DPI 9), 4.2 ± 1.2 (DPI 13) 80 µm: 2.6 ± 0.87 (DPI 9), 3.73 ± 1.19 (DPI 13) 90 µm: 2.53 ± 0.86 (DPI 9), 3 ± 0.98 (DPI 13) 100 µm: 1.93 ± 0.65 (DPI 9), 2.13 ± 0.73 (DPI 13)	DPI 9 VS. DPI 13 10 µm: *P* = 0.33 20 µm: *P* = 0.087 30 µm: *P* = 0.04 40 µm: *P* = 0.026 50 µm: *P* = 0.0083 60 µm: *P* = 0.13 70 µm: *P* = 0.098 80 µm: *P* = 0.086 90 µm: *P* = 0.78 100 µm: *P* = 0.63

Taken together, our data revealed that in stable surviving adult-born JGNs, dendritic growth was present only within a very short time window (DPI 9-13) during the early pre-integration phase. The rest of the maturation time (DPI 13-45) was accompanied by a significant reduction in the size and complexity of the dendritic tree after completion of lateral migration. At early developmental stages, adult-born JGNs underwent both extensive dendritic pruning and addition and the degree of dendritic remodeling decreased during development. Interestingly, we found adult-born PGCs and adult-born SACs shared similar dendritic developmental patterns.

3.3 Eliminated and surviving adult-born JGNs had a similar level of dendritic complexity and plasticity

Elimination of immature neurons by apoptosis takes place both during development and also in adulthood (Kuhn, 2015; Yuan and Yankner, 2000). This is a fast process, as the time from initiation of apoptosis to the completion

of apoptosis usually takes less than 24 hours (Cellerino et al., 2000; Cordeiro et al., 2004; Elmore, 2007; Saraste, 1999). Therefore, to determine whether the morphological features can distinguish to be eliminated and surviving cells, we took the day of cell death as a reference point and analyzed the dendritic morphology of eliminated and surviving adult-born JGNs at one, two and three days before death (DBD 1: 0-24 hours before death, DBD 2: 24-48 hours before death, DBD 3: 48-72 hours before death). The data obtained were normalized to the respective median values of all (at least 4) surviving cells of the same cell subtype (i.e. either PGCs-like or SACs-like) recorded in the same mouse at the same time point, as illustrated in Figure 15A. As reported in Figure 10, some multipolar adult-born JGNs (look like SACs) at early developmental stages pruned their primary dendrites during the maturation process to have unipolar dendritic morphology (typical PGCs) at the mature stages, thus we termed adult-born JGNs at these stages as PGCs-like and SACs-like cells. We found no significant difference between eliminated and surviving adult-born JGNs for all morphological parameters analyzed, including TDBL (Figure 15B), number of dendrites (Figure 15C), tnumber of primary dendrites (Figure 15D), the number of branch points (Figure 15E), number of dendritic endings (Figure 15F) (P > 0.05 for all comparisons, Wilcoxon signed rank test; n = 10 eliminated and 63 surviving cells from 6 mice). These data demonstrated that eliminated adult-born JGNs had a comparable dendritic complexity with surviving counterparts.

To understand whether the degree of dendritic remodeling can predict the future survival/death of adult-born JGNs, we analyze the addition and pruning of dendritic endings between two neighboring time points using the 4DSPA approach, as mentioned above. The fraction of pruned endings (Figure 15G), length of pruned endings (Figure 15H), fraction of added endings (Figure 15I) and length of newly-added endings (Figure 15J) in eliminated adult-born JGNs were similar with those in surviving adult-born JGNs (P > 0.05 for all comparisons, Wilcoxon signed rank test; n = 10 eliminated and 63 surviving cells from 6 mice). These data indicated that the degree of dendritic remodeling can not differentiate the subsequently eliminated adult-born JGNs from the surviving adult-born JGNs.

Together, these data suggested that the complexity and remodeling dynamics of the dendritic tree can not predict the subsequent elimination of adult-born JGNs in the mouse OB.

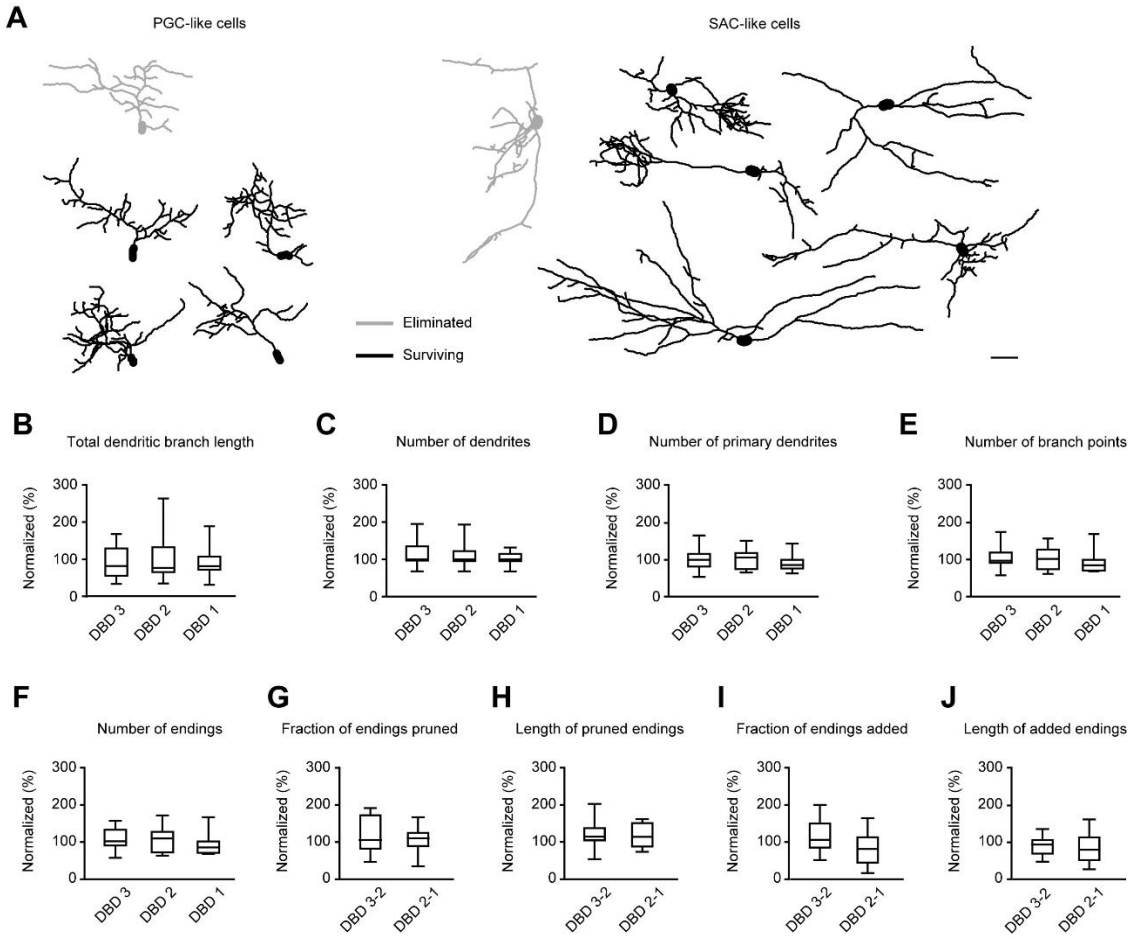

Figure 15. Dendritic morphology can not predict the fate of adult-born JGNs. (**A**) Representative reconstructions of two eliminated (grey) adult-born JGNs and corresponding surviving (black) cells from the same mice two days before death (DBD 2). Left: PGC-like cells, right: SAC-like cells. Scale bar: 25 µm. (**B**-**F**) Median (per cell) normalized total dendritic branch length (**B**), numbers of dendrites (**C**), primary dendrites (**D**), branch points (**E**) and endings (**F**) measured at DBD 3, DBD 2 and DBD 1. Data were normalized to the median value of all surviving cells of the same type recorded in the same animal at the same time points. (**G**-**J**) Median (per cell) fraction of endings pruned (**G**), length of pruned endings (**H**), fraction of endings added (**I**), length of added endings (**J**) analyzed at DBD 3-2 and DBD 2-1. Data were normalized to the respective median of corresponding surviving cells of the same type recorded in the same animal at the same time points ($P > 0.05$, Wilcoxon signed rank test, n = 10 eliminated cells and 63 surviving cells, 6 mice).

Table 6. Summary of dendritic complexity and remodeling in eliminated and surviving adult-born JGNs at DBD 3, DBD 2, DBD 1 and *P* values in Figure 15.

Figure	Data (median ± IQR)	*P* values
Figure 15B	DBD 3: 100 ± 39.67% DBD 2: 100 ± 28.26%	DBD 3: $P = 0.25$ DBD 2: $P = 0.63$

	DBD 1: 100 ± 20.79%	DBD 1: *P* > 0.99
Figure 15C	DBD 3: 100.4 ± 35.9% DBD 2: 106.7 ± 45.12% DBD 1: 86.03 ± 25.13%	DBD 3: *P* > 0.99 DBD 2: *P* = 0.73 DBD 1: *P* = 0.16
Figure 15D	DBD 3: 83.75 ± 77.61% DBD 2: 78.59 ± 70.6% DBD 1: 83.51 ± 37.99%	DBD 3: *P* = 0.63 DBD 2: *P* = 0.70 DBD 1: *P* = 0.56
Figure 15E	DBD 3: 118.1 ± 82.18% DBD 2: 125.9 ± 55.2% DBD 1: 98.69 ± 90.31%	DBD 3: *P* = 0.85 DBD 2: *P* = 0.85 DBD 1: *P* = 0.13
Figure 15F	DBD 3: 100.8 ± 45.12% DBD 2: 108.1 ± 57.72% DBD 1: 84.17 ± 33.21%	DBD 3: *P* = 0.57 DBD 2: *P* = 0.70 DBD 1: *P* = 0.22
Figure 15G	DBD 3-2: 105.2 ± 97.07% DBD 2-1: 102.2 ± 56.84%	DBD 3-2: *P* = 0.43 DBD 2-1: *P* = 0.63
Figure 15H	DBD 3-2: 87.81 ± 33.08% DBD 2-1: 87.23 ± 56.73%	DBD 3-2: *P* = 0.28 DBD 2-1: *P* = 0.38
Figure 15I	DBD 3-2: 108.3 ± 73.74% DBD 2-1: 83.61 ± 76.24%	DBD 3-2: *P* = 0.43 DBD 2-1: *P* = 0.32
Figure 15J	DBD 3-2: 95.89 ± 44.76% DBD 2-1: 82.06 ± 69.69%	DBD 3-2: *P*= 0.56 DBD 2-1: *P* = 0.38

3.4 *In* vivo tracking adult-born JGNs with ratiometric calcium indicator Twitch-2B

Since the period of adult-born JGN elimination corresponds to the pre-integration phase, when adult-born JGNs start to receive synaptic inputs and integrate into the local circuitry, it has been postulated that adult-born JGNs die because they “fail to integrate” into the pre-existing neural circuitry (Lepousez and Lledo, 2011; Lin et al., 2010; Turnley et al., 2014). We took the ability to acquire odor-responsiveness as the readout of adult-born JGN’s functional integration into the pre-existing neural circuitry and tested whether odor-responsiveness protects adult-born JGNs from being eliminated. To this end, migrating neuroblasts in the RMS were labeled by injection of lentivirus encoding Ca^{2+} indicator Twitch-2B (Figure 16A). Twitch-2B is a förster resonance energy transfer (FRET) based ratiometric Ca^{2+} indicator, composed of a donor protein (mCerulean3), a Ca^{2+}-binding domain and an acceptor protein ($cpVenus^{CD}$), thus the changes in the ratio of fluorescence intensity between the donor and acceptor proteins reflect the change in free intracellular Ca^{2+} concentration ($[Ca^{2+}]_i$, (Thestrup et al., 2014)), see Materials and Methods section for more details. Because of its ratiometric nature, Twitch-2B is

particularly valuable for longitudinal imaging of individual cells in awake animals (Maslyukov et al., 2018; Thestrup et al., 2014). Since it is difficult to track the identity of migrating adult-born JGNs without unique tags in the glomerular layer, our longitudinal imaging started at DPI 18, when the majority of adult-born JGNs have completed lateral migration, see Figure 7A in (Liang et al., 2016). Twitch-2B$^+$ adult-born JGNs were imaged every 2nd day from DPI 18 to DPI 44 in awake mice (Figure 16B). Because lentiviruses transduce both dividing and non-dividing cells, late-coming adult-born JGNs, eventually belonging to another wave of migration and having heterogeneous ages, arrived in the OB at a low rate after lentiviral injection in the RMS (Figure 16C) (Mizrahi, 2007; Wallace et al., 2017). We, therefore, focused on cells present in the FOV at DPI 18 to avoid late-coming adult-born JGNs of undefined age (yellow arrow in Figure 16C) and defined cells, which did not migrate during the first three imaging sessions (DPI 18, DPI 20, DPI 22), as stable adult-born JGNs (Figure 16C). Out of 533 Twitch-2B$^+$ adult-born JGNs tested, 94.12 ± 7.10% (median per mouse) were stable cells (Figure 16D, n = 11 mice).

Similar to the procedure described for RGB-labeled cells in Figure 8B, the criteria to decide the elimination of Twitch-2B$^+$ adult-born JGNs were as following: either (i) the cell debris was identified in the position where occupied by an adult-born JGN or (ii) stable adult-born JGNs disappeared from the cranial window after DPI 22 (Figure 16E,F). The median (per mouse) fraction of Twitch-2B$^+$ adult-born JGNs eliminated from DPI 22 to DPI 44 was 6.25 ± 5.24% (n = 11 mice), which is similar to the fraction (5.10 ± 9.87%, n = 12 mice) of eliminated RGB$^+$ adult-born JGNs during the same time period (Figure 16G, P = 0.97, Mann-Whitney test).

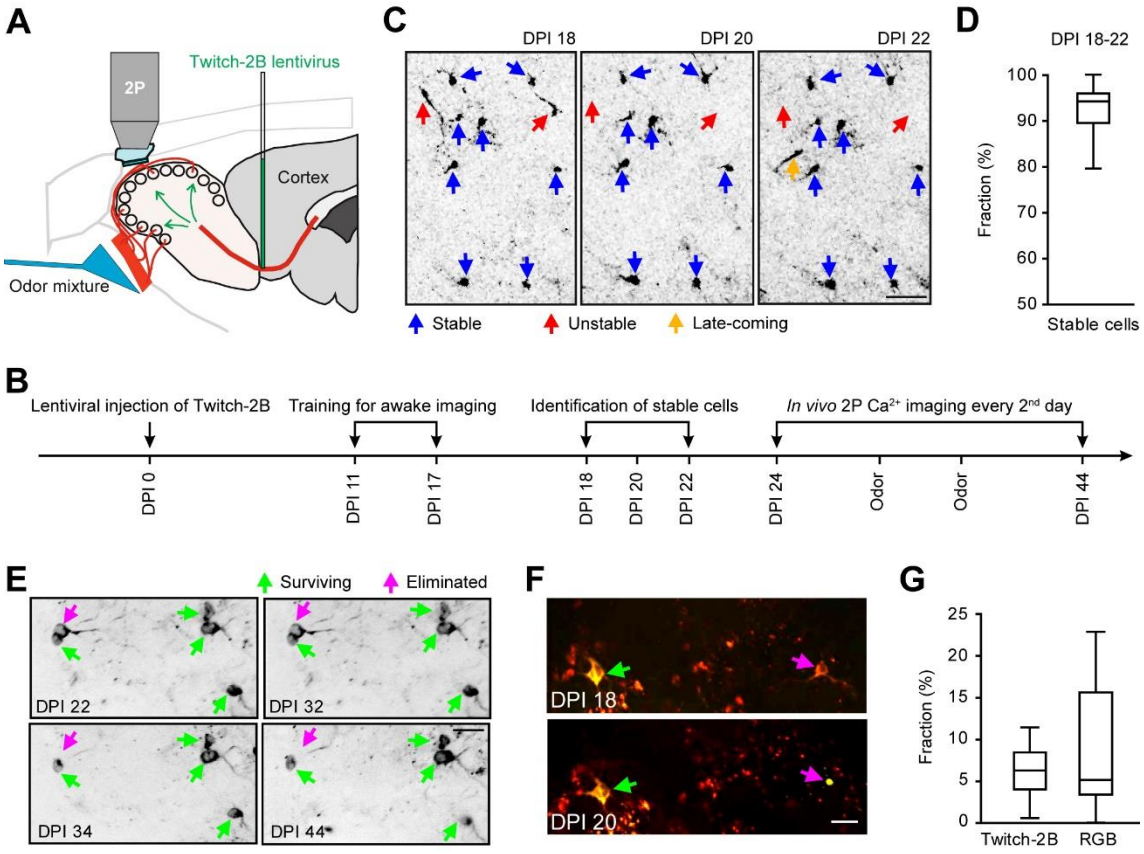

Figure 16. *In vivo* tracking adult-born JGNs with calcium indicator Twitch-2B(**A**) Scheme of the experimental setup. Lentivirus encoding Twitch-2B were injected into the RMS and Twitch-2B$^+$ adult-born JGNs were imaged *in vivo*. Odorant can be applied in front of the mouse's snout. (**B**) The experimental timeline was as follows: at DPI 11-17, mice were trained every day for awake imaging, at DPI 18, DPI 20 and DPI 22, the stable population of adult-born JGNs was defined, and at DPI 24-44, stable adult-born JGNs were recorded every 2nd day. (**C**) MIP (63-135 µm, step 3 µm) images illustrating 8 stable (blue arrows), 2 unstable (red arrows) and 1 late-coming (orange arrow) Twitch-2B$^+$ adult-born JGNs at DPI 18-22. Scale bars: 50 µm. (**D**) A box plot showing the fraction of stable adult-born JGNs at DPI 18-22 (n = 11 mice). (**E**) Images showing 1 eliminated (magenta arrow) and the other 4 surviving cells (green arrows) in the same FOV at 4 different time points. Each image was an average of 830 consecutive frames. In this specific case, DPI 34 was defined as the day of death. Scale bar: 20 µm. (**F**) Images of 1 eliminated (magenta arrow) and 1 surviving (green arrow) cells in the same FOV at 2 consecutive time points. Each image was an average of 830 consecutive frames. Left: DPI 18, DBD 2 (0-48 hours before cell debris was caught). Right: DPI 20, the day of death. Scale bar: 20 µm. (**C**) Box plots showing the fractions of cells eliminated after DPI 22 in the Twitch-2B and RGB experimental groups (P = 0.97, Mann-Whitney test, n = 11 mice for Twitch-2B group, n = 12 mice for RGB group).

Odor-responsiveness of stable Twitch-2B$^+$ adult-born JGNs was examined by applying twice the mixture of either 3 or 7 odorants (see Materials and Methods section for details) in front of the snout of anesthetized mice. Both odor mixtures can cause broad activation of dorsal glomeruli in the OB (Kovalchuk et al., 2015; Livneh et al., 2014), thereby increasing the probability to recruit odor responding

adult-born JGNs. Under these experimental conditions, 58.00 ± 17.44% (median per mouse, 281 cells, n = 11 mice) of adult-born JGNs showed odor-evoked responses (Figure 17A-C). Out of 25 eliminated cells, the odor-evoked responsiveness of 19 cells happened to be tested before they were eliminated. Out of these eliminated cells, 63.16% (12/19 cells from 8 mice) showed odor-evoked Ca^{2+} signals prior to their death (Figure 17D). This data convincingly demonstrated that adult-born JGNs can be eliminated despite acquired odor-responsiveness. The mentioned above fraction of odor-responding among eliminated adult-born JGNs (63.16%, 12/19 cells from 8 mice) was not significantly different from the fraction (56.37%, 146/259 cells from 11 mice) of odor-responding cells among surviving adult-born JGNs (Figure 17D, $P = 0.74$, Chi-square test with Yates' correction), suggesting acquired odor-responsiveness cannot protect adult-born JGNs from being eliminated.

To investigate whether eliminated and surviving adult-born JGNs responded differently to odor stimulation, we analyzed the maximum ΔR/R amplitude and the area under the curve (AUC) of odor-evoked Ca^{2+} transients in eliminated and surviving adult-born JGNs. Then, the median values of eliminated cells were normalized to the median values of corresponding surviving cells recorded from the same mice at the same time points. Interestingly, there was no significant difference between to be eliminated and surviving cells in terms of the maximum ΔR/R amplitude (Figure 17E, $P = 0.49$, Wilcoxon signed rank test) and the AUC (Fig. 4F, $P = 0.23$, One sample *t* test) (n = 12 odor responding eliminated cells and 112 odor responding surviving cells from 8 mice). These data demonstrated that there are no correlations between odor-evoked responses and the fate of adult-born JGNs.

In conclusion, our data showed that acquired odor-responsiveness cannot protect adult-born JGNs from being eliminated and there are no correlations between odor-evoked responses and the fate of adult-born JGNs.

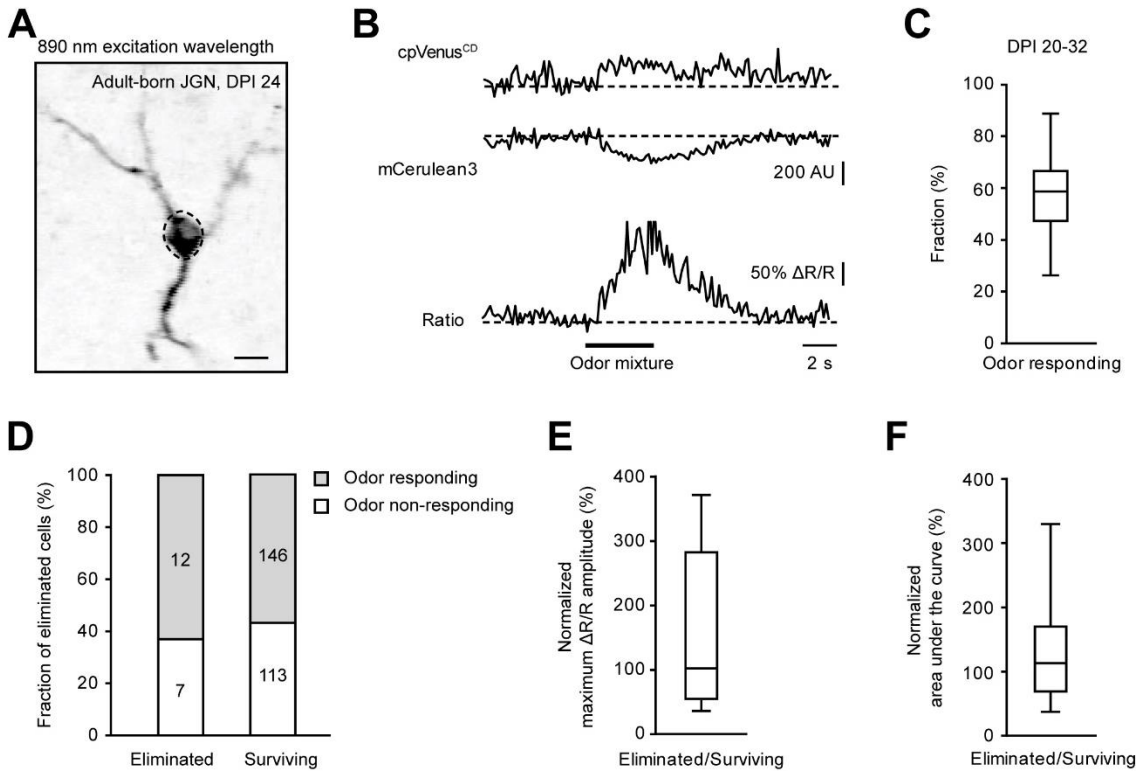

Figure 17. The fate of adult-born JGNs is not determined by their odor-responsiveness. (**A**) Representative image (average of 140 consecutive frames) of a Twitch-2B$^+$ adult-born JGN at DPI 24. Scale bar: 10 µm. (**B**) Traces illustrating changes in fluorescence intensity of mCerulean3 and cpVenus^{CD} channels and the Twitch-2B ratio trace recorded from the somatic region of interest shown in (**A**) in response to a 4-s-long application of the mixture of 7 odorants (ethyl-acetate, butanal, pentanal, ethyltiglate, propanal, methyl-propionate and ethyl-butyrate) (**C**) Box plot summarizing the median (per mouse) fraction of odor responding cells at DPI 20-32 (n = 11 mice). (**D**) Bar graphs showing the fractions of odor responding and odor non-responding cells among the eliminated and surviving cells (n = 19 eliminated cells from 8 mice and 259 surviving cells from 11 mice). (**E**, **F**) Box plots showing the normalized maximum ΔR/R amplitude (**E**) (*P* = 0.49, Wilcoxon signed rank test) and AUC (**F**) (*P* = 0.23, One sample *t* test). The medians of eliminated cells were normalized to the medians of corresponding surviving cells recorded from the same mice at the same time points (n = 12 odor responding eliminated cells and 112 odor responding surviving cells, 8 mice).

3.5 Distinct basal Ca^{2+} levels and endogenous activity patterns in eliminated and surviving adult-born JGNs

In our previous study, the ubiquitous presence of spontaneous Ca^{2+} transients has been detected in the Twitch-2B$^+$ adult-born JGNs during DPI 8-12 (Maslyukov et al., 2018). Using tetrodotoxin, the blocker for voltage-gated Na^+ channels, we established that Twitch-2B$^+$ adult-born JGNs can be considered as active (i.e., spiking) when their Twitch-2B ratio is above 2.4 and non-active (i.e., electrically silent) when their Twitch-2B ratio is below 2.0 (Maslyukov et al., 2018).

To examine whether basal $[Ca^{2+}]_i$, reflected by the basal Twitch-2B ratio and the pattern of endogenous Ca^{2+} signaling can predict the fate of adult-born JGNs, we analyzed endogenous activity patterns of subsequently eliminated cells at DBD 2 (0-48 hours before cell death) and compared them to median activity patterns of all surviving adult-born JGNs recorded in the same mice at the same time points. The following parameters were quantified: basal Twitch-2B ratio, maximum Twitch-2B ratio, maximum ΔR/R amplitude, fraction of time spent in the active state, AUC/second (as illustrated in Figure 18A) and fraction of time spent in the silent state. Many parameters, including basal Twitch-2B ratio (Figure 18B), maximum Twitch-2B ratio (Figure 18C), fraction of time spent above 2.4 (Figure 18E), AUC/second (Figure 18F) and fraction of time spent below 2.0 (Figure 18G) were elevated in the subsequently eliminated adult-born JGNs ($P < 0.05$ for all comparisons, Wilcoxon signed rank test; n = 16 eliminated and 205 surviving cells from 8 mice). However, maximum ΔR/R amplitude (Figure 18D) was similar between these two groups.

Since it is known that there is a sharp rise of neuronal $[Ca^{2+}]_i$ at the late stage of apoptosis (Cellerino et al., 2000; Linden et al., 2005), we also analyzed the patterns of endogenous Ca^{2+} signaling of subsequently eliminated adult-born JGNs at DBD 6 (96-144 hours before death) and DBD 4 (48-96 hours before death). Except for the maximum ΔR/R amplitude at DBD 6 and DBD 4 and the fraction of time spent below 2.0 at DBD 4, all other analyzed parameters (Figure 18B-G) differed significantly between the subsequently eliminated and surviving adult-born JGNs ($P < 0.05$ for all comparisons, Wilcoxon signed rank test; DBD 6: n = 14 eliminated and 176 surviving cells from 7 mice; DBD 4: n = 20 eliminated and 220 surviving cells from 8 mice), suggesting the basal $[Ca^{2+}]_i$ and endogenous Ca^{2+} signaling pattern can be predictive for the survival/death of adult-born JGNs in the mouse OB.

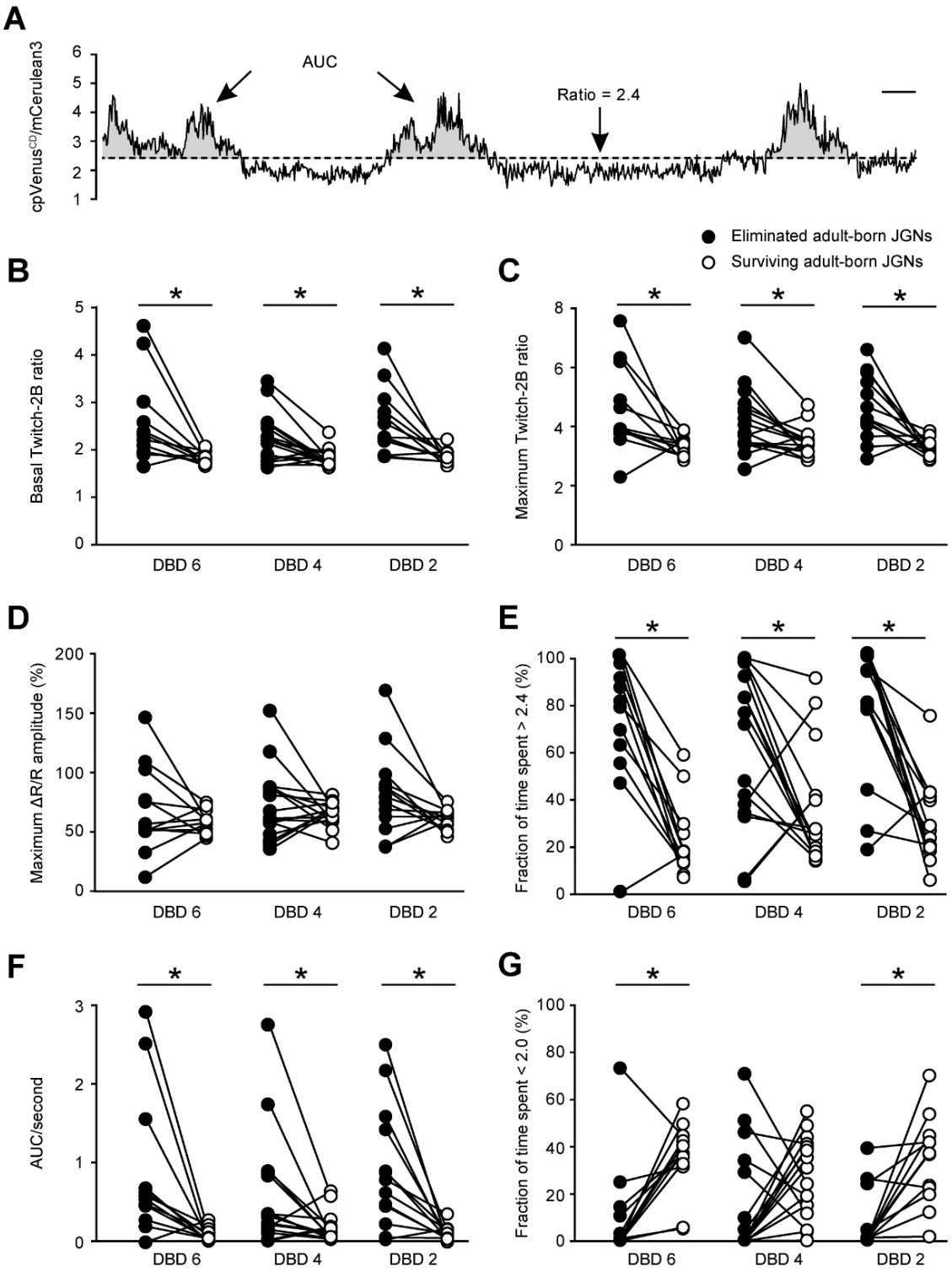

Figure 18. Different basal Twitch-2B ratios and endogenous activity patterns in eliminated and surviving adult-born JGNs. (**A**) Diagram illustrating the endogenous activity of adult-born JGNs and parameters used for its analyses. Cells were defined as active when their Twitch-2B ratio was above 2.4 and as non-active when their Twitch-2B ratio was below 2.0 (see Methods for details). AUC, the area under the curve. Scale bar: 5 s. (**B**-**G**) Connected dot graphs summarizing the median values of basal Twitch-2B ratio ($P < 0.05$, Wilcoxon signed rank test) (**B**), maximum Twitch-2B ratio ($P < 0.05$, Wilcoxon signed rank test) (**C**), maximum ΔR/R amplitude ($P > 0.05$, Paired *t* test) (**D**), fraction of time spent above 2.4 (i.e. in the active

state) (P < 0.05, Wilcoxon signed rank test) (**E**), the normalized area under the curve per second (AUC/second) (P < 0.05, Wilcoxon signed rank test) (**F**), fraction of time spent below 2.0 (in the non-active state) (P < 0.05 at DBD 6 and DBD 2, Wilcoxon signed rank test) (**G**) of eliminated cells and corresponding surviving cells of the same mice recorded in the DBD 6 (96-144 hours before cell death), DBD 4 (48-96 hours before cell death) and DBD 2 (0-48 hours before cell death) (DBD 6: n = 14 eliminated cells and 176 surviving cells, 7 mice; DBD 4: n = 20 eliminated cells and 220 surviving cells, 8 mice; DBD 2: n = 16 eliminated cells and 205 surviving cells, 8 mice).

Next, we investigated the stability of endogenous Ca^{2+} signaling in surviving and subsequently eliminated adult-born JGNs from DBD 6 to DBD 2. To this end, we took DBD 6 as a reference point, and calculated, for all parameters under this study, the differences between values measured at DBD 6 and at subsequent time points. Both for surviving and eliminated cells, the values measured in individual neurons scattered around zero. The median values, however, showed remarkable stability over the three recording sessions (Figure 19) (P > 0.05 for all comparisons, Friedman test; n = 8 eliminated cells and 138 surviving cells from 5 mice). For eliminated adult-born JGNs, we did observe there is a mild increase of basal Twitch-2B ratio (Figure 19A), maximum Twitch-2B ratio (Figure 19B) and maximum ΔR/R amplitude (Figure 19C) at DBD 2 compared to DBD 4 and DBD 6, probably reflecting the rise of $[Ca^{2+}]_I$ in some eliminated cells at the late stages of apoptosis, as described above. However, no significant differences have been detected between surviving and subsequently eliminated adult-born JGNs in terms of all the parameters measured (Figure 19) (P > 0.05 for all comparisons, Wilcoxon signed rank test; n = 8 eliminated cells and 138 surviving cells from 5 mice), indicating subsequently eliminated cells maintained the stable endogenous Ca^{2+} signaling as surviving cells.

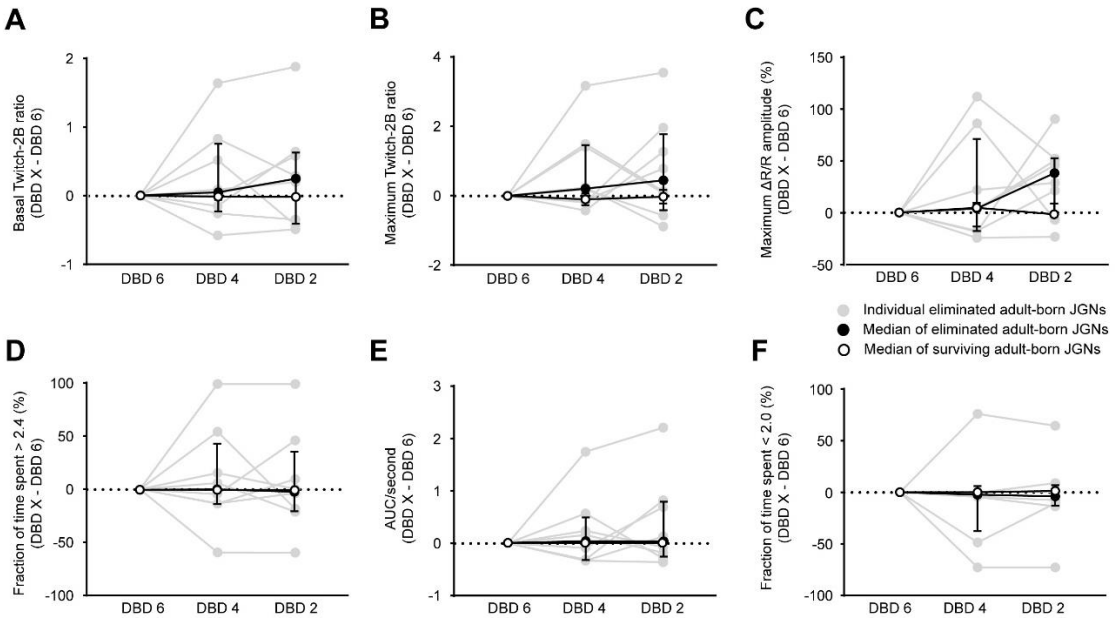

Figure 19. The stability of basal Twitch-2B ratios and endogenous activity patterns. (**A-F**) For each eliminated adult-born JGN as well as their corresponding surviving adult-born JGNs from the same mouse at the same time points, the differences between each time point (DBD 6, DBD 4 or DBD 2) and DBD 6 in terms of the following parameters were plotted: basal Twitch-2B ratio (**A**), maximum Twitch-2B ratio (**B**), maximum ΔR/R amplitude (**C**), fraction of time spent above 2.4 (**D**), the normalized AUC/second (**E**), fraction of time spent below 2.0 (**F**) ($P > 0.05$ for all comparisons, Friedman test for comparison of the same groups at different time points and Wilcoxon signed rank test for comparison of different groups at the same time points; n = 8 eliminated cells and 138 surviving cells from 5 mice).

It was suggested that fluctuations of $[Ca^{2+}]_i$ rather than mere Ca^{2+} influx are needed to drive the phosphorylation of nuclear cAMP-response-element-binding protein (CREB) (Li et al., 2016, 2009), a known key mediator of the development and survival of ABCs (Giachino et al., 2005; Jagasia et al., 2009). To determine whether adult-born JGNs were eliminated because their $[Ca^{2+}]_i$ was unable to fluctuate, we analyzed the fluctuation of $[Ca^{2+}]_i$ in adult-born JGNs (see Materials and Methods section for details). Interestingly, the fractions of fluctuating cells in the eliminated adult-born JGNs at DBD 6, DBD 4 and DBD 2 were not significantly different from those in surviving cells (Figure 20), suggesting the $[Ca^{2+}]_i$ of eliminated adult-born JGNs maintained the ability to fluctuate before their death ($P > 0.05$, Chi-square test with Yates' correction; DBD 6: n = 14 eliminated and 302 surviving cells from 7 mice, DBD 4: 20 eliminated and 465 surviving cells from 8 mice, DBD 2: 16 eliminated and 371 surviving cells from 8 mice).

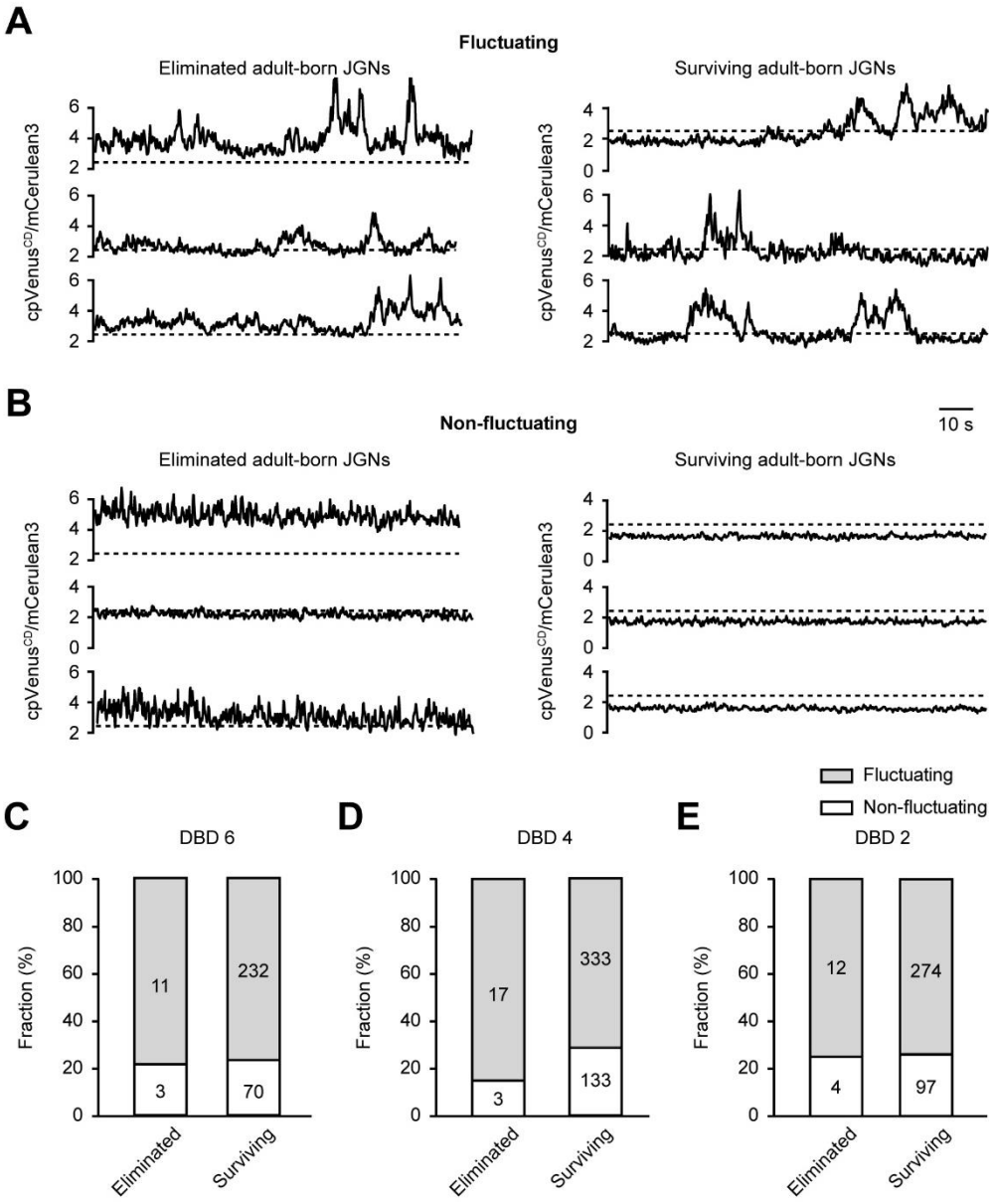

Figure 20. The analysis of $[Ca^{2+}]_i$ fluctuation in adult-born JGNs. (**A**) Representative traces of fluctuating eliminated (left) and fluctuating surviving (right) adult-born JGNs. (**B**) Representative traces of non-fluctuating eliminated (left) and non-fluctuating surviving adult-born JGNs (right). Scale bar: 10 s. (**C**-**E**) Bar graphs summarizing the fractions of fluctuating and non-fluctuating cells among the eliminated and surviving adult-born JGNs at DBD 6 (**C**) (P = 0.89, Chi-square test with Yates' correction), DBD 4 (**D**) (P = 0.29, Chi-square test with Yates' correction) and DBD 2 (**E**) (P= 0.84, Chi-square test with Yates' correction).

To conclude, the endogenous activity patterns and the accompanying ongoing changes in $[Ca^{2+}]_i$ differ significantly between the subsequently eliminated and surviving adult-born JGNs, with subsequently eliminated adult-born JGNs being subjected to enhanced endogenous Ca^{2+} signaling over prolonged periods of time.

4. Discussion

To our knowledge, this is the first *in vivo* study analyzing the morphological and functional properties of ABCs prior to their elimination. According to our conservative estimate, at least 20% of adult-born JGNs arriving in the glomerular layer of the bulb are subsequently eliminated. The elimination is largely accomplished till the end of the pre-integration phase, with no adult-born JGNs being eliminated after DPI 36. Surprisingly, the stable surviving adult-born JGNs spent the majority of their maturation time reducing and refining their dendritic trees, with adult-born PGCs and SACs showing a similar pattern of dendritic development. This knowledge could not be anticipated based on the previous population-based data, describing the net dendritic growth of adult-born JGNs as the major hallmark of maturation (Livneh et al., 2009, 2014; Mizrahi, 2007). Still, despite its developmental complexity, the dendritic morphogenesis occurred similarly in surviving and eliminated adult-born JGNs. In addition, we found that around 63% of the subsequently eliminated adult-born JGNs acquired odor-responsiveness prior to elimination, which, however, does not prevent their death. Finally, our data clearly showed that the levels of endogenous neuronal activity differ significantly between the surviving and subsequently eliminated adult-born JGNs. Unexpectedly, the death of adult-born JGNs is associated with a protracted increase in the endogenous neuronal activity, much in contrast to the previous concept, associating enhanced neuronal activity with an increased potential for the survival of ABCs (Lin et al., 2010).

4.1 Dendritic development of adult-born JGNs in the mouse OB

It is well established that migrating immature neurons have a highly polarized morphology: a prominent, long leading process and a short trailing process (Kaneko et al., 2017; Ota et al., 2014) This is also the case for migrating immature ABCs in the tangential migration phase in the RMS and in the radial migration phase in the deeper layers of the OB (Doetsch et al., 1997; Kaneko et

al., 2017). For adult-born GCs, which stop and settle down at the end of radial migration (Liang et al., 2016), the steady growth of dendritic tree (Sailor et al., 2016) is a natural step in the maturation process. However, after accomplishing radial migration, adult-born JGNs enter a 1-3 weeks long lateral migration phase, during which they migrate and simultaneously grow their dendritic trees (Kovalchuk et al., 2015; Liang et al., 2016). How these two processes influence each other remains unclear. We showed that those cells, which settle down by DPI 13, significantly reduce their dendritic complexity during the developmental process, even their primary dendrites can be removed (Figure 10). Although adult-born PGCs and SACs have very distinct dendritic morphology as described in the Introduction section, they shared a similar developmental pattern during the maturation process (Figure 12 and Figure 13). These data suggest that in adult-born JGNs, dendritic growth mainly occurs during the lateral migration phase, in line with our morphological data obtained at DPI 9-13 (Figure 13). Although surprising and counterintuitive at first glance, these data suggest that adult-born JGNs actively search for their parent glomeruli. To do so, while migrating they spread their dendrites around to sense activity patterns of many neighboring glomeruli. Once the parent glomeruli have been found, adult-born JGNs settle down and start to prune unnecessary dendrites. This hypothesis explains the necessity of extensive dendritic pruning and addition at early developmental stages (~2 weeks after their birth) (Figure 11). This hypothesis can also well explain the higher odor-responsiveness but lower odor-selectivity of immature adult-born JGNs (4 weeks after birth), when compared with their mature counterparts (8-9 weeks after birth) (Livneh et al., 2014). In fact, a similar concept might apply to adult-born GCs in the OB, which also show overshooting, albeit to much lesser extent (no primary dendrites are pruned and the fraction of dendritic overshooting is not as high as adult-born JGNs), of dendritic morphology (Sailor et al., 2016), as well as higher odor-responsiveness but lower odor-selectivity (Wallace et al., 2017) during the process of maturation after arrival in the OB.

Taken together, our data demonstrated that the net dendritic growth of adult-born JGNs happened in a rapid manner before the completion of lateral

migration in the glomerular layer. After the completion of later migration, the dendritic complexity of adult-born JGNs exhibited a clear decrease during the maturation process with adult-born PGCs and SACs showing a similar dendritic developmental pattern. Surprisingly, at early developmental stages (~2 weeks after the birth of cells), adult-born JGNs underwent both extensive addition and pruning.

4.2 Elimination of adult-born JGNs in the mouse OB

The use of nucleotide analog bromodeoxyuridine (BrdU) as the lineage-tracing tool revealed a significant level (~50%) of cell death among immature ABCs in the rodent OB (Petreanu and Alvarez-Buylla, 2002; Winner et al., 2002; Yamaguchi and Mori, 2005). Recently, an elegant *in vivo* study from Platel et al has cast doubt on the death of immature ABCs in the OB (Platel et al., 2019). By using Nestin-CreER^{T2}xRosa-RFP mice, the authors injected tamoxifen to induce RFP expression in the SVZ stem cells and all their progeny at 2 months of mouse age. Platel *et al* took advantage of two-photon imaging technique to study the integration and survival of red ABCs in the OB between week post-injection 1 and 8. Under these experimental conditions, only 1.5% of adult-born JGNs and 5.9% of adult-born GCs disappeared over the observation time period, prompting the authors to suggest that the previously observed cell death is caused by the toxicity of high doses of BrdU (Platel et al., 2019). Although our conservative estimation of the fraction of eliminated adult-born JGNs (~20%) is also a factor of 2 lower than the data obtained using BrdU, giving the room to the phenomenon of BrdU-mediated toxicity, it is still 10 times higher than that reported by Platel et. al. The explanation is likely to lie in the population-based nature of all previous studies. Indeed, when imaging many (20-170) red cells once a week (Platel et al., 2019), it is very difficult to account for vivid cell migration (Liang et al., 2016), the substitution of dying cells by late-coming ABCs (Sawada et al., 2011), etc. Moreover, studies showed survival of ABCs can be enhanced by modifications in olfactory sensory activity (Bovetti et al., 2009a; Forest et al., 2019a; Rochefort and Lledo, 2005; Sultan et al., 2011) or by knockdown of connective tissue growth factor in the whole bulb

(Khodosevich et al., 2013). This phenomenon cannot be explained if the death of ABCs is a rare event. Consistent with our data, longitudinal every 2nd day *in vivo* two-photon imaging of adult-born GCs revealed that ~21% of adult-born GCs were eliminated between DPI 24 and 56 (~0.7%/day decline in total cell number) (Sailor et al., 2016). Taken together, these data show that considerable fractions (at least 20%) of ABCs are eliminated after their arrival in their destination layers. For adult-born JGNs, the period of cell elimination seems to start at DPI 12 as ~6% of adult-born JGNs were eliminated at DPI 12-15 in our experiments (Figure 8E), somewhat earlier than assumed previously and last till DPI 36 only. This time window closely coincides with the period of lateral migration during the pre-integration phase (Liang et al., 2016).

4.3 Eliminated and surviving adult-born JGNs showed a similar level of dendritic complexity

It has been reported that sensory deprivation by unilateral naris closure has a negligible impact on the dendritic morphogenesis of ABCs in the OB (Mizrahi, 2007; Petreanu and Alvarez-Buylla, 2002), but decreases their survival (Corotto et al., 1994; Petreanu and Alvarez-Buylla, 2002; Sawada et al., 2011). Moreover, genetically moderate modulation of the endogenous activity of ABCs affects their fate but does not influence their dendritic morphology (Lin et al., 2010) These data documented the absence of the causal link between the dendritic morphology and fate of ABCs. However, some data showed the opposite results. Saghatelyan et al demonstrated that odor-deprivation decreased the dendritic complexity and also the survival of ABCs in the OB (Saghatelyan et al., 2005). Livneh et al showed that odor-enriched environment up-regulated the dendritic development of adult-born JGNs only in enriched glomeruli (Livneh et al., 2009) and odor-enriched environments are known to promote the survival of ABCs (Bovetti et al., 2009a; Forest et al., 2019a). (Bovetti et al., 2009b; Forest et al., 2019b). It is tentative to directly test whether there are any correlations between the dendritic morphology of ABCs and their fate. We recorded and analyzed the dendritic morphology of surviving and subsequently eliminated adult-born JGNs at DBD 3, DBD 2 and DBD 1 and

compared with the dendritic morphology of their surviving counterparts. We found there are no significant differences between these two groups in terms of all the parameters analyzed, including both the complexity of dendritic morphology and degree of dendritic remodeling (Figure 15). Although we can not exclude the possibilities that some subtle changes in the dendrites of eliminated adult-born JGNs may happen before their death, for example, thickness of dendrites, density of dendritic spines, spine size, spine length and so on (Segal, 2010), these data proved that the complexity of dendritic morphology and level of dendritic remodeling cannot distinguish surviving and subsequently eliminated adult-born JGNs in the OB, suggesting there are no correlations between the dendritic morphology of adult-born JGNs and their fate.

4.4 Fate of adult-born JGNs is independent of their ability to acquire odor-responsiveness

Since the critical period of ABC elimination corresponds to the pre-integration phase when ABCs start to receive synaptic inputs and integrate into the local circuitry, it has been postulated that immature ABCs die because they “fail to integrate” into the pre-existing neural circuitry (Lepousez and Lledo, 2011; Lin et al., 2010; Turnley et al., 2014). In this study, we took the cell’s odor-responsiveness as a read-out of its functional integration into surrounding neural circuitry. Interestingly, our data showed that ~63% of adult-born JGNs responded to odor stimulation before their death (Figure 17D), convincingly demonstrated that these adult-born JGNs acquired the ability to be odor responsive before their death. Note that the fraction (58.33%) of responding adult-born JGNs at the population level at DPI 20-32 in our experimental set (Figure 17C) is lower than that in previous reports (Kovalchuk et al., 2015; Livneh et al., 2014), mainly because we did not know which odorants should be applied to stimulate individual adult-born JGNs. As shown in the previous paper from our lab (Kovalchuk et al., 2015), this can be done by characterizing the responsiveness of their parent glomeruli to the stimulation of different odorants and then applying the odorants, to which their parent glomeruli are responsive, to stimulate the individual adult-born JGNs. Instead, we used a mixture of

odorants, which can achieve broad activation of the dorsal glomeruli (Kovalchuk et al., 2015; Livneh et al., 2014). Therefore, our data may underestimate the fraction of eliminated odor-responding adult-born JGNs. Nonetheless, it firmly documented that this fraction of eliminated odor-responding adult-born JGNs is substantial (≥ 63%). Nonetheless, our data demonstrated that the acquisition of odor-responsiveness does not prevent subsequent cell death. The question of whether these eliminated odor-responding adult-born JGNs were synaptically integrated or not remains to be addressed. Since there is a general consensus that PSD95-GFP puncta serve as a good proxy for putative synapses (Kelsch et al., 2008, 2009; Livneh et al., 2009), combined with the fact that the dendrites in every adult-born JGNs at DPI12-14 are studded with punctuated postsynaptic proteins PSD95 and the number of puncta increased during the maturation process (Livneh et al., 2009). Therefore, our eliminated odor-responsive adult-born JGNs, which were older than DPI 22, most likely were synaptically connected (i.e., integrated into the pre-existing circuitry) prior to their elimination.

Also, we found the parameters of odor-evoked responses analyzed (the maximum response amplitude and area under the curve) cannot distinguish the surviving and subsequently eliminated adult-born JGNs (Figure 17E,F), suggesting these two groups of ABCs responded similarly to the odor stimulation. However, we cannot exclude the possibility that other characteristics (e.g., odor selectivity or stability of odor responses) (Livneh et al., 2014; Wallace et al., 2017) may differ between these two groups of cells. Knocking out NMDARs revealed the critical role of synaptic inputs for the survival of ABCs (Kelsch et al., 2012; Mu et al., 2015; Tashiro et al., 2006). The death of NMDARs-deficient ABCs was fully rescued by increasing cell-intrinsic activity via NaChBac expression, suggesting that synaptic inputs-dependent survival of ABCs depends on the overall level of cell-intrinsic activity, regardless of its pattern (Lin et al., 2010). Our data provided direct evidence showing that the pattern of sensory input is not necessary for the survival of adult-born JGNs.

4.5 Different basal Ca^{2+} level and endogenous activity patterns in eliminated and surviving adult-born JGNs

Our data revealed that eliminated adult-born JGNs exhibited elevated endogenous Ca2+ signaling over a prolonged period of time, thus identifying the level of endogenous activity of adult-born JGNs as a potential predictor of cell's fate. This is in strong contrast to the literature suggesting that enhanced neuronal activity promotes the survival of immature adult-born GCs (Lin et al., 2010). Although the exact reason for this discrepancy remains to be discovered, it has to be noted that while the expression of sodium channel NaChBac increased survival of adult-born GCs in the OB (Lin et al., 2010)), it failed to do so in adult-born hippocampal GCs (Sim et al., 2013) (Sim et al, 2013), suggesting that different types of adult-born cells might possess different survival strategies, as described (Pfisterer and Khodosevich, 2017).

Having discovered that the subsequent elimination of adult-born JGNs can be predicted by the high level of their endogenous Ca^{2+} signaling, we hypothesized that this is due to the loss of fluctuations in $[Ca^{2+}]_i$, needed for optimal activation of the CREB-mediated survival program (Li et al., 2016, 2009). Surprisingly, the vast majority of subsequently eliminated adult-born JGNs maintained fluctuations in $[Ca^{2+}]_i$ even at DBD 2, right before the apoptosis (Figure 20). Although we cannot exclude that some subtle features of the fluctuation patterns, which are difficult to extract because of the inhomogeneity of the activity patterns in individual cells, do differ between the surviving and the eliminated cells, our current data suggest that the cell death in adult-born JGNs is triggered by the sustained increase in the overall level of $[Ca^{2+}]_i$.

Ca^{2+} is generally accepted as the most important intracellular messenger, mediates a variety of neuronal functions, such as the release of neurotransmitter, neurite outgrowth, gene transcription, neuronal survival, and so on (Hara and Snyder, 2007; Méndez-Armenta et al., 2014). It has been well known that neuronal apoptosis can be positively and negatively affected by the altered intracellular Ca^{2+} homeostasis and also the subtle changes in intracellular Ca^{2+} distribution within the compartment (Orrenius et al., 2003;

Toescu, 1998). Molecular mechanisms underlying the elevated $[Ca^{2+}]_i$ related apoptosis are diverse. For example, Cadmium-induced elevation of $[Ca^{2+}]_i$ stimulates the phosphorylation of calcium/calmodulin-dependent protein kinase II (CaMKII) and activates of the mitogen-activated protein kinases (MAPK) and the mammalian target of rapamycin (mTOR) signaling pathways, which lead to neuronal apoptosis (Chen et al., 2011; Xu et al., 2011). Oxidative stress increased $[Ca^{2+}]_i$ results in enhanced production of reactive oxygen species (ROS), which can trigger the activation of the caspase-dependent apoptosis pathway (Annunziato et al., 2003; Méndez-Armenta et al., 2014). The molecular mechanism underlying the enhanced endogenous $[Ca^{2+}]_i$-related elimination of adult-born JGNs remains to be discovered.

In summary, our study identifies the ongoing endogenous activity as a key player influencing the fate of adult-born JGNs. Such ongoing activity can integrate both the cell-intrinsic firing and the influence of the steady-state odor environment reaching either a pro- or an anti-apoptotic level. Because some odorants increase and the others decrease the levels of endogenous activity in JGNs (Homma et al., 2013), this model reconciles the seemingly opposing findings showing that odor enrichment either decreases (Khodosevich et al., 2013) or increases (Bonzano et al., 2014; Forest et al., 2019b; Rochefort et al., 2002) the survival of adult-born JGNs.

Summary

Thousands of adult-born cells are generated and migrate into the rodent olfactory bulb on a daily basis. These adult-born cells differentiate and mature into two types of inhibitory neurons in the OB: granule cells and juxtaglomerular neurons (JGNs), which play important roles in processing olfactory information. BrdU incorporation studies showed that ~50% of adult-born cells were subsequently eliminated and this elimination depended on the sensory experience. Indeed, the odor-enriched environment promotes the survival of adult-born neurons while odor deprivation inhibits it. However, the morphological and functional properties of adult-born cells before their death remain elusive. Therefore, the major aim of this project was to examine whether the morphological and functional properties of adult-born cells can predict their survival/death. This question can be conveniently addressed *in vivo* in adult-born JGNs because of their superficial location in the mouse OB.

For the first set of experiments, we labeled adult-born cells by injecting a mixture of retroviruses encoding RGB fluorescent proteins to achieve precise identification of migrating adult-born JGNs at early developmental stages. The fate together with the dendritic morphology of adult-born JGNs was recorded on a daily basis with two-photon microscopy during the critical period for cell elimination (day post injection (DPI) 12 – DPI 45). We found that stable surviving adult-born JGNs showed a clear reduction in the complexity of their dendritic morphology throughout the maturation process from DPI 13 to DPI 45 but exhibited a brief period of rapid dendritic growth at DPI 9-13. Interestingly, at early developmental stages they underwent both extensive dendritic addition and pruning. Although may be underestimated, We found that ~20% of eliminated adult-born JGNs died between DPI 12 and DPI 45 (although this number might be underestimated due to stringent criteria used for identifying cell death) and that the critical period for cell elimination starts somewhat earlier than previously thought (~6% of adult-born JGNs were eliminated as early as DPI 12-15). However, both the complexity of the dendritic tree and the degree of dendritic remodeling were not able to differentiate the surviving and

subsequently eliminated adult-born JGNs shortly (1-3 days) before their death. Together, these data suggest that the morphology of the dendritic tree of adult-born JGNs cannot predict their fate.

In the second set of experiments, we expressed the ratiometric Ca^{2+} indicator Twitch-2B in adult-born cells to record both their endogenous activity and their odor-evoked responses. Around 60% of eliminated adult-born JGNs responded to odor stimuli before their death. Moreover, the responses of the eliminated and surviving adult-born JGNs were similar in terms of the response amplitude and area under the curve. These data suggest the fate determination of adult-born JGNs is independent of the acquired odor responsiveness. However, the eliminated auld-born JGNs possessed higher basal Ca^{2+} levels that surviving cells from the same mice and showed a long-lasting enhancement of the ongoing endogenous Ca^{2+} signaling.

In conclusion, our data demonstrate that adult-born JGNs can still be eliminated after acquiring the ability to respond to odorants, so the “integration into the neural circuitry” cannot protect them from elimination. Moreover, their fate can be fatefully predicted by the enhanced levels of the ongoing endogenous activity, whereas the phasic sensory-driven activity and dendritic morphology are similar between the eliminated and the surviving cells.

Zusammenfassung

Tausende Zellen werden täglich im adulten Gehirn von Nagetieren erzeugt und wandern in den Riechkolben ein. Diese im Adulten geborenen Zellen differenzieren sich und reifen zu zwei Arten von inhibitorischen Neuronen an: Körnerzellen und juxtaglomeruläre Zellen (JGZ), die beide eine wichtige Rolle bei der Verarbeitung von olfaktorischen Informationen spielen. Studien haben gezeigt dass ~ 50% der im Adulten geborenen Zellen zwischen 12 und 45 Tagen nach ihrer Geburt eliminiert wurden. Dabei fördert eine mit Gerüchen angereicherte Umgebung das Überleben der im Adulten geborenen Zellen während der Geruchsmangel hemmt das Überleben der Zellen. Ob die im Adulten geborenen Zellen bestimmte morphologische und funktionelle Merkmale besitzen, die ihrem Tod vorausgehen, ist jedoch noch nicht bekannt. Daher war das Hauptziel dieser Arbeit zu untersuchen, ob die morphologischen und funktionellen Eigenschaften von der im Adulten geborenen Zellen ihr Überleben/Tod vorhersagen können. Diese Frage kann *in vivo* mit Hilfe von juxtaglomerulären Zellen beantwortet werden, weil sie oberflächlich im Riechkolben der Maus liegen.

Für den ersten experimentellen Teil der Arbeit markierten wir die adult-geborenen Zellen durch Injektion einer Mischung von Retroviren, die für rote, grüne und blaue (RGB) fluoreszierende Proteine kodieren, um die migrierende adult-geborenen JGZ in frühen Entwicklungsstadien zu identifizieren. Da die Retroviren nur die sich teilenden Zellen markieren, gibt die Zeit nach der Virusinjektion (*day post injection*, DPI) das Alter der Zellen an. Die dendritische Morphologie von im Adulten geborenen JGZ wurde während des kritischen Zeitfensters für im Adulten geborene JGZ (DPI 12 - DPI 45) täglich mittels Zwei-Photonen-Mikroskopie aufgezeichnet. Wir fanden bei überlebenden im Adulten geborenen JGZ nach einer kurzen Phase schnellen Wachstums bei DPI 9-13, eine deutliche Verringerung der Komplexität ihrer dendritischen Morphologie während des Reifungsprozesses (von DPI 13 bis zum DPI 45). Interessanterweise erfuhren sie in frühen Entwicklungsstadien ein Hinzufügen als auch ein Wegnehmen ihrer dendritischen Zweige. Wir fanden aus, dass

ungefähr 20% der eliminierten im Adulten geborenen im Adulten geborenen JGZ zwischen DPI 12 auf DPI 45 eliminiert wurden. Diese Zahl ist möglicherweise unterschätzt, da wir sehr stringente Kriterien für Zelltod anwandten. Interessanterweise begann der Zeitraum der Zellelimination früher als gedacht, da ~ 6% der im Adulten geborenen JGZ bei DPI 12-15 eliminiert wurden. Sowohl die Komplexität des dendritischen Baums als auch der Grad der dendritischen Umgestaltung gaben jedoch kein Indiz dafür, ob die JGZ sterben werden. Zusammengenommen legen diese Daten nahe, dass sich das Schicksal der im Adulten geborenen JGZ nicht durch ihre dendritische Morphologie vorhersagen lässt.

Im zweiten experimentellen Teil der Arbeit exprimierten wir in den im Adulten geborenen Zellen den ratiometrischen Ca^{2+} Indikator Twitch-2B, um ihre endogene Aktivität sowie die Antworten auf Duftstoffe zu messen. Etwa 60% der im Nachhinein eliminierten im Adulten geborenen JGZ konnen vor ihrem Tod auf die sensorischen Reize (Duftstoffe) reagieren. Eliminierte und überlebende adult-geborenen JGZ reagierten ähnlich auf Duftstoffe bezüglich der Antwortamplitude und Fläche unter der Antwort-kurve. Diese Daten legen nahe, dass die Schicksalsentscheidung von im Adulten geborenen JGZ unabhängig von ihrer erworbenen Duftstoff-Ansprechbarkeit ist. Interessanterweise zeigten die künftig eliminierten im Adulten geborenen JGZ ein anhaltend erhöhtes basales Ca^{2+} Niveau und erhöhte endogene Ca^{2+} Signalgebung verglichen zu den überlebenden Zellen.

Zusammenfassend zeigen unsere Daten, dass adult-geborenen JGZ noch eliminiert werden können, sogar nachdem sie bereits die Duftstoff-Ansprechbarkeit erworben haben. Ihre langanhaltende verstärkte endogene Aktivität, jedoch nicht ihre Duftstoffaktivität oder ihre dendritische Morphologie, kann ihr Schicksal vorhersagen.

References

Alonso, M., Viollet, C., Gabellec, M.-M., Meas-Yedid, V., Olivo-Marin, J.-C., and Lledo, P.-M. (2006). Olfactory Discrimination Learning Increases the Survival of Adult-Born Neurons in the Olfactory Bulb. J. Neurosci. *26*, 10508–10513.

Alonso, M., Lepousez, G., Wagner, S., Bardy, C., Gabellec, M.-M., Torquet, N., and Lledo, P.-M. (2012). Activation of adult-born neurons facilitates learning and memory. Nat Neurosci *15*, 897–904.

Altman, J. (1963). Autoradiographic investigation of cell proliferation in the brains of rats and cats. The Anatomical Record *145*, 573–591.

Altman, J. (1969). Autoradiographic and histological studies of postnatal neurogenesis. IV. Cell proliferation and migration in the anterior forebrain, with special reference to persisting neurogenesis in the olfactory bulb. Journal of Comparative Neurology *137*, 433–457.

Altman, J., and Das, G.D. (1965). Autoradiographic and histological evidence of postnatal hippocampal neurogenesis in rats. Journal of Comparative Neurology *124*, 319–335.

Annunziato, L., Amoroso, S., Pannaccione, A., Cataldi, M., Pignataro, G., D'Alessio, A., Sirabella, R., Secondo, A., Sibaud, L., and Di Renzo, G.F. (2003). Apoptosis induced in neuronal cells by oxidative stress: role played by caspases and intracellular calcium ions. Toxicology Letters *139*, 125–133.

Aungst, J.L., Heyward, P.M., Puche, A.C., Karnup, S.V., Hayar, A., Szabo, G., and Shipley, M.T. (2003). Centre–surround inhibition among olfactory bulb glomeruli. Nature *426*, 623–629.

Balu, R., Pressler, R.T., and Strowbridge, B.W. (2007). Multiple Modes of Synaptic Excitation of Olfactory Bulb Granule Cells. J. Neurosci. *27*, 5621–5632.

Bath, K.G., Mandairon, N., Jing, D., Rajagopal, R., Kapoor, R., Chen, Z.-Y., Khan, T., Proenca, C.C., Kraemer, R., Cleland, T.A., et al. (2008). Variant Brain-Derived Neurotrophic Factor (Val66Met) Alters Adult Olfactory Bulb Neurogenesis and Spontaneous Olfactory Discrimination. J. Neurosci. *28*, 2383–2393.

Belluzzi, O., Benedusi, M., Ackman, J., and LoTurco, J.J. (2003). Electrophysiological Differentiation of New Neurons in the Olfactory Bulb. J. Neurosci. *23*, 10411–10418.

Benn, S.C., and Woolf, C.J. (2004). Adult neuron survival strategies — slamming on the brakes. Nature Reviews Neuroscience *5*, 686–700.

Biebl, M., Winner, B., and Winkler, J. (2005). Caspase inhibition decreases cell death in regions of adult neurogenesis. Neuroreport *16*, 1147–1150.

Boldrini, M., Fulmore, C.A., Tartt, A.N., Simeon, L.R., Pavlova, I., Poposka, V., Rosoklija, G.B., Stankov, A., Arango, V., Dwork, A.J., et al. (2018). Human Hippocampal Neurogenesis Persists throughout Aging. Cell Stem Cell *22*, 589-599.e5.

Bond, A.M., Ming, G., and Song, H. (2015). Adult Mammalian Neural Stem Cells and Neurogenesis: Five Decades Later. Cell Stem Cell *17*, 385–395.

Bonzano, S., Bovetti, S., Fasolo, A., Peretto, P., and De Marchis, S. (2014). Odour enrichment increases adult-born dopaminergic neurons in the mouse olfactory bulb. Eur J Neurosci *40*, 3450–3457.

Bordiuk, O.L., Smith, K., Morin, P.J., and Semënov, M.V. (2014). Cell Proliferation and Neurogenesis in Adult Mouse Brain. PLOS ONE *9*, e111453.

Borisovska, M., Bensen, A.L., Chong, G., and Westbrook, G.L. (2013). Distinct Modes of Dopamine and GABA Release in a Dual Transmitter Neuron. J. Neurosci. *33*, 1790–1796.

Bovetti, S., Hsieh, Y.-C., Bovolin, P., Perroteau, I., Kazunori, T., and Puche, A.C. (2007). Blood Vessels Form a Scaffold for Neuroblast Migration in the Adult Olfactory Bulb. J. Neurosci. *27*, 5976–5980.

Bovetti, S., Veyrac, A., Peretto, P., Fasolo, A., and Marchis, S.D. (2009a). Olfactory Enrichment Influences Adult Neurogenesis Modulating GAD67 and Plasticity-Related Molecules Expression in Newborn Cells of the Olfactory Bulb. PLOS ONE *4*, e6359.

Bovetti, S., Veyrac, A., Peretto, P., Fasolo, A., and De Marchis, S. (2009b). Olfactory Enrichment Influences Adult Neurogenesis Modulating GAD67 and Plasticity-Related Molecules Expression in Newborn Cells of the Olfactory Bulb. PLoS ONE *4*, e6359.

Breton-Provencher, V., Lemasson, M., Peralta, M.R., and Saghatelyan, A. (2009). Interneurons Produced in Adulthood Are Required for the Normal Functioning of the Olfactory Bulb Network and for the Execution of Selected Olfactory Behaviors. J. Neurosci. *29*, 15245–15257.

Brill, M.S., Ninkovic, J., Winpenny, E., Hodge, R.D., Ozen, I., Yang, R., Lepier, A., Gascón, S., Erdelyi, F., Szabo, G., et al. (2009). Adult generation of glutamatergic olfactory bulb interneurons. Nat Neurosci *12*, 1524–1533.

Buck, L., and Axel, R. (1991). A novel multigene family may encode odorant receptors: A molecular basis for odor recognition. Cell *65*, 175–187.

Bywalez, W.G., Ona-Jodar, T., Lukas, M., Ninkovic, J., and Egger, V. (2017). Dendritic Arborization Patterns of Small Juxtaglomerular Cell Subtypes within the Rodent Olfactory Bulb. Front. Neuroanat. *10*, 127.

Carlén, M., Cassidy, R.M., Brismar, H., Smith, G.A., Enquist, L.W., and Frisén, J. (2002). Functional Integration of Adult-Born Neurons. Current Biology *12*, 606–608.

Carleton, A., Petreanu, L.T., Lansford, R., Alvarez-Buylla, A., and Lledo, P.-M. (2003). Becoming a new neuron in the adult olfactory bulb. Nature Neuroscience *6*, 507–518.

Cellerino, A., Galli-Resta, L., and Colombaioni, L. (2000). The Dynamics of Neuronal Death: A Time-Lapse Study in the Retina. J. Neurosci. *20*, RC92–RC92.

Chen, S., Xu, Y., Xu, B., Guo, M., Zhang, Z., Liu, L., Ma, H., Chen, Z., Luo, Y., Huang, S., et al. (2011). CaMKII is involved in cadmium activation of MAPK and mTOR pathways leading to neuronal cell death. Journal of Neurochemistry *119*, 1108–1118.

Cleland, T.A., and Linster, C. (2005). Computation in the Olfactory System. Chem Senses *30*, 801–813.

Cordeiro, M.F., Guo, L., Luong, V., Harding, G., Wang, W., Jones, H.E., Moss, S.E., Sillito, A.M., and Fitzke, F.W. (2004). Real-time imaging of single nerve cell apoptosis in retinal neurodegeneration. Proc Natl Acad Sci U S A *101*, 13352–13356.

Corotto, F.S., Henegar, J.R., and Maruniak, J.A. (1994). Odor deprivation leads to reduced neurogenesis and reduced neuronal survival in the olfactory bulb of the adult mouse. Neuroscience *61*, 739–744.

Costantini, L.M., Baloban, M., Markwardt, M.L., Rizzo, M., Guo, F., Verkhusha, V.V., and Snapp, E.L. (2015). A palette of fluorescent proteins optimized for diverse cellular environments. Nature Communications *6*, 1–13.

Darcy, D.P., and Isaacson, J.S. (2009). L-Type Calcium Channels Govern Calcium Signaling in Migrating Newborn Neurons in the Postnatal Olfactory Bulb. J. Neurosci. *29*, 2510–2518.

Denizet, M., Cotter, L., Lledo, P.-M., and Lazarini, F. (2017). Sensory deprivation increases phagocytosis of adult-born neurons by activated microglia in the olfactory bulb. Brain, Behavior, and Immunity *60*, 38–43.

Doetsch, F., García-Verdugo, J.M., and Alvarez-Buylla, A. (1997). Cellular Composition and Three-Dimensional Organization of the Subventricular Germinal Zone in the Adult Mammalian Brain. J. Neurosci. *17*, 5046–5061.

Doetsch, F., Caillé, I., Lim, D.A., García-Verdugo, J.M., and Alvarez-Buylla, A. (1999). Subventricular Zone Astrocytes Are Neural Stem Cells in the Adult Mammalian Brain. Cell *97*, 703–716.

Dulac, C., and Torello, A.T. (2003). Molecular detection of pheromone signals in mammals: from genes to behaviour. Nature Reviews Neuroscience *4*, 551–562.

Durand, G.M., Kovalchuk, Y., and Konnerth, A. (1996). Long-term potentiation and functional synapse induction in developing hippocampus. Nature *381*, 71–75.

Elmore, S. (2007). Apoptosis: A Review of Programmed Cell Death. Toxicol Pathol *35*, 495–516.

Enwere, E., Shingo, T., Gregg, C., Fujikawa, H., Ohta, S., and Weiss, S. (2004). Aging Results in Reduced Epidermal Growth Factor Receptor Signaling, Diminished Olfactory Neurogenesis, and Deficits in Fine Olfactory Discrimination. J. Neurosci. *24*, 8354–8365.

Eriksson, P.S., Perfilieva, E., Björk-Eriksson, T., Alborn, A.-M., Nordborg, C., Peterson, D.A., and Gage, F.H. (1998). Neurogenesis in the adult human hippocampus. Nat Med *4*, 1313–1317.

Forest, J., Moreno, M., Cavelius, M., Chalençon, L., Ziessel, A., Sacquet, J., Richard, M., Didier, A., and Mandairon, N. (2019a). Short-term availability of adult-born neurons for memory encoding. Nature Communications *10*, 1–9.

Forest, J., Moreno, M., Cavelius, M., Chalençon, L., Ziessel, A., Sacquet, J., Richard, M., Didier, A., and Mandairon, N. (2019b). Short-term availability of adult-born neurons for memory encoding. Nature Communications *10*.

Frazier-Cierpial, L., and Brunjes, P.C. (1989). Early postnatal cellular proliferation and survival in the olfactory bulb and rostral migratory stream of normal and unilaterally odor-deprived rats. Journal of Comparative Neurology *289*, 481–492.

Fuentealba, L.C., Rompani, S.B., Parraguez, J.I., Obernier, K., Romero, R., Cepko, C.L., and Alvarez-Buylla, A. (2015). Embryonic Origin of Postnatal Neural Stem Cells. Cell *161*, 1644–1655.

Furutachi, S., Miya, H., Watanabe, T., Kawai, H., Yamasaki, N., Harada, Y., Imayoshi, I., Nelson, M., Nakayama, K.I., Hirabayashi, Y., et al. (2015). Slowly dividing neural progenitors are an embryonic origin of adult neural stem cells. Nat Neurosci *18*, 657–665.

Garcia, A.D.R., Doan, N.B., Imura, T., Bush, T.G., and Sofroniew, M.V. (2004). GFAP-expressing progenitors are the principal source of constitutive neurogenesis in adult mouse forebrain. Nature Neuroscience *7*, 1233–1241.

García-González, D., Khodosevich, K., Watanabe, Y., Rollenhagen, A., Lübke, J.H.R., and Monyer, H. (2017). Serotonergic Projections Govern Postnatal Neuroblast Migration. Neuron *94*, 534-549.e9.

Gheusi, G., Cremer, H., McLean, H., Chazal, G., Vincent, J.-D., and Lledo, P.-M. (2000). Importance of newly generated neurons in the adult olfactory bulb for odor discrimination. PNAS *97*, 1823–1828.

Giachino, C., Marchis, S.D., Giampietro, C., Parlato, R., Perroteau, I., Schütz, G., Fasolo, A., and Peretto, P. (2005). cAMP Response Element-Binding Protein Regulates Differentiation and Survival of Newborn Neurons in the Olfactory Bulb. J. Neurosci. *25*, 10105–10118.

Gire, D.H., Restrepo, D., Sejnowski, T.J., Greer, C., De Carlos, J.A., and Lopez-Mascaraque, L. (2013). Temporal Processing in the Olfactory System: Can We See a Smell? Neuron *78*, 416–432.

Gomez-Nicola, D., Riecken, K., Fehse, B., and Perry, V.H. (2014). In-vivo RGB marking and multicolour single-cell tracking in the adult brain. Sci Rep *4*, 1–10.

Gonçalves, J.T., Bloyd, C.W., Shtrahman, M., Johnston, S.T., Schafer, S.T., Parylak, S.L., Tran, T., Chang, T., and Gage, F.H. (2016). In vivo imaging of dendritic pruning in dentate granule cells. Nat Neurosci *19*, 788–791.

Gould, E., and Gross, C.G. (2002). Neurogenesis in Adult Mammals: Some Progress and Problems. J. Neurosci. *22*, 619–623.

Gratzner, H.G. (1982). Monoclonal antibody to 5-bromo- and 5-iododeoxyuridine: A new reagent for detection of DNA replication. Science *218*, 474–475.

Grubb, M.S., Nissant, A., Murray, K., and Lledo, P.-M. (2008). Functional Maturation of the First Synapse in Olfaction: Development and Adult Neurogenesis. J. Neurosci. *28*, 2919–2932.

Halabisky, B., Friedman, D., Radojicic, M., and Strowbridge, B.W. (2000). Calcium Influx through NMDA Receptors Directly Evokes GABA Release in Olfactory Bulb Granule Cells. J. Neurosci. *20*, 5124–5134.

Hara, M.R., and Snyder, S.H. (2007). Cell Signaling and Neuronal Death. Annual Review of Pharmacology and Toxicology *47*, 117–141.

Hayar, A., Karnup, S., Shipley, M.T., and Ennis, M. (2004a). Olfactory Bulb Glomeruli: External Tufted Cells Intrinsically Burst at Theta Frequency and Are Entrained by Patterned Olfactory Input. J. Neurosci. *24*, 1190–1199.

Hayar, A., Karnup, S., Ennis, M., and Shipley, M.T. (2004b). External Tufted Cells: A Major Excitatory Element That Coordinates Glomerular Activity. J. Neurosci. *24*, 6676–6685.

Hayar, A., Shipley, M.T., and Ennis, M. (2005). Olfactory Bulb External Tufted Cells Are Synchronized by Multiple Intraglomerular Mechanisms. J. Neurosci. *25*, 8197–8208.

Holy, T.E. (2018). The Accessory Olfactory System: Innately Specialized or Microcosm of Mammalian Circuitry? Annual Review of Neuroscience *41*, 501–525.

Homma, R., Kovalchuk, Y., Konnerth, A., Cohen, L.B., and Garaschuk, O. (2013). In vivo functional properties of juxtaglomerular neurons in the mouse olfactory bulb. Front Neural Circuits *7*.

Igarashi, K.M., Ieki, N., An, M., Yamaguchi, Y., Nagayama, S., Kobayakawa, K., Kobayakawa, R., Tanifuji, M., Sakano, H., Chen, W.R., et al. (2012). Parallel Mitral and Tufted Cell Pathways Route Distinct Odor Information to Different Targets in the Olfactory Cortex. J. Neurosci. *32*, 7970–7985.

Imai, T. (2014). Construction of functional neuronal circuitry in the olfactory bulb. Seminars in Cell & Developmental Biology *35*, 180–188.

Imamura, F., and Greer, C.A. (2009). Dendritic Branching of Olfactory Bulb Mitral and Tufted Cells: Regulation by TrkB. PLOS ONE *4*, e6729.

Imayoshi, I., Sakamoto, M., Ohtsuka, T., Takao, K., Miyakawa, T., Yamaguchi, M., Mori, K., Ikeda, T., Itohara, S., and Kageyama, R. (2008). Roles of continuous neurogenesis in the structural and functional integrity of the adult forebrain. Nature Neuroscience *11*, 1153–1161.

Isaacson, J.S., and Strowbridge, B.W. (1998). Olfactory Reciprocal Synapses: Dendritic Signaling in the CNS. Neuron *20*, 749–761.

Jablonska, B., Aguirre, A., Raymond, M., Szabo, G., Kitabatake, Y., Sailor, K.A., Ming, G.-L., Song, H., and Gallo, V. (2010). Chordin-induced lineage plasticity of adult SVZ neuroblasts after demyelination. Nature Neuroscience *13*, 541–550.

Jagasia, R., Steib, K., Englberger, E., Herold, S., Faus-Kessler, T., Saxe, M., Gage, F.H., Song, H., and Lie, D.C. (2009). GABA-cAMP Response Element-Binding Protein Signaling Regulates Maturation and Survival of Newly Generated Neurons in the Adult Hippocampus. J. Neurosci. *29*, 7966–7977.

Jan, D.D.S., Hirnet, D., Westbrook, G.L., and Charpak, S. (2009). External Tufted Cells Drive the Output of Olfactory Bulb Glomeruli. J. Neurosci. *29*, 2043–2052.

Jankovski, A., Garcia, C., Soriano, E., and Sotelo, C. (1998). Proliferation, migration and differentiation of neuronal progenitor cells in the adult mouse subventricular zone surgically separated from its olfactory bulb. European Journal of Neuroscience *10*, 3853–3868.

Jones, D.T., and Reed, R.R. (1989). Golf: an olfactory neuron specific-G protein involved in odorant signal transduction. Science *244*, 790–795.

Kadohisa, M. (2013). Effects of odor on emotion, with implications. Front. Syst. Neurosci. *7*.

Kalamakis, G., Brüne, D., Ravichandran, S., Bolz, J., Fan, W., Ziebell, F., Stiehl, T., Catalá-Martinez, F., Kupke, J., Zhao, S., et al. (2019). Quiescence Modulates Stem Cell Maintenance and Regenerative Capacity in the Aging Brain. Cell *176*, 1407-1419.e14.

Kaneko, N., Sawada, M., and Sawamoto, K. (2017). Mechanisms of neuronal migration in the adult brain. Journal of Neurochemistry *141*, 835–847.

Kelsch, W., Lin, C.-W., and Lois, C. (2008). Sequential development of synapses in dendritic domains during adult neurogenesis. PNAS *105*, 16803–16808.

Kelsch, W., Lin, C.-W., Mosley, C.P., and Lois, C. (2009). A Critical Period for Activity-Dependent Synaptic Development during Olfactory Bulb Adult Neurogenesis. J. Neurosci. *29*, 11852–11858.

Kelsch, W., Li, Z., Eliava, M., Goengrich, C., and Monyer, H. (2012). GluN2B-Containing NMDA Receptors Promote Wiring of Adult-Born Neurons into Olfactory Bulb Circuits. J. Neurosci. *32*, 12603–12611.

Khazipov, R., and Luhmann, H.J. (2006). Early patterns of electrical activity in the developing cerebral cortex of humans and rodents. Trends in Neurosciences *29*, 414–418.

Khodosevich, K., Lazarini, F., von Engelhardt, J., Kaneko, H., Lledo, P.-M., and Monyer, H. (2013). Connective Tissue Growth Factor Regulates Interneuron Survival and Information Processing in the Olfactory Bulb. Neuron *79*, 1136–1151.

Kirschenbaum, B., Doetsch, F., Lois, C., and Alvarez-Buylla, A. (1999). Adult Subventricular Zone Neuronal Precursors Continue to Proliferate and Migrate in the Absence of the Olfactory Bulb. J. Neurosci. *19*, 2171–2180.

Kiyokage, E., Pan, Y.-Z., Shao, Z., Kobayashi, K., Szabo, G., Yanagawa, Y., Obata, K., Okano, H., Toida, K., Puche, A.C., et al. (2010). Molecular Identity of Periglomerular and Short Axon Cells. J. Neurosci. *30*, 1185–1196.

Kopel, H., Schechtman, E., Groysman, M., and Mizrahi, A. (2012). Enhanced Synaptic Integration of Adult-Born Neurons in the Olfactory Bulb of Lactating Mothers. J. Neurosci. *32*, 7519–7527.

Kosaka, T., and Kosaka, K. (2011). “Interneurons” in the olfactory bulb revisited. Neuroscience Research *69*, 93–99.

Kovalchuk, Y., Homma, R., Liang, Y., Maslyukov, A., Hermes, M., Thestrup, T., Griesbeck, O., Ninkovic, J., Cohen, L.B., and Garaschuk, O. (2015). In vivo odourant response properties of migrating adult-born neurons in the mouse olfactory bulb. Nat Commun *6*, 1–12.

Kriegstein, A., and Alvarez-Buylla, A. (2009). The Glial Nature of Embryonic and Adult Neural Stem Cells. Annual Review of Neuroscience *32*, 149–184.

Kuhn, H.G. (2015). Control of Cell Survival in Adult Mammalian Neurogenesis. Cold Spring Harb Perspect Biol *7*, a018895.

Lacar, B., Young, S.Z., Platel, J.-C., and Bordey, A. (2011). Gap junction-mediated calcium waves define communication networks among murine postnatal neural progenitor cells. European Journal of Neuroscience *34*, 1895–1905.

Lee, P.-C., He, H., Lin, C.-Y., Ching, Y.-T., and Cline, H.T. (2013). Computer Aided Alignment and Quantitative 4D Structural Plasticity Analysis of Neurons. Neuroinform *11*, 249–257.

Leinwand, S.G., and Chalasani, S.H. (2011). Olfactory networks: from sensation to perception. Current Opinion in Genetics & Development *21*, 806–811.

Lepousez, G., and Lledo, P.-M. (2011). Life and Death Decision in Adult Neurogenesis: In Praise of Napping. Neuron *71*, 768–771.

Lepousez, G., Valley, M.T., and Lledo, P.-M. (2013). The Impact of Adult Neurogenesis on Olfactory Bulb Circuits and Computations. Annual Review of Physiology *75*, 339–363.

Li, B., Tadross, M.R., and Tsien, R.W. (2016). Sequential ionic and conformational signaling by calcium channels drives neuronal gene expression. Science *351*, 863–867.

Li, S., Zhang, C., Takemori, H., Zhou, Y., and Xiong, Z.-Q. (2009). TORC1 Regulates Activity-Dependent CREB-Target Gene Transcription and Dendritic Growth of Developing Cortical Neurons. J. Neurosci. *29*, 2334–2343.

Li, W.L., Chu, M.W., Wu, A., Suzuki, Y., Imayoshi, I., and Komiyama, T. (2018). Adult-born neurons facilitate olfactory bulb pattern separation during task engagement. ELife *7*, e33006.

Liang, Y., Li, K., Riecken, K., Maslyukov, A., Gomez-Nicola, D., Kovalchuk, Y., Fehse, B., and Garaschuk, O. (2016). Long-term in vivo single-cell tracking reveals the switch of migration patterns in adult-born juxtaglomerular cells of the mouse olfactory bulb. Cell Res *26*, 805–821.

Lin, C.-W., Sim, S., Ainsworth, A., Okada, M., Kelsch, W., and Lois, C. (2010). Genetically Increased Cell-Intrinsic Excitability Enhances Neuronal Integration into Adult Brain Circuits. Neuron *65*, 32–39.

Linden, R., Martins, R.A.P., and Silveira, M.S. (2005). Control of programmed cell death by neurotransmitters and neuropeptides in the developing mammalian retina. Progress in Retinal and Eye Research *24*, 457–491.

Livneh, Y., and Mizrahi, A. (2011). Long-term changes in the morphology and synaptic distributions of adult-born neurons. J. Comp. Neurol. *519*, 2212–2224.

Livneh, Y., Feinstein, N., Klein, M., and Mizrahi, A. (2009). Sensory Input Enhances Synaptogenesis of Adult-Born Neurons. J. Neurosci. *29*, 86–97.

Livneh, Y., Adam, Y., and Mizrahi, A. (2014). Odor Processing by Adult-Born Neurons. Neuron *81*, 1097–1110.

Lledo, P.-M., Gheusi, G., and Vincent, J.-D. (2005). Information Processing in the Mammalian Olfactory System. Physiological Reviews *85*, 281–317.

Lledo, P.-M., Alonso, M., and Grubb, M.S. (2006). Adult neurogenesis and functional plasticity in neuronal circuits. Nature Reviews Neuroscience *7*, 179–193.

Lledo, P.-M., Merkle, F.T., and Alvarez-Buylla, A. (2008). Origin and function of olfactory bulb interneuron diversity. Trends in Neurosciences *31*, 392–400.

Lois, C., and Alvarez-Buylla, A. (1994). Long-distance neuronal migration in the adult mammalian brain. Science *264*, 1145–1148.

Lois, C., García-Verdugo, J.-M., and Alvarez-Buylla, A. (1996). Chain Migration of Neuronal Precursors. Science *271*, 978–981.

Luhmann, H.J., Sinning, A., Yang, J.-W., Reyes-Puerta, V., Stüttgen, M.C., Kirischuk, S., and Kilb, W. (2016). Spontaneous Neuronal Activity in Developing Neocortical Networks: From Single Cells to Large-Scale Interactions. Front. Neural Circuits *10*.

Magavi, S.S.P., Mitchell, B.D., Szentirmai, O., Carter, B.S., and Macklis, J.D. (2005). Adult-Born and Preexisting Olfactory Granule Neurons Undergo Distinct Experience-Dependent Modifications of their Olfactory Responses In Vivo. J. Neurosci. *25*, 10729–10739.

Mandairon, N., Stack, C., Kiselycznyk, C., and Linster, C. (2006). Broad activation of the olfactory bulb produces long-lasting changes in odor perception. PNAS *103*, 13543–13548.

Maslyukov, A., Li, K., Su, X., Kovalchuk, Y., and Garaschuk, O. (2018). Spontaneous calcium transients in the immature adult-born neurons of the olfactory bulb. Cell Calcium *74*, 43–52.

McGann, J.P., Pírez, N., Gainey, M.A., Muratore, C., Elias, A.S., and Wachowiak, M. (2005). Odorant Representations Are Modulated by Intra- but Not Interglomerular Presynaptic Inhibition of Olfactory Sensory Neurons. Neuron *48*, 1039–1053.

McLachlan, G., and Peel, D. (2000). Finite mixture models (Wiley).

McVea, D.A., Murphy, T.H., and Mohajerani, M.H. (2016). Large Scale Cortical Functional Networks Associated with Slow-Wave and Spindle-Burst-Related Spontaneous Activity. Front. Neural Circuits *10*.

Méndez-Armenta, M., Nava-Ruíz, C., Juárez-Rebollar, D., Rodríguez-Martínez, E., and Yescas Gómez, P. (2014). Oxidative Stress Associated with Neuronal Apoptosis in Experimental Models of Epilepsy (Hindawi).

Merkle, F.T., Fuentealba, L.C., Sanders, T.A., Magno, L., Kessaris, N., and Alvarez-Buylla, A. (2014). Adult neural stem cells in distinct microdomains generate previously unknown interneuron types. Nature Neuroscience *17*, 207–214.

Ming, G., and Song, H. (2005). Adult Neurogenesis in the Mammalian Central Nervous System. Annual Review of Neuroscience *28*, 223–250.

Ming, G., and Song, H. (2011). Adult Neurogenesis in the Mammalian Brain: Significant Answers and Significant Questions. Neuron *70*, 687–702.

Mirzadeh, Z., Merkle, F.T., Soriano-Navarro, M., Garcia-Verdugo, J.M., and Alvarez-Buylla, A. (2008). Neural Stem Cells Confer Unique Pinwheel Architecture to the Ventricular Surface in Neurogenic Regions of the Adult Brain. Cell Stem Cell *3*, 265–278.

Mizrahi, A. (2007). Dendritic development and plasticity of adult-born neurons in the mouse olfactory bulb. Nat Neurosci *10*, 444–452.

Mizrahi, A., Lu, J., Irving, R., Feng, G., and Katz, L.C. (2006). In vivo imaging of juxtaglomerular neuron turnover in the mouse olfactory bulb. PNAS *103*, 1912–1917.

Mombaerts, P., Wang, F., Dulac, C., Chao, S.K., Nemes, A., Mendelsohn, M., Edmondson, J., and Axel, R. (1996). Visualizing an Olfactory Sensory Map. Cell *87*, 675–686.

Moreno, M.M., Linster, C., Escanilla, O., Sacquet, J., Didier, A., and Mandairon, N. (2009). Olfactory perceptual learning requires adult neurogenesis. PNAS *106*, 17980–17985.

Moreno-Jiménez, E.P., Flor-García, M., Terreros-Roncal, J., Rábano, A., Cafini, F., Pallas-Bazarra, N., Ávila, J., and Llorens-Martín, M. (2019). Adult hippocampal neurogenesis is abundant in neurologically healthy subjects and drops sharply in patients with Alzheimer's disease. Nature Medicine 1.

Mori, I. (2001). Olfaction. In Encyclopedia of Genetics, S. Brenner, and J.H. Miller, eds. (New York: Academic Press), pp. 1368–1370.

Mouret, A., Gheusi, G., Gabellec, M.-M., de Chaumont, F., Olivo-Marin, J.-C., and Lledo, P.-M. (2008). Learning and survival of newly generated neurons: when time matters. J. Neurosci. *28*, 11511–11516.

Mouret, A., Lepousez, G., Gras, J., Gabellec, M.-M., and Lledo, P.-M. (2009). Turnover of Newborn Olfactory Bulb Neurons Optimizes Olfaction. J. Neurosci. *29*, 12302–12314.

Mu, Y., Zhao, C., Toni, N., Yao, J., and Gage, F.H. (2015). Distinct roles of NMDA receptors at different stages of granule cell development in the adult brain. ELife *4*, e07871.

Murphy, G.J., Darcy, D.P., and Isaacson, J.S. (2005). Intraglomerular inhibition: signaling mechanisms of an olfactory microcircuit. Nature Neuroscience *8*, 354–364.

Murthy, V.N. (2011). Olfactory Maps in the Brain. Annual Review of Neuroscience *34*, 233–258.

Myatt, D.R., Hadlington, T., Ascoli, G.A., and Nasuto, S.J. (2012). Neuromantic – from Semi-Manual to Semi-Automatic Reconstruction of Neuron Morphology. Front Neuroinform *6*.

Nagayama, S., Enerva, A., Fletcher, M.L., Masurkar, A.V., Igarashi, K.M., Mori, K., and Chen, W.R. (2010). Differential Axonal Projection of Mitral and Tufted Cells in the Mouse Main Olfactory System. Front. Neural Circuits *4*.

Nagayama, S., Homma, R., and Imamura, F. (2014). Neuronal organization of olfactory bulb circuits. Front Neural Circuits *8*.

Nakamura, T., and Gold, G.H. (1987). A cyclic nucleotide-gated conductance in olfactory receptor cilia. Nature *325*, 442–444.

Nissant, A., Bardy, C., Katagiri, H., Murray, K., and Lledo, P.-M. (2009). Adult neurogenesis promotes synaptic plasticity in the olfactory bulb. Nat Neurosci *12*, 728–730.

Nottebohm, F. (2002). Why Are Some Neurons Replaced in Adult Brain? J. Neurosci. *22*, 624–628.

Orrenius, S., Zhivotovsky, B., and Nicotera, P. (2003). Regulation of cell death: the calcium–apoptosis link. Nature Reviews Molecular Cell Biology *4*, 552–565.

Ota, H., Hikita, T., Sawada, M., Nishioka, T., Matsumoto, M., Komura, M., Ohno, A., Kamiya, Y., Miyamoto, T., Asai, N., et al. (2014). Speed control for neuronal migration in the postnatal brain by Gmip-mediated local inactivation of RhoA. Nature Communications *5*, 1–12.

Parrish-Aungst, S., Shipley, M. t., Erdelyi, F., Szabo, G., and Puche, A. c. (2007). Quantitative analysis of neuronal diversity in the mouse olfactory bulb. J. Comp. Neurol. *501*, 825–836.

Petreanu, L., and Alvarez-Buylla, A. (2002). Maturation and Death of Adult-Born Olfactory Bulb Granule Neurons: Role of Olfaction. J. Neurosci. *22*, 6106–6113.

Pfisterer, U., and Khodosevich, K. (2017). Neuronal survival in the brain: neuron type-specific mechanisms. Cell Death Dis *8*, e2643.

Pinching, A.J., and Powell, T.P.S. (1971). The Neuron Types of the Glomerular Layer of the Olfactory Bulb. Journal of Cell Science *9*, 305–345.

Platel, J.-C., Angelova, A., Bugeon, S., Wallace, J., Ganay, T., Chudotvorova, I., Deloulme, J.-C., Béclin, C., Tiveron, M.-C., Coré, N., et al. (2019). Neuronal integration in the adult mouse olfactory bulb is a non-selective addition process. ELife *8*, e44830.

van Praag, H., Schinder, A.F., Christie, B.R., Toni, N., Palmer, T.D., and Gage, F.H. (2002). Functional neurogenesis in the adult hippocampus. Nature *415*, 1030–1034.

Price, J.L., and Powell, T.P.S. (1970). The mitral and short axon cells of the olfactory bulb. Journal of Cell Science *7*, 631–651.

Rochefort, C., and Lledo, P.-M. (2005). Short-term survival of newborn neurons in the adult olfactory bulb after exposure to a complex odor environment. European Journal of Neuroscience *22*, 2863–2870.

Rochefort, C., Gheusi, G., Vincent, J.-D., and Lledo, P.-M. (2002). Enriched Odor Exposure Increases the Number of Newborn Neurons in the Adult Olfactory Bulb and Improves Odor Memory. J. Neurosci. *22*, 2679–2689.

Saghatelyan, A., Roux, P., Migliore, M., Rochefort, C., Desmaisons, D., Charneau, P., Shepherd, G.M., and Lledo, P.-M. (2005). Activity-Dependent Adjustments of the Inhibitory Network in the Olfactory Bulb following Early Postnatal Deprivation. Neuron *46*, 103–116.

Sailor, K.A., Valley, M.T., Wiechert, M.T., Riecke, H., Sun, G.J., Adams, W., Dennis, J.C., Sharafi, S., Ming, G., Song, H., et al. (2016). Persistent Structural Plasticity Optimizes Sensory Information Processing in the Olfactory Bulb. Neuron *91*, 384–396.

Sakamoto, M., Imayoshi, I., Ohtsuka, T., Yamaguchi, M., Mori, K., and Kageyama, R. (2011). Continuous neurogenesis in the adult forebrain is required for innate olfactory responses. PNAS *108*, 8479–8484.

Sakamoto, M., Kageyama, R., and Imayoshi, I. (2014). The functional significance of newly born neurons integrated into olfactory bulb circuits. Front Neurosci *8*.

Saraste, A. (1999). Morphologic criteria and detection of apoptosis. Herz *24*, 189–195.

Sawada, M., Kaneko, N., Inada, H., Wake, H., Kato, Y., Yanagawa, Y., Kobayashi, K., Nemoto, T., Nabekura, J., and Sawamoto, K. (2011). Sensory Input Regulates Spatial and Subtype-Specific Patterns of Neuronal Turnover in the Adult Olfactory Bulb. J. Neurosci. *31*, 11587–11596.

Schaar, B.T., and McConnell, S.K. (2005). Cytoskeletal coordination during neuronal migration. PNAS *102*, 13652–13657.

Segal, M. (2010). Dendritic spines, synaptic plasticity and neuronal survival: activity shapes dendritic spines to enhance neuronal viability. European Journal of Neuroscience *31*, 2178–2184.

Shen, Q., Wang, Y., Kokovay, E., Lin, G., Chuang, S.-M., Goderie, S.K., Roysam, B., and Temple, S. (2008). Adult SVZ Stem Cells Lie in a Vascular Niche: A Quantitative Analysis of Niche Cell-Cell Interactions. Cell Stem Cell *3*, 289–300.

Shepherd, G.M., Chen, W.R., Willhite, D., Migliore, M., and Greer, C.A. (2007). The olfactory granule cell: From classical enigma to central role in olfactory processing. Brain Research Reviews *55*, 373–382.

Shingo, T., Gregg, C., Enwere, E., Fujikawa, H., Hassam, R., Geary, C., Cross, J.C., and Weiss, S. (2003). Pregnancy-Stimulated Neurogenesis in the Adult Female Forebrain Mediated by Prolactin. Science *299*, 117–120.

Sierra, A., Encinas, J.M., Deudero, J.J.P., Chancey, J.H., Enikolopov, G., Overstreet-Wadiche, L.S., Tsirka, S.E., and Maletic-Savatic, M. (2010). Microglia Shape Adult Hippocampal Neurogenesis through Apoptosis-Coupled Phagocytosis. Cell Stem Cell *7*, 483–495.

Sim, S., Antolin, S., Lin, C.-W., Lin, Y., and Lois, C. (2013). Increased Cell-Intrinsic Excitability Induces Synaptic Changes in New Neurons in the Adult Dentate Gyrus That Require Npas4. J. Neurosci. *33*, 7928–7940.

Soudry, Y., Lemogne, C., Malinvaud, D., Consoli, S.-M., and Bonfils, P. (2011). Olfactory system and emotion: Common substrates. European Annals of Otorhinolaryngology, Head and Neck Diseases *128*, 18–23.

Sultan, S., Rey, N., Sacquet, J., Mandairon, N., and Didier, A. (2011). Newborn Neurons in the Olfactory Bulb Selected for Long-Term Survival through Olfactory Learning Are Prematurely Suppressed When the Olfactory Memory Is Erased. J. Neurosci. *31*, 14893–14898.

Sultan, S., Li, L., Moss, J., Petrelli, F., Cassé, F., Gebara, E., Lopatar, J., Pfrieger, F.W., Bezzi, P., Bischofberger, J., et al. (2015). Synaptic Integration of Adult-Born Hippocampal Neurons Is Locally Controlled by Astrocytes. Neuron *88*, 957–972.

Takahashi, H., Ogawa, Y., Yoshihara, S., Asahina, R., Kinoshita, M., Kitano, T., Kitsuki, M., Tatsumi, K., Okuda, M., Tatsumi, K., et al. (2016). A Subtype of Olfactory Bulb Interneurons Is Required for Odor Detection and Discrimination Behaviors. J. Neurosci. *36*, 8210–8227.

Takahashi, H., Yoshihara, S., and Tsuboi, A. (2018). The Functional Role of Olfactory Bulb Granule Cell Subtypes Derived From Embryonic and Postnatal Neurogenesis. Front. Mol. Neurosci. *11*.

Tashiro, A., Sandler, V.M., Toni, N., Zhao, C., and Gage, F.H. (2006). NMDA-receptor-mediated, cell-specific integration of new neurons in adult dentate gyrus. Nature *442*, 929–933.

Thestrup, T., Litzlbauer, J., Bartholomäus, I., Mues, M., Russo, L., Dana, H., Kovalchuk, Y., Liang, Y., Kalamakis, G., Laukat, Y., et al. (2014). Optimized ratiometric calcium sensors for functional in vivo imaging of neurons and T lymphocytes. Nat Meth *11*, 175–182.

Toescu, E.C. (1998). Apoptosis and cell death in neuronal cells: where does Ca2+ fit in? Cell Calcium *24*, 387–403.

Turnley, A., Basrai, H., and Christie, K. (2014). Is integration and survival of newborn neurons the bottleneck for effective neural repair by endogenous neural precursor cells? Front. Neurosci. *8*.

Valley, M., Mullen, T.R., Schultz, L., Sagdullaev, B.T., and Firestein, S. (2009). Ablation of mouse adult neurogenesis alters olfactory bulb structure and olfactory fear conditioning. Front. Neurosci. *3*.

Wachowiak, M., and Shipley, M.T. (2006). Coding and synaptic processing of sensory information in the glomerular layer of the olfactory bulb. Seminars in Cell & Developmental Biology *17*, 411–423.

Wallace, J.L., Wienisch, M., and Murthy, V.N. (2017). Development and Refinement of Functional Properties of Adult-Born Neurons. Neuron *96*, 883-896.e7.

Wang, C., Liu, F., Liu, Y.-Y., Zhao, C.-H., You, Y., Wang, L., Zhang, J., Wei, B., Ma, T., Zhang, Q., et al. (2011). Identification and characterization of neuroblasts in the subventricular zone and rostral migratory stream of the adult human brain. Cell Res *21*, 1534–1550.

Whitman, M.C., and Greer, C.A. (2007a). Adult-generated neurons exhibit diverse developmental fates. Devel Neurobio *67*, 1079–1093.

Whitman, M.C., and Greer, C.A. (2007b). Synaptic Integration of Adult-Generated Olfactory Bulb Granule Cells: Basal Axodendritic Centrifugal Input Precedes Apical Dendrodendritic Local Circuits. J. Neurosci. *27*, 9951–9961.

Whitman, M.C., and Greer, C.A. (2009). Adult neurogenesis and the olfactory system. Progress in Neurobiology *89*, 162–175.

Whitman, M.C., Fan, W., Rela, L., Rodriguez-Gil, D.J., and Greer, C.A. (2009). Blood vessels form a migratory scaffold in the rostral migratory stream. Journal of Comparative Neurology *516*, 94–104.

Wilms, C.D., and Häusser, M. (2014). Twitching towards the ideal calcium sensor. Nat Meth *11*, 139–140.

Winner, B., Cooper-Kuhn, C.M., Aigner, R., Winkler, J., and Kuhn, H.G. (2002). Long-term survival and cell death of newly generated neurons in the adult rat olfactory bulb. European Journal of Neuroscience *16*, 1681–1689.

Wit, E., Heuvel, E. van den, and Romeijn, J.-W. (2012). 'All models are wrong...': an introduction to model uncertainty. Statistica Neerlandica *66*, 217–236.

Xu, B., Chen, S., Luo, Y., Chen, Z., Liu, L., Zhou, H., Chen, W., Shen, T., Han, X., Chen, L., et al. (2011). Calcium Signaling Is Involved in Cadmium-Induced Neuronal Apoptosis via Induction of Reactive Oxygen Species and Activation of MAPK/mTOR Network. PLOS ONE *6*, e19052.

Yamaguchi, M., and Mori, K. (2005). Critical period for sensory experience-dependent survival of newly generated granule cells in the adult mouse olfactory bulb. PNAS *102*, 9697–9702.

Yuan, J., and Yankner, B.A. (2000). Apoptosis in the nervous system. Nature *407*, 802–809.

Yuste, R., MacLean, J., Vogelstein, J., and Paninski, L. (2011). Imaging Action Potentials with Calcium Indicators. Cold Spring Harb Protoc *2011*, pdb.prot5650.

Zhao, C., Deng, W., and Gage, F.H. (2008). Mechanisms and Functional Implications of Adult Neurogenesis. Cell *132*, 645–660.

Zilles, K. (2004). CHAPTER 27 - Architecture of the Human Cerebral Cortex: Regional and Laminar Organization. In The Human Nervous System (Second Edition), G. Paxinos, and J.K. Mai, eds. (San Diego: Academic Press), pp. 997–1055.

(2003). IEEE Standard on Transitions, Pulses, and Related Waveforms. IEEE Std 181-2003 1–60.

Publication

Maslyukov, A., Li, K., Su, X., Kovalchuk, Y., and Garaschuk, O. (2018). Spontaneous calcium transients in the immature adult-born neurons of the olfactory bulb. *Cell Calcium* 74, 43–52.doi: 10.1016/j.ceca.2018.06.001

Declaration of contribution

The dissertation work was carried out in the Institute of Physiology, Department of Neurophysiology at the Eberhard Karls Universität Tübingen under the supervision of Professor Dr. Olga Garaschuk. The study was conceived by Professor Dr. Olga Garaschuk. Dr. Kaizhen Li and Dr. Katherine Figarella produced the lentivirus and retroviruses, Dr. Nithi Asavapanumas and Dr. Nima Mojtahedi contributed to data analyses. Armin Gohl, Jonas Mueck, Marco Knecht and Suya Wang helped with morphological analysis. I accomplished anything else (~95%) in this study. I hereby declare that I have produced the work entitled “Enhanced ongoing endogenous activity predicts elimination of adult-born neurons in the mouse olfactory bulb”, submitted for the award of a doctorate on my own, have used only the sources and aids I indicated and have marked passages included from other works. I sear upon oath that these statements are true and that I have not concealed anything. I am aware that making false declaration under oath is punishable by a term of imprisonment of up to three years or by a fine.

Tübingen, 10.11.2020

Signature:

Acknowledgment

I wish to take this opportunity to sincerely thank all the people who helped me in this project, I would not be able to finish this project without their help.

Foremost, I want to thank my supervisor, Professor Olga Garaschuk for offering me this opportunity to join her lab, teaching me critical scientific thinking and pushing me to move forward in the field of science.

I must also thank my direct supervisor, Dr. Yury Kovalchuk. He is always knowledgeable, motivated, ready to help. I wish to acknowledge Dr. Kaizhen Li for his encouragement during these years. I would like to thank the other members of my doctoral committee, Professor Marlies Knipper and Professor Olaf Rieß for their assistance and insightful suggestions for this study. In addition, I appreciated the help from Dr. Katherine Figarella, Dr. Nithi Asavapanumas, Dr. Nima Mojtahedi, Armin Gohl, Jonas Mueck, Marco Knecht and Suya Wang and all the other members in the neurophysiology group.

Last but not the least, I dedicated this thesis to my wife Dr. Jie Yu and my parents who support me throughout my life. They all kept me going and this thesis would not have been possible without them.

Curriculum Vitae

EDUCATIONAL BACKGROUND

- 2015 - 2020, University of Tübingen, Germany
  Ph.D. candidate in Neurophysiology, supervisor: Prof. Olga Garaschuk
  Dissertation: Enhanced ongoing endogenous activity predicts elimination of adult-born neurons in the mouse olfactory bulb
- 2011 - 2014, Fudan University, China
  M.Sc. in Neuroscience, supervisor: Prof. Yong-Chun Yu
  Thesis: Gap junction between excitatory neurons in the neocortex plays important roles in cortical development
- 2007 - 2011, Central South University, China B.Sc. in Biology, supervisor: Prof. Xinxing Liu
  Thesis: The analysis of bacterial community diversity in the industrial biological pre-treatment of arsenic-containing ore

HONORS AND AWARDS

- 2015 - 2019: Four-year scholarship for Ph.D. Student, DAAD in Germany
- 2014: The Excellent Graduate, Fudan University in China
- 2013: Guanghua Scholarship, Fudan University in China
- 2011 - 2013: Fudan University Scholarship (triples) in China
- 2011: The Excellent Graduate, Central South University in China
- 2010: National Encouragement Scholarship, Ministry of Education of China
- 2010: The Excellent Student Award, Central South University in China
- 2008 - 2010: Central South University Scholarship (triples) in China

PUBLICATION LIST

- Maslyukov, A., Li, K., **Su, X**., Kovalchuk, Y., and Garaschuk, O. (2018). Spontaneous calcium transients in the immature adult-born neurons of the olfactory bulb. *Cell Calcium*. 74, 43–52.
- **Su, X**.*, Chen, J.-J.*, Liu, L.-Y., Huang, Q., Zhang, L.-Z., et al. (2017). Neonatal CX26 removal impairs neocortical development and leads to elevated anxiety. *PNAS* USA. 114, 3228–3233. (*co-first author)
- **Su, X**., Guan, W., Yu, Y.-C., and Fu, Y. (2014). Cerebellar stem cells do not produce neurons and astrocytes in adult mouse. *Biochemical and Biophysical Research Communications*. 450, 378–383.
- Yang, W.-Z. , Liu, T.-T. , Cao, J.-W., Chen, X.-F., Liu, X., Wang, M., **Su, X.**, Zhang, S.-Q., Qiu, B.-L., Hu, W.-X., et al. (2016). Fear Erasure Facilitated by Immature Inhibitory Neuron Transplantation. *Neuron*. 92, 1352–1367.
- Wang, M., Chen, J.-J., Huang, Q., **Su, X.**, Yu, Y.-C., and Liu, L.-Y. (2019). Connexin43 in Neonatal Excitatory Neurons is Important for Short-Term Motor Learning. *Brain Research*. 1720, 146287.